Hot Stamping of a Boron Steel

Side Impact Beam

with Tailored Flange Properties -

Experiments and Numerical Simulations

by

Yonathan Prajogo

A thesis
presented to the University of Waterloo
in fulfillment of the
thesis requirement for the degree of
Masters of Applied Science
in
Mechanical Engineering

Waterloo, Ontario, Canada, 2015

I hereby declare that I am the sole author of this thesis. This is a true copy of the thesis, including any required final revisions, as accepted by my examiners.

I understand that my thesis may be made electronically available to the public.

Abstract

The effect of tailoring of hot stamped components is investigated, specifically the introduction of a tailored (locally softened) flange within an otherwise martensitic hot formed side impact beam. The effect of tailoring on the resulting micro-hardness distribution and crash response during three-point bending is examined. The "in-die heating" tailoring method is considered, using a cooled die with local heating in the flange region. The heated regions cool the flange at a lower cooling rate to produce a softer region with higher ductility.

In the current work, three different die temperatures are chosen for the forming conditions in the tailored flange region. A fully hardened beam is hot formed and quenched with the dies set at room temperature as a benchmark case. Die temperatures in the flange region of 400 and 600°C are considered to produce the tailored side impact beams with reduced hardness in the flange. The material considered is Usibor® 1500-AS boron steel in thicknesses of 1.2 and 1.8 mm. Two quenching periods of 4 and 10 s are also studied.

After forming, the 1.2 mm thick beams exhibit very little difference in hardness distribution between the two quenching periods. The 1.8 mm thick beams have a larger difference in hardness distribution in the sidewall region caused by the difference in quenching (hold) time, with the shorter quench resulting in a softer sidewall condition. The measured micro hardness in the flange area of the 1.2 mm thick beams was 480, 360, and 225 HV (compared to 480 HV in the fully quenched region away from the flange) when the flange region of the dies are set to room temperature, 400°C, and 600°C respectively. For the 1.8 mm thick beams, the measured hardness was 475, 270, and 205 HV for the corresponding die temperatures and a 10 s quench period.

The tailored hot formed side impact beams are tested under three-point bend loading using two back plate configurations, referred to as the full back plate and split back plate configurations. The split back plate configuration was intended to focus deformation at the center of the beam thereby inducing fracture in the flange region. The beams exhibited two deformation modes, referred to as a "wrapping mode" versus a "collapse mode". In the wrapping mode, the friction between the punch and beam surface sufficient to cause the deforming beam to wrap around the indentor resulting in a higher overall load level and energy absorption. In the collapse mode, the cross-section collapses or folds under the indentor leading to a lower bending resistance. The mode selection was spurious with nominally identical beams exhibiting both responses. In general, the fully hardened beams have the highest peak load while the tailored beams formed with a 600°C dies have the lowest peak load in the 3-point bend experiments. None of the beams tested exhibited global fractures for all conditions considered.

Numerical models of the tailored hot forming process and subsequent three-point bend experiments were developed. The material model developed by Akerstrom (2006, PhD Thesis, Lulea University of Technology), as implemented in LS-DYNA with modifications proposed by Schill et al. (2013, 4th Int. CHS2 Conf., pp. 31-38) for tailoring simulations with a temperature hold period, is used to predict the hardness after tailored hot forming, while the TCM II constitutive model developed by Bardelcik et al. (2014, Mat. and Des., pp. 509-525) is used to predict the crash performance of the tailored hot formed beams. The forming simulations were able to accurately predict the hardness of the non-tailored, fully hardened beams with a predicted hardness of greater than 480 HV for both thicknesses and quenching periods. The hardness of the tailored (softened) flanges was predicted within 27 HV (12%) for the 600°C die temperature and 63 HV (18%) for the 400°C die temperature.

A parametric study using the three-point bending model, demonstrated that the deformation mode (wrapping versus collapsing) was controlled by the friction between the punch and beam surface. High friction levels promoted a wrapping deformation mode that produces higher load levels. For high friction cases, the simulations were able to predict the force versus displacement response of the wrapping mode beams with a full back plate configuration very closely up to an impactor displacement of 30 mm. At this point, the beams in the experiments begin to soften due to fracture in fold regions which was not accounted for in the models. The predicted loads for the beams with a split back plate configuration at peak load displacement of the experiment were lower than measured by 4.8 kN (or 22%), possibly due to an additional gap that formed between the flange and the back plate caused by a thermal distortion.

Tailoring the flange of the side impact beams lowered the peak force value when compared to the peak force of a fully hardened beam. Most of the fractures seen during the three-point bend experiments were located at the fully hardened region of a tailored beam. There was no spot weld failure in any of the three-point bend experiments regardless of the forming temperature or the spot weld configuration. Future work should include a bend experiment for which the specimens are more prone to fracture in the reduced hardness area, to further examine the role of tailoring in controlling the onset of fracture.

Acknowledgements

To my parents,

For giving my sister and I the opportunity of a better life in Canada

Table of Contents

List of Figures

xiii

List of Tables

List of Equations

1 Introduction

The consumer and regulatory demand to reduce the overall weight of a vehicle has pushed the development of stronger and lighter automotive parts to create more fuel efficient and environmentally friendly vehicles [1-3]. One of the avenues pursued to produce lighter vehicles is focused on developing structural components using ultra high-strength steels (UHSS). This class of materials allows for thinner gauge sheet components with less overall weight. However, light weighting of vehicles must respect the paramount safety standard requirements set by governments [4] and UHSS have the potential to provide the strength to meet occupant safety requirements. The overall goal of this research is to help create lightweight automotive structural parts using UHSS that will increase fuel efficiency while providing occupant safety.

UHSS materials can be utilized to produce the automotive parts with superior strength. An example of a UHSS material is so-called boron steel, commonly referred to as 22MnB5. This material is quench hardenable and can reach an ultimate tensile strength (UTS) of 1500 MPa [5]. The superior strength of this material is realized by heating the base material at 930°C for five minutes to fully austenize the material and quenching it at a rate faster than 30°C/s during forming to transform its microstructure from austenite to martensite [4]. Forming at high temperature also increases the formability and allows for a more complex structure and geometry to be formed. Hot forming also reduces the amount of spring back after quenching.

Fully quenched hot stamped parts will produce a hard martensitic microstructure with high strength and low ductility. Such parts are well suited for use in intrusion protection applications, however, they may perform poorly in energy absorption application due to early onset of fracture. Tailoring processes introduce softer bainite or ferrite into the hard martensitic microstructure, reducing tensile strength while improving ductility [6-8]. Tailored hot stamping can be utilized to produce a part with multiple regions, containing both quench hardened and tailored properties to optimize its energy absorption and crash performance during an impact. In this research, the use of in-die heating [9-15] to locally modify quenching rates and resulting properties to produce tailored hot stamped components is studied. A tailored component comprising a top hat cross-section side impact beam is hot formed and then loaded under three-point bending. Top hat structures are formed in either fully hardened configurations or with a locally softened flange regions using a range of die temperatures during forming. The resulting mechanical response is examined and numerical models of the forming and impact response of the beams are developed.

1.1 Tailored Hot Forming Die Quenching Technology

Hot forming of a boron steel sheet metal to produce UHSS structures allows for light weighting of a vehicle to reduce its fuel consumption while providing safety to the occupants [4]. This process requires a sheet metal blank material to be heated in a furnace to be fully austenized at 930°C for five minutes. The blank is quickly transported from the furnace into a die where it is formed quickly into its final shape. The tooling used in hot stamping is actively cooled using circulating coolant throughout the die to keep it near room temperature. The die is required to impose a cooling rate of greater than 30°C/s to achieve an austenite to martensite phase transformation. The additional strength relative to parts made out of conventional mild steel allows designers to create components of lower thickness thereby reducing overall weight.
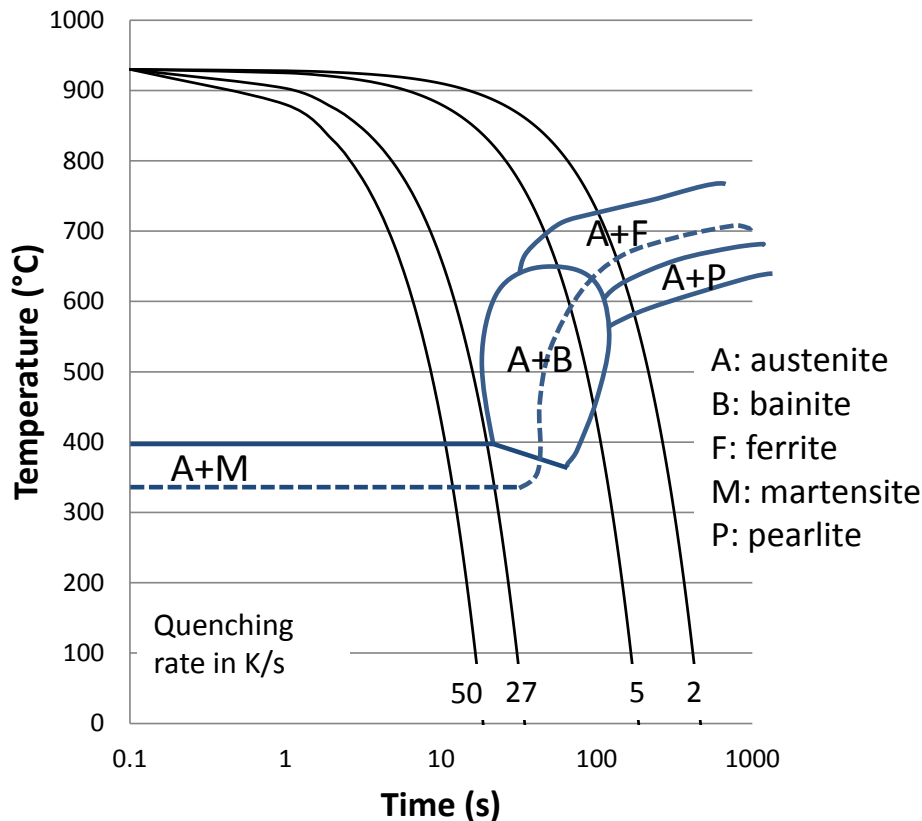
Figure 1: CCT diagram for boron steel material, adapted from [16].

As shown in Figure 1, the cooling rate of a completely austenized boron steel determines its final microstructure. Austenite will transform into one of its daughter phases including martensite, bainite, ferrite, and pearlite. Cooling rates between 30°C/s and 5°C/s will produce bainite while slower cooling rates will produce mixture of ferrite and pearlite.

2

Many different materials are suitable to be used in a vehicle's body in white. Figure 2 shows the many different categories of steel, comparing their tensile strength and ductility. Parts that can be manufactured using stamping technology can be made using these different materials with varying strength and ductility depending on their intended use. Materials with a higher ultimate tensile strength (UTS) tend to have a lower ductility while materials with lower UTS will have higher ductility. Parts manufactured for the purpose of energy absorption during a crash event are usually made from materials with a higher ductility to provide more deformation to absorb kinetic energy. Parts that require a higher strength to prevent deformation and provide intrusion prevention for passenger safety are typically made out of materials with a higher tensile strength. Quenched martensitic steels are excellent candidates for this intrusion prevention application.
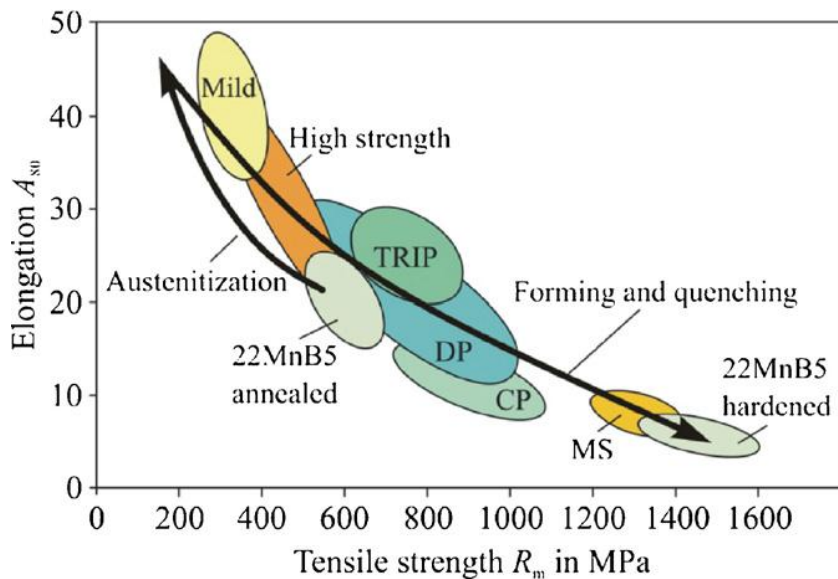
Figure 2: Mechanical properties of boron alloyed steel compared to other types of steel, adapted from [4].

The use of hot stamping technology to produce body-in-white parts has been increasing in the past decade [1,4,17]. Structural parts such as A- or B-pillars, doors, bumpers, and cross members are excellent candidates to be formed using hot stamping since these parts require high strength and low deformation for intrusion resistance.

Indirect and direct hot stamping processes are two major methods commonly used to produce hot stamped parts (Figure 3). The indirect method separates the forming and quenching into two different stages. Initially a part is formed at room temperature to approximately 90-95% of its final shape [9]. The final shape is not achieved at the initial forming stage possibly due to a formability limit at room temperature. The partially formed part is then heated in the furnace to austenize for approximately five minutes at

930°C and quickly transferred back into a cooled die to form and quench the part into its final shape. The part is removed and left to cool in still air until it reaches room temperature. In some cases, a further trimming or punching operation may follow to ensure correct alignment of the part to be connected to other parts.
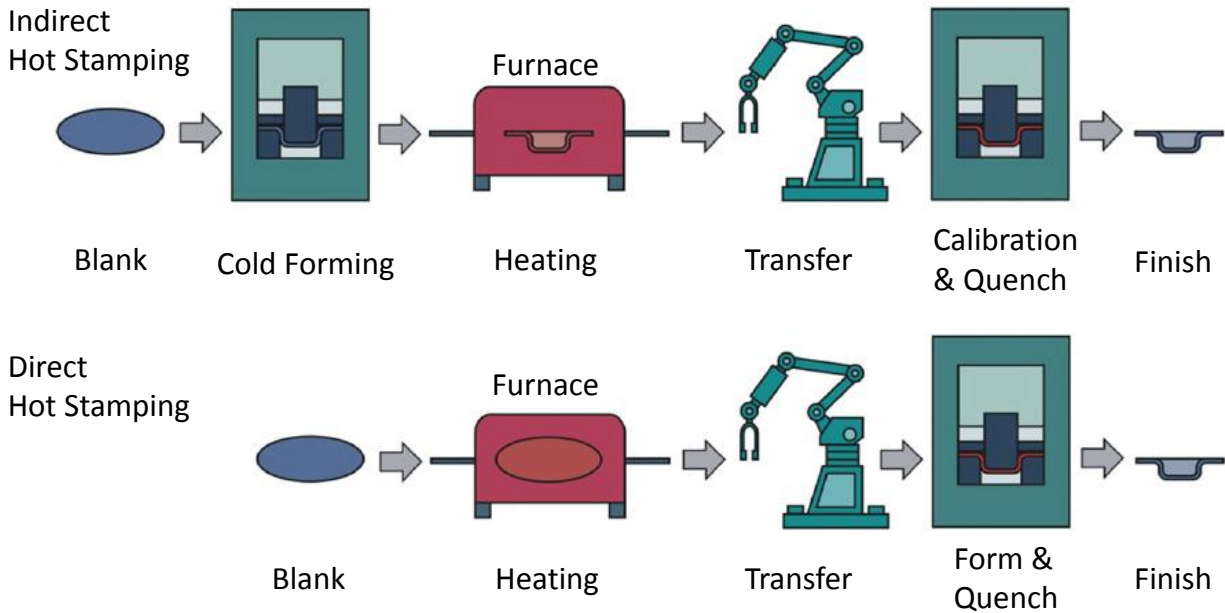
Figure 3: Indirect and direct hot stamping process, adapted from [4].

Direct hot stamping is done by first austenizing a blank in a furnace before transferring the blank into a cooled die to be press formed and quenched simultaneously. The part is taken out of the die the same way as in a direct stamping method to reach room temperature or for further trimming and punching operations. Direct hot stamping is more commonly used in industry and is the chosen method for the experiments in this study.

The basic hot forming process uses either a direct or an indirect method. Both methods produce a fully martensitic part that has a high tensile strength and low ductility throughout the structure. In some cases, certain regions in a crash structure could benefit from having a mechanical behavior with higher ductility, allowing more deformation prior to the onset of fracture to improve energy absorption. This approach has been explored by George et al. [9,18] who produced a tailored lab scale B-pillar. In that work, the base of the B-pillar was quenched using a heated die to form a softer microstructure while the main part of the B-pillar is quenched using a cooled die to achieve a hard martensitic microstructure.

The loss in energy absorption due to premature fracture during a crash event can be significant. The work done by Sigvant et al. [19] found a large difference in the total displacement of an impactor in drop tower

experiments considering fully martensitic versus tailored quenched parts of identical geometry. They concluded that the B-pillars with annealed flanges had a higher energy absorption capacity by 30% based on their drop tower experiments. The softer flanges led to improvements in spot weld impact performance. Spot welded coupons made from hardened boron steel were tested in a cross tension and overlap shear experiments and compared with coupons made from annealed specimens. The load capacity for the annealed coupons is higher in cross tension experiments but lower for overlap shear experiment compared to fully martensitic specimens. Softer regions in a structure with tailored properties may also help with subsequent punching and trimming operations after the forming stage to preserve the life of the tooling [20-22].

1.2   Hot Forming Material

ArcelorMittal developed an aluminum-silicon (Al-Si) coated boron sheet metal termed Usibor® 1500-AS for use in hot stamping processes. The Al-Si coating is used to prevent oxidation of the bulk material during austenization at 930°C. The protective coating fuses with the iron-based substrate material creating an iron-aluminum-silicon (Fe-Al-Si) layer when the heating rate achieved in a furnace is less than 12 K/s. It is advised that an Al-Si coated material should not be heated at a rate greater than 12 K/s to prevent premature melting of the protective coating [23,24]. A faster heating rate would melt the Al-Si layer prior to it fusing with the substrate. The addition of boron increases the hardenability during quenching. Prior to quenching, this material has an as-received UTS of 600 MPa with a minimum elongation of 10% while capable of achieving a UTS of 1500 MPa with an elongation of 6% after being hot stamped and rapidly quenched [5].

The hardenability of this material makes it a great candidate for use in structural parts where high strength is required. Following the CCT diagram shown in Figure 1, different microstructures can be achieved depending on the cooling rate experienced by a blank during forming and quenching. Bardelcik et al. [25] found that at a cooling rate of 25°C/s, the austenite transformed into a largely martensitic microstructure with a small amount of bainite and an overall Vickers micro hardness of 420 HV. At higher cooling rates of 45°C or faster, the fully martensitic microstructure has a hardness of greater than 472 HV. Bardelcik et al. [26] also found that the average Vickers hardness obtained with different cooling rates increases linearly with the area fraction of martensite starting at 275 HV to 470 HV. Deformation during quenching at a lower cooling rate led to the formation of ferrite, increasing the uniform elongation and the ultimate tensile strength with no effect on the yield strength [8].

1.3 Blank Heating Technologies

A number of technologies are available to heat a boron sheet steel to the austenization temperature in production of hot stamped parts. This section describes three available options for industrial use in hot stamping process.

1.3.1 Convection Furnace

The most commonly used furnace used for industrial operation is a convection furnace. Specifically, this method uses rollers through a long furnace that accepts as-received material inserted in one end and which is transferred through the furnace to the die at the other end. Typically, the length of this furnace would range from 30-40 meters depending on the blank size being heated, the amount of time required to austenize a blank, and the rate at which the part is hot stamped [4]. A convection roller furnace in an assembly line application can be divided into multiple thermal zones to tailor the heating rate for a blank. Floor space requirements can be a constraint in an assembly line environment and multi-level chamber furnaces can be used to reduce the floor space as multiple furnaces are stacked on top of each other. This approach increases cost and complexity [27].

1.3.2 Conduction/Resistance Heating

Resistance heating of a blank is done by conducting an electrical current through the bulk material to create heat as described by Joule's first law. The heat generated in the blank material is directly proportional to the amount of power applied through a blank. The geometry of the blank and any irregularities in the density or thickness will affect the current path and final temperature distribution after the austenization of a blank. Therefore, uniformly austenizing a blank with an irregular geometry would be more difficult with this method [24,28], although the work of Mori et al. [15] shows that a uniform temperature distribution can be achieved. It was also shown that it is possible to austenize only select target regions within a blank using a separated current for resistance heating. This is done by providing multiple electric current paths only to the desired regions in a blank. This method is quite difficult to achieve in practice as the process has to be done quickly to prevent heat loss from the intended heating area. It is more difficult to ensure uniform results between multiple regions in a blank as a path with a smaller resistance will have more current passing through it. It was also noted that the power equipment requirement becomes more complex and power losses become larger as blanks become larger and of more complex geometry. A bypass resistance heating was developed to allow all regions in a blank intended to be heated to have the same amount of current passing through. It is done by bypassing regions not intended to be heated by providing an alternate path for the electric current using a copper bypass. This method was able to produce tailored hot stamped top hat parts with a hardness value ranging from 280 HV to 500 HV [29].

1.3.3 Induction Heating

Induction heating uses electrical coils around a blank to create induced current to generate heat in a blank. It is a well developed technology in applications such as melting and bulk metal forming, however, this heating method is not a commonly used method for hot forming technology. This technology can be used in an industrial application using a conveyor or a chain drive system. The process parameters that affect the heating rate and final temperature are the power, frequency, and feed speed of the chain drive system. The work done by Kolleck et al. [28] shows that two stage induction heating can be used to produce a fully hardened part after quenching with a hardness of 487 HV. Further research is being done to investigate the suitability of this technology for use with aluminum-silicon coated material.

1.4 Tailoring Techniques

Conventional hot stamped parts are usually designed to be fully martensitic to provide uniform high strength properties. In the current study, a tailored hot stamping method is utilized to study the potential of improving crash response behaviour of a structural part, such as a side impact beam, to absorb more kinetic energy during an impact.

Multiple methods are available to tailor the mechanical properties within a component to improve crash response. Such methods include Tailor Welded Blanks (TWB), Tailor Rolled Blanks (TRB), partial austenizing, post tempering, tailored quenching, and tailored tempering. The following sections discuss each method along with its advantages and disadvantages.

1.4.1 Tailor Welded Blanks

This method involves tailoring the strength or thickness of a part by joining several different alloys into a single sheet. ArcelorMittal offers two different alloys that can be combined within tailor welded blanks (TWB): Usibor® 1500-AS and Ductibor® 500P have been used to create a TWB structure with uniform thickness. Ductibor® 500P has a UTS of 550 MPa and an elongation of over 15% at fracture after it is hot formed and rapidly quenched [5].

The advantage in using the TWB method lies in part consolidation by combining multiple parts of different strength/thickness into one [3,30]. Munera et al. [31] were successful in reducing the weight of a door ring, a rear rail, and a front rail while maintaining intrusion prevention using TWBs. The drawback comes from the step in thickness necessary to produce the as-received blanks required to form the designed parts. The heat affected zone (HAZ) in TWBs can also cause some unwanted failure during forming due to limited formability in the local HAZ. Tailoring a part using this method also leads to concerns over shifting of the weld line between the two different materials during forming [32]. Proper

design of the blank and locating the blank within the die prior to forming is crucial to form the structure correctly.

1.4.2 Tailor Rolled Blanks

A slightly different approach to TWBs, Tailor Rolled Blanks (TRB) uses the rolling process to create multiple thicknesses within a single blank. This approached is slightly different than for TWBs as this method will have the same as-received material while TWBs can use different materials and thicknesses. A survey done by Perez-Santiago et al. [17] shows twelve different recent vehicle models that use TRB parts to reduce the overall weight of parts such as B-pillars, rear bumpers, and cowl beams.

Tailoring the thicknesses within a part allows designers to tailor its behaviour during a crash in which either intrusion protection or energy absorption is intended. Two advantages of this method are the weight saving by varying the thickness within one part and also the elimination of joining processes before or after forming.

A disadvantage associated with this method is the potential movement of the thickness step during forming of TRBs. If the step moves relative to the tooling, this may affect the local contact between the blank and dies. The change in contact pressure will affect the cooling rate of a formed blank during quenching and may result in a different microstructure and mechanical properties from that intended.

1.4.3 Partial Austenizing in a Furnace

Partial austenizing of a boron sheet metal can be done by heating only one region of a blank in a furnace that has been divided into multiple thermal sections where the temperature of each individual section can be independently controlled. This method creates a non-uniform temperature distribution within the blank. The lower temperature in some regions prevents formation (or complete formation) of austenite and the subsequent formation of martensite during forming and quenching. Stoehr et al. [33] have studied austenizing a boron steel sheet with different temperature zones of 775°C, 825°C, and 950°C. The section of a sheet metal austenized at 775°C has a lower hardness value of 300 HV and yield stress (YS) of 600 MPa, whereas the other two higher temperature sections show hardness values of 440 HV and YS of 1100 MPa, indicating a fully martensitic microstructure. The lower hardness values from the partially austenized section comes from a ferritic-martensitic structure by combining the existing as-received ferrite and pearlite microstructure and the martensite formed during quenching. In another study, Wilsius et al. [34] used a heat shield above and below a region of a blank during austenization to form a B-pillar. The hardened region was tested to have a UTS of 1600 MPa with 6% elongation while the differential heating region has a UTS of 700 MPa with a 16% elongation.

This tailoring method allows the designer to use a fully cooled die without complex die design to achieve tailored properties. The tailoring comes from the different austenization temperatures. The disadvantage of this method is that the sectioning of multiple thermal zones in a furnace may be challenging and limits a designer to a smaller number of thermal zones. The blank must be properly aligned before entering the furnace.

1.4.4 Post Tempering

As-formed hot stamped parts can be tailored by locally heat treating sections of the part after quenching, a process known as post tempering. The post tempering study done by Labudde and Bleck [35] included 30 minutes of heat treatment in an air atmosphere furnace set to temperatures of 200°C, 300°C, 450°C, and 600°C followed by slow cooling to room temperature. The initial hardness of the specimen after hot stamping was recorded to be 550 HV. Post tempering at the aforementioned temperatures for 30 minutes reduced the hardness to 515 HV, 470 HV, 380 HV, and 270 HV, respectively. This method would reduce the cost to manufacture a complex die design with heaters and coolant channels; however, the extra step to temper parts post forming takes a relatively long time and is a major drawback from a production point of view.

1.4.5 Die Materials with varying Thermal Conductivity

Hot stamping tooling can be made from materials with varying degrees of thermal conductivity and specific heat capacity that control the rate of heat transfer between the blank and the die. Often, dies used in a production line application are made from 4140 steel [15]. This material has a thermal conductivity of 47 W/mK and is capable of removing heat from a blank fast enough to achieve a cooling rate greater than 30°C/s resulting in a fully martensitic structure. For tailoring applications, certain regions of a die can be manufactured using a material with a lower thermal conductivity or a lower specific heat capacity that leads to a slower cooling rate in that region, creating softer microstructures. Mori et al. [15] have developed dies using steatite (ceramic) plates that have a low thermal conductivity of 2 W/mK as a tooling material. The region formed with steatite material achieved a hardness of 250 HV while the regions formed in contact with the conventional die material (thermal conductivity of 25 W/mK) achieved a hardness of 475 HV.

This method of tailoring mechanical properties in a hot stamped structure is limited to the available thermal conductivities of materials that are strong enough to be used in a hot stamping environment. This method will save cost as it does not require the use of in-die heating. However, the cost associated with fabricating the segmented dies with different material will be higher.

1.4.6   Tailored Die Quenching

Mori et al. [15] produced a top hat structure using a grooved tooling designed to introduce gaps between the tool and work piece to reduce the local cooling rate. This specific tool forms a top hat cross-section and quenches the section in the corner or bend areas while leaving the flat sidewall and top hat untouched during quenching. The part was held during quenching for 3.5 seconds. The regions with a lower cooling rate had a measured hardness of 275 HV whereas the contacted regions have a measured hardness of 450 HV. This technique allows tailoring of hot stamped parts without any in-die heaters that can lower the cost of die manufacturing. However, it only allows tailoring on flat surfaces of a part in order to introduce gaps with the tooling.

Work done by George et al. [9,18,36] considered a tailored laboratory-scale B-pillar produced using a partially heated die. In-die cartridge heaters are installed in the lower half of the die that forms part of the B-pillar that attaches to a door frame. The hardness achieved in a tailored laboratory-scaled B-pillar by George et al. is shown in Figure 4. The heated region of the tool was set to a temperature of up to 400°C for forming and quenching. The center part of the B-pillar is formed with a cooled die that can achieve a cooling rate of greater than 30°C/s during forming and quenching. The heated and cooled dies are separated using a 1 mm air gap as an insulation to prevent heat transfer. The cooled tooling was able to produce a fully martensitic microstructure (505 HV) whereas the heated region developed a bainitic and ferritic microstructure with hardness in the range 262-304 HV [18].

(a)   (b)
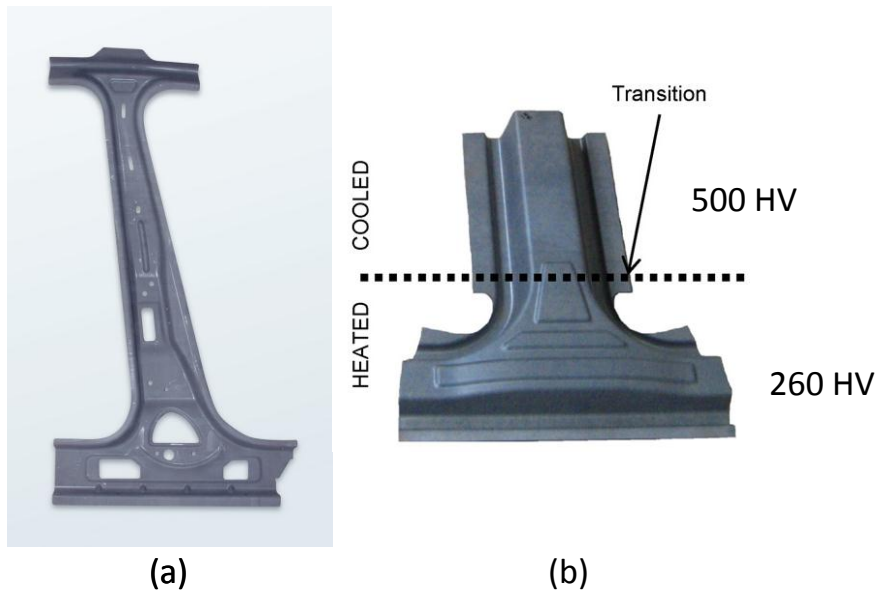
Figure 4: (a) Automotive B-pillar from ArcelorMittal [5], and (b) laboratory-scale B-pillar adapted from [18].

Svec and Merklein [10] quenched a flat blank using a cooled and heated die simultaneously to study the effect of die temperature and contact pressure on the heat transfer coefficient. The die temperature used in their study ranges from room temperature to 500°C. A hardness value of 240 to 290 HV was achieved in the heated zone at 500°C, depending on the contact pressure, while a hardness of 550 HV was achieved in the cooled zone. Erturk et al. [37] also quenched a flat blank using a partially cooled and heated die up to 550°C. The tensile strength of the quenched specimen ranges from 660 to 1450 MPa when formed at 550 and 200°C, respectively. Banik et al. [38] formed a B-pillar using a partially heated die to achieve a lower hardness of 200 HV. Erhardt and Boke [39] formed a B-pillar using a partially heated die at 200°C and achieved a lower hardness of 200 HV transitioning to 500 HV in the fully hardened region. Berglund [40] formed a tailored hot formed hat shaped part with a soft region in the middle and studied the part under a four-point bending test. The softened region was able to prevent cracks from forming in the heat affected zone (HAZ) that would form due to spot welding in a fully hardened region. Eller et al. [12] formed a 500 mm long top hat shape beam with one half of the die heated at 530°C while the other half is set to 30°C as shown in Figure 5. The two halves of the tooling are separated by a 1.4 mm air gap. The hardness ranged between 250 to 465 HV over a transition distance of 150 mm.
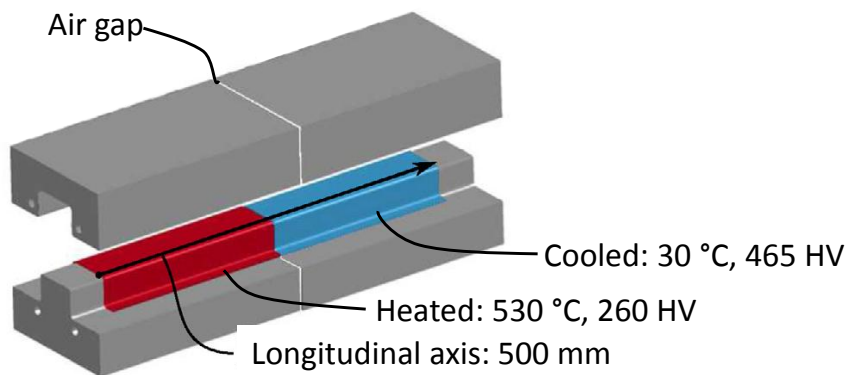
Figure 5: Top hat section formed by Eller et al., adapted from [12]

This method provides an easily controllable tooling condition giving distinct heated and cooled die sections to produce tailored hot formed parts. The temperature distribution of the tooling can be set to have a steep or more gradual transition between the cooled and heated dies depending on the intended final microstructure of the formed part. The disadvantage of this tailoring method comes from the additional machining cost to produce a die that is separated into the different thermal zones rather than producing a simple monolithic punch and die tooling.

1.5 Quasi-Static and Impact Testing of Hot Stamped Structures with Tailored Properties

Laboratory-scale tailored hot stamped parts have been crash tested to compare their performance relative to non-tailored fully martensitic parts. This is necessary to assess whether tailoring the properties of a structural part in a vehicle would improve its performance during a crash.

The work done by Sigvant et al. [19] compared B-pillars with annealed (soft) flanges to fully martensitic counterparts in a drop tower experiment with a fixed weight of 77 kg and a range of impact velocities. They used a normalized energy unit using "1 E" as the lowest energy used in an experiment. A normalized energy value of 1.7 E was enough to fracture both flanges of the fully hardened flange B-pillars while the annealed flanges only sustained fracture in one of the flanges. They also found that the annealed B-pillars can absorb approximately 30% more energy than the fully hardened B-pillars when subjected to the same amount of deformation.

Wilsius et al. [34] impacted three different B-pillars made out of a monolithic hot stamped Usibor® 1500-AS, a laser welded blank using a combination of Usibor® 1500-AS and Ductibor® 500P, and a partially hardened B-pillar from Usibor® 1500-AS using differential heating of the blank. The two B-pillars with tailored properties have a softer region at the bottom of the structure. Impacted in a 3-point bend fashion, the monolithic pillar deformed at the impactor contact site, while the other two tailored structures were deformed near the base of the pillars. Tailoring a structure can change the crash performance by moving the deformation zone, potentially improving the integrity of passenger safety inside the vehicle.

Sato et al. [41] experimented with a top hat structure spot welded along its flange to a backing plate in a 3-point bend configuration under impact and quasi-static velocities. They also demonstrated the effect of different bending spans. At a smaller bending span, the top hat shaped structure would crush under and 'wrap' around the impactor. Wrapping allows the top hat structure to deform following the circular shape of the impactor. A larger bending span would cause the hat shaped structure to collapse underneath the impactor creating a V-shaped fold. The experiments done with a larger bending span also decreased the peak force in the force-displacement response compared to smaller bending spans. At a constant bending span, higher speed experiments recorded larger bending moments compared to quasi-static experiments.

Omer [13] developed a hot stamped axial crush member with tailored properties along the length. They used an in-die heating method up to 700°C for one-half of the length with the remainder of length being quenched using a cooled tooling. The same geometry is used to form the fully hardened axial crush members to be crushed and compared to the tailored axial crush members. Experimental data showed that the fully hardened axial crush members achieved a higher peak force; however, due to the onset of

fracture, the tailored axial crush members were able to absorb more energy at higher levels of displacement. More importantly, the fully hardened crush members exhibited undesirable extensive cracking and tearing whereas the tailored components exhibited a desirable accordion crush mode.

1.6 Numerical Modeling

Considerable effort has been expended over the past decade to develop numerical modeling techniques to simulate the hot stamping process [14,16,34,42-45]. A key objective of this work has been the prediction of the final mechanical properties of hot stamped parts including microstructural phase composition and micro hardness. Also of importance is the prediction of the as-formed properties of hot stamped parts, particularly in terms of their crash behaviour.

1.6.1 Forming Material Models

One of the principle models used to simulate the response of steels during hot stamping and the model adopted in the current research was originally developed by Akerstrom [46] and uses the temperature history and deformation throughout the forming and quenching to predict the resulting hardness and microstructure. In the study by Akerstrom, the blank was given an initial temperature of 1200 K and the temperature history was calculated based on heat loss through convection, conduction, and radiation due to interaction with the tooling and air during transfer to and from the tooling. The austenite decomposition model used is proposed by Kirkaldy and Venugopalan [47] with a modification proposed by Li et al. [48]. The modified model calculates the volume fraction of each of the daughter microstructure phases (martensite, bainite, pearlite, or ferrite) as a function of austenite grain size, alloy composition, temperature, and the current fraction formed. The final composition of the material and the quench rate are used to calculate the Vickers hardness value after forming [46]. The model of Akerstrom has been implemented within the finite element program called LS-DYNA® and is referred to as the *MAT_244 or *MAT_UHS_STEEL [49] constitutive model.

The hardness of the blank elements is calculated based on the weighted average hardness of each phase formed:

$$HV = X_b HV_b + X_f HV_f + X_p HV_p + X_m HV_m \qquad (1)$$

where the volume fraction for each phase is represented by X, the Vickers hardness value for each phase is represented by HV, and the phases bainite, ferrite, pearlite, and martensite are represented using the subscripts b, f, p, and m, respectively. The hardness calculations for ferrite and pearlite were taken from the works of Maynier et al. [50], while the hardness calculations for bainite and martensite were taken from Bhadesia [51] and Honeycombe [52], respectively.

The hardness calculation in equation (1) assumed a continuous cooling rate at 700°C to be uniform throughout the whole process. This method will not work correctly to simulate tailored hot forming processes with the use of in-die heating. A modification by Schill et al. [53], implemented in the commercial finite element code LS-DYNA, is used to incrementally update the hardness for bainite and martensite when a holding phase is detected in the simulation. The modified hardness is calculated as

$$HV_i^{n+1} = \frac{x_i^n}{x_i^{n+1}} * HV_i^{n+1} + \frac{x_i^{n+1} - x_i^n}{x_i^{n+1}} h_i(T) \; for \; i = b, m \tag{2}$$

where $h_i(T)$ is the Vickers hardness as a function of temperature of bainite and martensite. This hardness calculation is used when a holding phase is detected with the following condition.

$$T \le T_{st,i} \text{ for } i = b, m \text{ and } |\Delta T_{avg}| \le \Delta T_{crit} \tag{3}$$

A holding phase is detected when the actual temperature of the material is below the start temperature of bainite and martensite, and when the average cooling rate is below a specified critical cooling rate [54].

The mechanical model used by Akerstrom is proposed by Leblond et al. [55-58] and is assumed valid for conditions where the austenite transforms into more than one daughter phases.

$$\Delta \varepsilon_{ij} = \Delta \varepsilon_{ij}^e + \Delta \varepsilon_{ij}^{th} + \Delta \varepsilon_{ij}^{tr} + \Delta \varepsilon_{ij}^p + \Delta \varepsilon_{ij}^{tp} \tag{4}$$

The total increment in strain $\Delta \varepsilon_{ij}$ is additively decomposed into the following strain increment: the elastic strain increment, $\Delta \varepsilon_{ij}^e$, the thermal strain increment, $\Delta \varepsilon_{ij}^{th}$, the isotropic transformation strain increment, $\Delta \varepsilon_{ij}^p$, and the plastic strain increment, $\Delta \varepsilon_{ij}^{tp}$. These strain increments are explained in detail by Akerstrom [46].

1.6.2   Heat Transfer Coefficient

The cooling rate of a blank is determined by the heat lost through conduction, convection, and radiation to its surroundings. It is important to model the thermal boundary condition properly to simulate the correct cooling rate required to calculate the final mechanical properties of a tailored hot stamped structure. Most of the heat transfer from the blanks happens through a conduction process by contact with the tooling (which is either water chilled or heated in the case of tailored hot stamping) during the forming and quenching stages. Factors such as die material and surface roughness are important considerations affecting the heat transfer between a blank and a die.

The contact heat transfer condition between the blank and tooling surface pairing is complex and can be a strong function of surface roughness (Figure 6). At some locations, the blank and die are in direct contact creating a location for thermal energy to transfer through direct conduction. At other locations, heat is

transferred through radiation and gas conduction. Direct conduction is a more efficient way to transfer thermal energy between a blank and die. For a given surface roughness, the conduction Heat Transfer Coefficient (HTC) is mainly a function of the applied pressure between the two surfaces [59,60]. When more pressure is applied between the two contact surfaces, the peaks in the contact region are elastically deformed providing more overall surface area between the blank and die for heat transfer. Overall, a greater press force will provide a higher cooling rate for a blank which helps to produce a fully martensitic component [61].

Other factors such as modulus of elasticity, temperature, and emissivity of the material can affect the overall heat transfer rate. Merklein et al. [62] have shown an approximately linear increase in average HTC as contact pressure increases. This HTC was reported to be in the range of 700-3000 W/m^2K and pressures of $0 - 40$ MPa. Caron et al. [59,63] have shown that there is a large jump in the HTC value between when the blank is initially placed on the die and when the press force and die pressure are applied as the blank is being formed. The inverse heat transfer analysis done by Caron et al. showed that at 8 MPa of pressure, the HTC value starts at 2000 W/m^2K and increases to 5000 W/m^2K as the temperature difference between the blank and die decreases and approaches zero. The change in HTC is attributed to the initial warping of the blank and associated poor initial contact versus the increase in overall contact surface area between the blank and the die due to the micro deformation of the surfaces with increased pressure. George et al. [18] took the HTC value based on experiments done by Oldenburg and Lindkvist [60] and modified it to give a better micro hardness prediction for the tailored hot stamped laboratory-scale B-pillars.
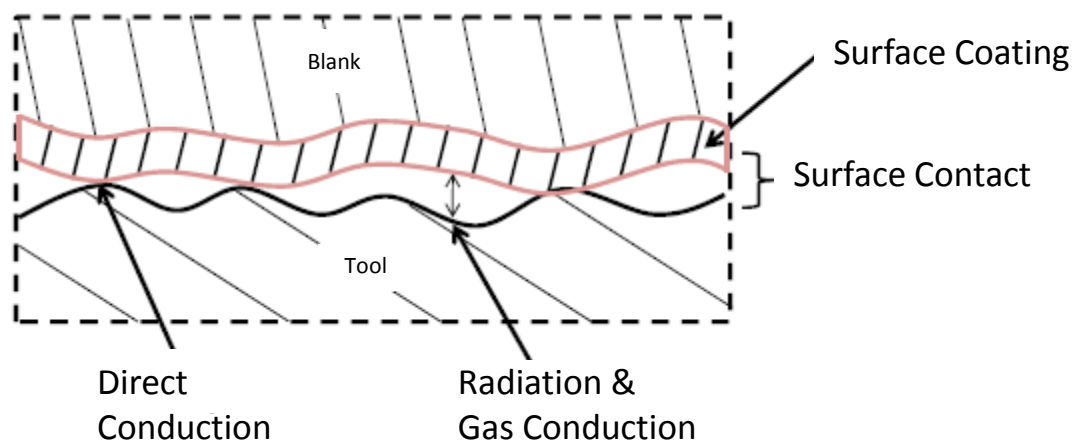
Figure 6: Contact zone between blank and tool for heat transfer adapted from [9].

1.6.3 Coefficient of Friction

The coefficient of friction is an important parameter in a sheet metal forming simulation to correctly predict the strain experienced by a formed blank. The friction condition under a hot stamping environment has been researched by Yanagida and Azushima [64] using a hot flat drawing experiment. At a temperature of 800°C, unlubricated boron steel blanks have a coefficient of friction of 0.6. The value is reduced to 0.4 when the blank is lubricated. Hardell and Prakesh [65] reported a coefficient of friction around 0.8 for plasma nitride tool steel against Al-Si coated boron steel at 800°C. Using a rotating pin-on-disk equipment, Ghiotti et al. [66] showed that the coefficient of friction for boron steel sheet at 800°C is between 0.5 – 0.6 without the use of any lubricants. The coefficient of friction increases to 0.8 with a reduced temperature of 500°C. They also found that the coefficient of friction is largely dependent on temperature and pressure. Hora [67] recommended a constant coefficient of 0.4 for static and dynamic friction in simulation of hot stamping operations.

1.6.4 Crash Modeling of Hot Stamped Components

Bardelcik et al. [26] derived a strain rate-sensitive constitutive model that account for strain rate sensitivity and utilizes a Voce [68] hardening description:

$$\sigma = \left(A + \left((B - A)e^{\frac{\varepsilon}{C}} \right) \right)(1 + \dot{\varepsilon})^D \tag{5}$$

The model is termed the Tailored Crash Model (TCM) and is intended for use with tailored hot stamped components with variable as-formed phases. The parameters A, B, C, and D in equation were determined by Bardelcik et al. [26] to be a function of the as-formed hardness:

$$A = 0.005318HV^2 - 0.7902HV + 699.49 \ (MPa) \tag{6}$$

$$B = 2.499HV - 71.24 \ (MPa) \tag{7}$$

$$C = \begin{cases} -7.747 \times 10^{-9}HV^3 + 9.222 \times 10^{-6}HV^2 - 0.003652HV + 0.4884, \text{for } 266 < HV < 375 \\ +0.0072, \text{for } HV > 375 \end{cases} \tag{8}$$

$$D = 0.018 \tag{9}$$

The TCM model was calibrated for specimens that have a fully martensitic or bainitic microstructure. An extension of the TCM, known as the TCM II, was developed by Bardelcik et al. [8] to better predict the

hardening response for parts that have ferritic microstructural components. It was concluded by Bardelcik et al. that the TCM can be used when the predicted Vickers hardness is 466 HV or greater (fully martensitic condition). Simulation of hot stamped parts with Vickers micro hardness of less than 466 HV should use the TCM II model to correctly predict the flow stress of parts with ferritic (or partially ferritic) microstructures. For the TCM II model, the A, B, C, and D parameters are modified to be functions of the as-formed phase fractions:

$$A, B, C, D = \beta_1 + \beta_2 \left(\frac{M}{M+B}\right) + \beta_3 F + \beta_4 \left(\frac{M}{M+B}\right)^2 + \beta_5 F \left(\frac{M}{M+B}\right) + \beta_6 F^2 \qquad (10)$$

In which *M, B* and *F* are the phase fractions of martensite, bainite and ferrite, respectively and the values for β_n, n=1-6, are given in Table 1.

Table 1: Coefficients used for β_n to calculate parameters A, B, C, and D for TCM II model [8].

	β_1	β_2	β_3	β_4	β_5	β_6
A(MPa)	853	809.3	3050	-152.9	2.016	-2.05×10^4
B(MPa)	602.7	631.8	1438	-98.36	980.5	-1.599×10^4
C	0.01875	-0.03875	0.1657	-0.03009	-0.23	0.2447
D	0.018	-	-	-	-	-

The TCM and TCM II models can generate flow stress curves as a function of effective plastic strain for multiple different strain rates, based on the predicted hardness taken from the forming simulation of tailored hot stamped boron steel parts. The resulting microstructure at the end of a hot forming simulation is used to predict the behaviour of a tailored quenched part during a crash event. Bardelcik et al. [69] modelled crash behaviour of the tailored hot stamped laboratory-scale B-pillar developed by George et al. [9,18]. They developed a remapping program [8,26] to sort each individual elements within the as-formed B-pillar into eight different bins based on its predicted micro hardness. The model then creates a set of strain-rate sensitive flow stress curves for the elements in each bin based on the median Vickers hardness. The program outputs the material model in a format used by the LS-DYNA commercial finite element code using the *MAT_24 or *MAT_PIECEWISE_LINEAR_PLASTICITY constitutive model. Ostlund et al. [70] also used a remapping program that produces an effective flow curve with an effective fracture strain given at various biaxial ratios.

1.7   Current Work

The review of the current literature has shown that extensive knowledge exists concerning the hot forming process. The process and parameters required to form fully martensitic components are well known and this process has proven effective in strengthening structural components in order to reduce the overall weight of a vehicle.

There is less understanding of the tailored hot forming process, although it has been shown to potentially improve the crash performance of a structure in certain applications. One aspect to be considered, the focus of the current thesis, is the application of in-die heating to locally tailor (soften) the flange region of a hot stamped component and the development of numerical models of the crash response of such components. This form of tailoring has potential merit in improving ductility (and weldability) in the flange region.

The work done in support of this thesis is part of a larger project sponsored by Honda R&D Americas, Promatek Research Centre, and ArcelorMittal Dofasco. The overall project is geared towards developing the ability to simulate tailored hot forming of Usibor® 1500-AS and its crash performance. The project includes a total of four tasks. Task 1, the focus of this thesis, addresses the experimental and numerical study of hot forming and crash experiments on tailored hot formed side impact beams. Task 2 considers tailored hot formed axial crush members. Task 3 includes the study of heat transfer and quenching response during tailored hot stamping, while Task 4 comprises the characterization of fracture of hot stamped components for a range of tailored conditions.

This thesis research entails both experimental and numerical components. In the experiments, a side impact beam with tailored (locally softened) flanges is developed after which static and dynamic three-point bending experiments are performed to assess crashworthiness. Both tailored and fully martensitic beams are tested in order to assess the effect of tailoring on the mechanical response. Numerical models of the hot stamping and subsequent mechanical testing are also developed. The forming process models are used to assess the ability of the Akerstrom [46] constitutive model, with the modifications proposed by Schill et al. [53], to predict the phase and hardness distributions within the as-formed beams. In addition, the TCM II constitutive model developed by Bardelcik et al. [26] is assessed.

The balance of this thesis is organized as follows. The apparatus and experimental methods used for this study are described in Chapter 2. The numerical models of the tailored hot forming, quasi-static, and impact experiments on the tailored side impact beams are presented in Chapter 3. The measured Vickers hardness distributions from the as-formed beams and the results of the quasi-static and dynamic three-point bend experiments are discussed in Chapter 4. In Chapter 5, the experimental results are compared to

the predicted results from numerical simulations. The conclusions and recommendations for further work stemming from this research are presented in Chapter 6.

2 Experiments

2.1 Material

Boron steel, Usibor® 1500-AS, manufactured by ArcelorMittal and developed specifically for hot forming applications, is considered in this research. Two different thicknesses of 1.2mm and 1.8mm have been provided for this study. This material has an aluminum-silicon (Al-Si) coating to prevent surface oxidation during austenization of the sheet metal in the furnace prior to hot stamping. The coating thickness (25 μm) is included in the nominal thicknesses. The composition of Usibor® 1500-AS is shown in Table 2. The as-received material has a yield strength (YS) of approximately 300 MPa and an ultimate tensile strength (UTS) of approximately 500 MPa [5].

Table 2: Usibor® 1500-AS Material Composition [71].

Element	Composition (weight %)
Carbon (C)	0.22
Manganese (Mn)	1.23
Phosphorus (P)	0.008
Sulfur (S)	0.001
Silicon (Si)	0.25
Copper (Cu)	0.03
Nickel (Ni)	0.02
Molybdenum (Mo)	0.02
Chromium (Cr)	0.2
Columbium (Cb)	0.008
Vanadium (V)	0.008
Aluminum (Al)	0.03
Tin (Sn)	0.01
Titanium (Ti)	0.037
Nitrogen (N)	0.044
Boron (B)	0.004
Iron (Fe)	Remaining

The Continuous Cooling Transformation (CCT) diagram in Figure 1 shows that a fully martensitic microstructure can be achieved by austenizing at 900°C and quenching at a rate greater than the critical cooling rate of 30°C/s. Once the as-received material is austenized and quenched with a cooling rate greater than 30°C/s, the resulting YS and UTS are approximately 1100 MPa and 1500 MPa, respectively [5]. In such a fully martensitic form, this material has a micro hardness in the range of 450-500 HV [25,72].

2.2   Side Impact Beam Structure

A side impact beam in a vehicle door structure is used to provide intrusion protection to the passengers in the event of a side impact. The hot forming process is an ideal method to produce strong structural parts while keeping weight to a minimum to improve fuel efficiency. However, tailoring a side impact beam may provide some improvements in the crash performance. Selectively softening a region in a part can delay the onset of fracture and allow the part to deform further while absorbing more energy. It can also delay the failure of spot welds and keep the part structurally sound during an impact event as demonstrated by Sigvant et al. [19].
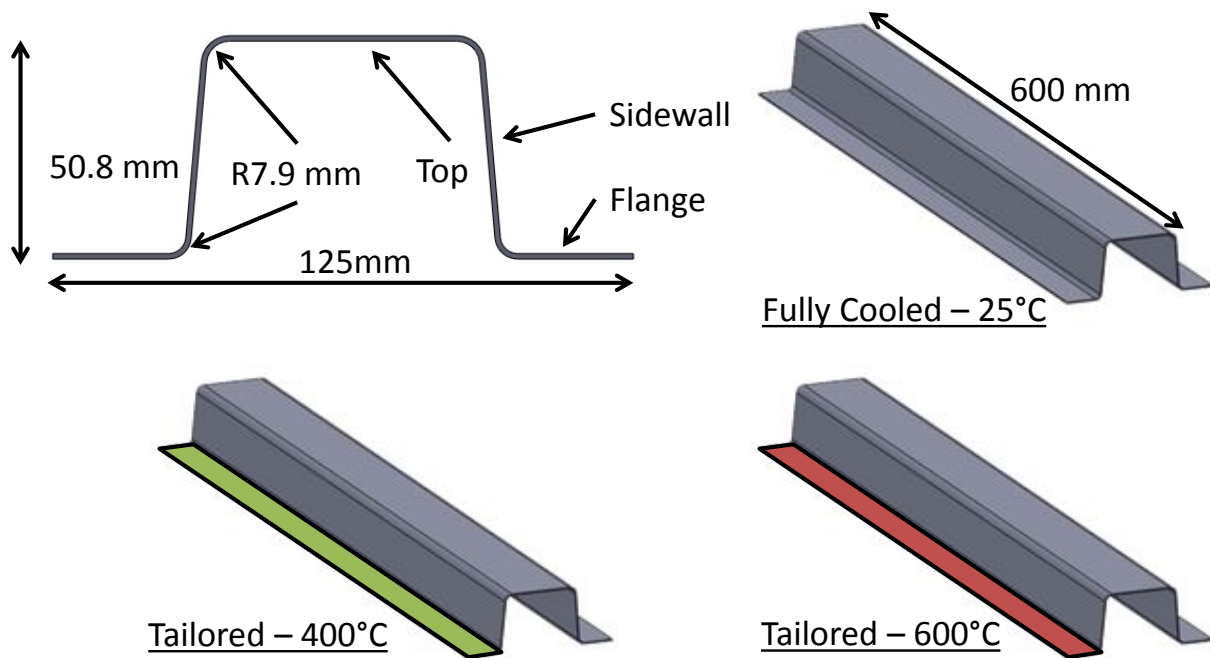
Figure 7: Top hat side impact beam profile and the flange tailoring temperature.

The side impact beam structure in this study is a top hat structure, shown in Figure 7, with the potential of soft tailoring the flange. The overall length of the beam is 600 mm. The cross section, referred to as a "top hat section", will have a width of 125 mm and a height of 50.8 mm. The flat section at the top of the cross section has a width of 50.8 mm. The flange has a width of 25 mm on each side. All of the corners have a radius of 7.94 mm and the sidewall has a draft angle of 5° from the vertical axis.

2.2.1   Forming Temperature and Quenching Period Configurations

The study consists of producing and testing a side impact beam with three different die temperature and two quenching period configurations. The forming test matrix is shown below in Table 3.

Table 3: Forming test matrix for 1.2 mm and 1.8 mm thicknesses.

Forming Flange Temperature (°C)	Quench Periods (seconds)
25	4
	10
400	4
	10
600	4
	10

The first configuration with a room temperature die is used to produce a fully martensitic side impact beam as a baseline for this study. This tooling temperature configuration is achieved with all the heaters turned off and the chilled water cooling system circulated during the forming and quenching process keeping all tooling components at near room temperature. For this configuration, a fan is used to force room temperature air through the press opening while a blank is being heated in the furnace to help cool the tool sections that do not incorporate chilled water cooling channels (see tooling description, below). The fan is turned off during the blank transfer process from the furnace to the die and during forming to prevent excess heat being removed from the heated blank. The other two die temperature configurations are used to produce a tailored hot stamped side impact beam with a fully martensitic top hat section and softer bainitic flanges. In this study, 400°C and 600°C were selected temperatures in the flange regions to produce these tailored microstructures. The effect of flange tailoring on the mechanical behaviour of the side impact beam under three-point bend loading is the primary focus of this research. The 400°C temperature was selected since it corresponded to that used by George [9], while 600°C was the highest temperature achievable using the available electrical power.

The two quenching periods are chosen to study the effect of quench time on the hardness distribution of the tailored flange. The shorter quenching period is more attractive in an industrial setting to reduce the cycle time required to produce a part.

2.3   Forming Tools and Equipment

The tooling used in this research, shown in Figure 8, was developed by George [14] to produce a laboratory-scale top hat side impact beam with tailored flange. The tooling consists of three main sections which include the female die, punch, and binder. The female die located in the upper half of the tool is divided into two main parts with a water-cooled section, which forms the C-channel top hat section, and a heated blank holder which contacts the flange section of the top hat structure. The stationary water-cooled

punch and the heated binder are located in the bottom half of the tool. The binder is guided by a slider plate and is forced upwards using six nitrogen gas spring cylinders. The binder sits 1 mm higher than the punch to prevent the austenized blank from contacting the cold surface of the punch and prematurely losing its thermal energy before the forming process begins. The upper section is attached to the ram of the hydraulic press and moves downwards towards the punch while the blank holder forces the binder downwards against the nitrogen springs during the forming process. The lower portion of the tool is fixed to the press table.
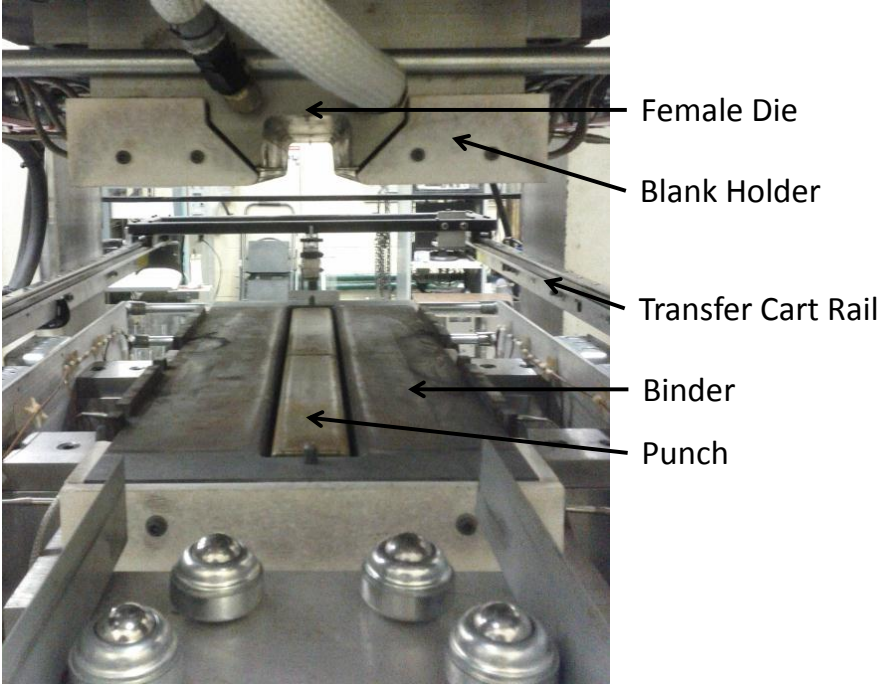
Figure 8: Tailor hot forming tool installed in the hydraulic press.
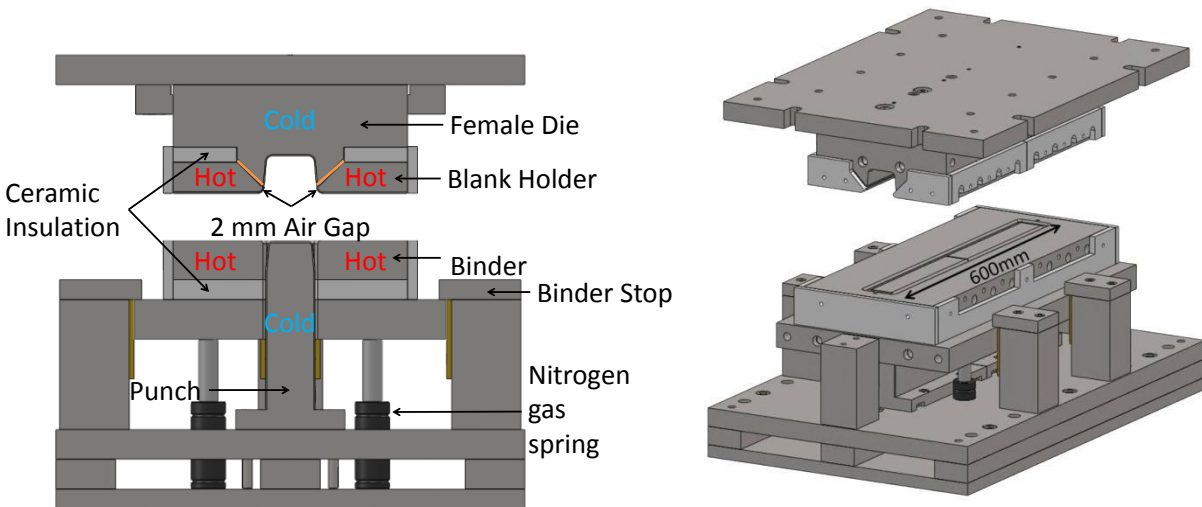
Figure 9: Tooling schematic showing heated and cooled regions of tool to produce tailored top hat section.

The binder is placed on top of six nitrogen gas spring cylinders and is secured in place with six binder stops, two on each side along the length and one on each end of the tool. The pressure inside the nitrogen gas spring cylinders was initially set to 6.9 MPa (1000 psi) for the 1.2 mm beams. This corresponds to an applied force of 26.8 kN (total) to the blank when the die is fully closed. The nitrogen gas spring cylinders were set to 10.3 MPa (1500 psi) for the 1.8 mm beams, corresponding to a force of 40.2 kN (total) in the fully closed position. Four 50 mm tall solid steel blocks are placed underneath the binder to prevent the nitrogen gas spring cylinders from bottoming out.

The upper portion of the tooling is composed of a water-cooled female die and two heated blank holders. The water-cooled upper female die is secured to the upper bed plate. The heated blank holders on the upper die are secured to the water-cooled female die using four bolts on each side of the flange. The bolts used to secure the heated blank holder are not thermally insulated and may transfer some thermal energy between the two thermal zones.

The components of the tooling that are heated for the forming process are the blank holders in the upper die and the binders in the lower die. These parts can be heated to 600°C using cartridge heaters inserted into the tooling components. The heated parts will reduce the cooling rate of the side impact beam flange during the forming and quenching process. Insulating ceramic plates are used to minimize the amount of thermal energy lost to the surrounding water cooled tools and ambient room temperature surroundings, helping to keep the heated parts at the target temperature. The insulation used for this tooling is Zircal-95, manufactured by ZIRCAR Refractory Composites, Inc. (Florida, NY). It has a thermal conductivity of 0.31 W/mK at 200°C, 0.29 W/mK at 400°C, and 0.27 W/mK at 600°C [73]. A 2 mm air gap is used between the water-cooled female upper die and heated blank holders located in the upper tooling. George

24

et al. [9,18] demonstrated that a 1 mm air gap placed between heated and cooled tools in a tailored B-pillar die is sufficient to prevent excessive heat transfer from the heated tools to the water-cooled tools.

2.3.1   Cooling Channels and In-Die Cartridge Heaters

The cooling channels in all of the chilled-water cooled tools are created using drilled holes with a diameter of 17.86 mm. The perimeter of the cooling channels is located at between 12 mm to 21.4 mm from the nearest forming surface that contacts the blank during forming and quenching.

The cartridge heaters are installed in the upper die blank holders and lower die binders. Figure 10 shows the location of the cartridge heaters and thermocouple locations in the blank holders and binder. A total of 32 cartridge heaters are installed in the dies. 16 cartridges are installed in the binders, with 8 cartridges installed on each side. The blank holders also have 8 cartridge heaters installed on each side. The hydraulic press control system has three available electrical power source rated for 30 A at 208 V. The 32 cartridge heaters are divided into three different temperature control zones. The 16 cartridge heaters located in the upper die blank holders are wired into one temperature control zone. The other 16 cartridge heaters installed in the binder were divided into two control zones. The inner eight cartridge heaters are controlled in one zone and the outer eight cartridge heaters are controlled as another zone. The division of the binder cartridge heaters ensures that the middle section of the side impact beam, where most of the deformation in a 3-point bend experiment will take place, is formed with uniform temperature. Each individual circuit can be used continuously using 80% of its maximum current draw. Cartridge heaters rated at 600 W and 300 W were selected for the binder and blank holder heaters respectively. All 32 cartridge heaters installed in the forming dies have a diameter of 19.05mm. The heaters in the binder and blank holders have a length of 101.6mm and 76.2mm respectively. Three thermocouples are used for the temperature control feedback. They are embedded within 5-10mm of the forming contact surface.
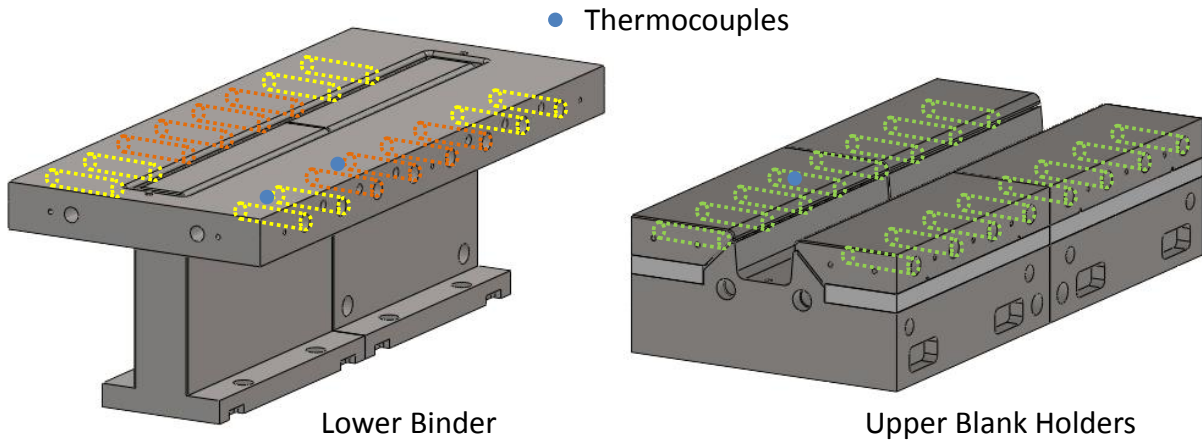
Figure 10: Cartridge heaters location with temperature control zones for blank holders (green), inner binder (orange), and outer binder (yellow).

The differential temperature tooling configuration requires the binder and blank holders to be heated which leads to a requirement to accommodate thermal expansions of the tool sections. Provisions are made in the tooling design [11] to center the various tooling elements along the punch centerline while allowing the tool to expand axially and transverse to the punch centerline.

2.3.2 Furnace

A custom built furnace manufactured by Deltech Inc. (Denver, CO) was used to heat and austenize the blanks prior to forming. The furnace has an overall heating capacity of 18 kW, with inside dimensions of 610 mm x 915 mm x 203 mm (24" x 36" x 8") in width x length x height respectively. A total of six heating elements are installed in the furnace, three at the top and three at the bottom. All six elements are spaced equally to cover the whole area between the front, middle, and back of the furnace uniformly. The six heating elements on the top and bottom of the furnace are grouped in pairs based on location from the door of the furnace to create three temperature controlled sections. This configuration helps the furnace to reach thermal equilibrium throughout the inside of the furnace at the desired temperature even though most of the thermal energy loss is thorough the furnace door. The three different thermal regions are controlled independently; however, they are not insulated from each other inside the furnace.

Figure 11 shows the furnace location behind the hydraulic press. The set up minimizes the travel distance of the blank between furnace and die prior to forming. A platform made of ball rollers between the furnace and press serves to support the hot blank during transfer from the furnace.

26

Figure 11: Furnace and Hydraulic Press equipment set up.

2.3.3 Blank Heating Time

The temperature vs. time history of the blank during austenization in the furnace was measured at three different points on an instrumented blank to ensure uniform heating rate throughout the blank. The three different measured locations correspond to the three temperature controlled zones at the front, middle, and back of the furnace. Three thermocouples were welded to the blank as illustrated in Figure 12, with T1 located at the back of the furnace and T3 located near the front of when the blank is placed inside. The blank is inserted in to the furnace at 930° for five minutes, the amount of time required to austenize a blank prior to forming. The temperature vs. time histories of the three thermocouples were recorded and are shown in Figure 12. The figure shows that the blank was heated evenly within the three different temperature control zones in the furnace.
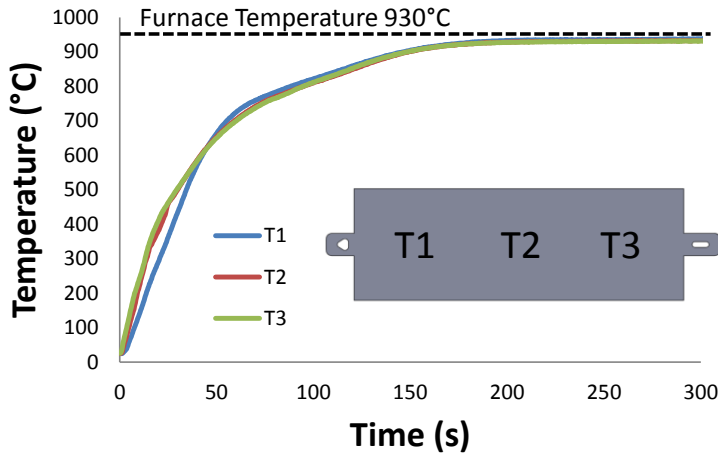
Figure 12: Temperature-time history of an instrumented blank during austenization. Thermocouple locations as sown in the blank illustration.

2.3.4 Press Frame & Hydraulics

The parts were formed in an existing hydraulic press manufactured by Macrodyne Technologies Inc. which has a total bed size of 1372 mm by 762 mm. The press has a 120 ton actuator which allows a relatively fast forming speed for hot stamping [9]. A 100 GPM servo valve and two 15 gallon hydraulic accumulators allow the press to move at 254 mm/sec [9]. This minimizes the time required in the die to form the side impact beam to approximately one second, completely forming the part before the austenized blanks begin to transform into other phases.

The press uses a closed-loop position control algorithm with an MTS FlexTest servo controller and program signal is generated with a PC-based Digital-to-Analog card driven by a custom LabVIEW program. The hydraulic press has a string potentiometer for displacement feedback. Pressure transducers are installed at the hydraulic fluid inlet and outlet of the actuator. Press force is calculated based on the pressure recorded and differences in cylinder areas. The measured load is recorded using Analog-to-Digital channels on the same DAQ card used by the controller.

2.3.5 Transfer System

A universal transfer system, developed by George et al. [36] and shown in Figure 13 was used to transport blanks into and out of the furnace. The system uses a platform cart mounted on two horizontal linear bearing rails to slide a gripper system through the open die and reach into the furnace. The transfer system is designed to grab a blank using a gripper head and move it into and out of the furnace, and into the die for forming. The gripper tongue is lined with a layer of ceramic insulation to minimize heat transfer between the gripper and the heated blanks during a blank transfer.
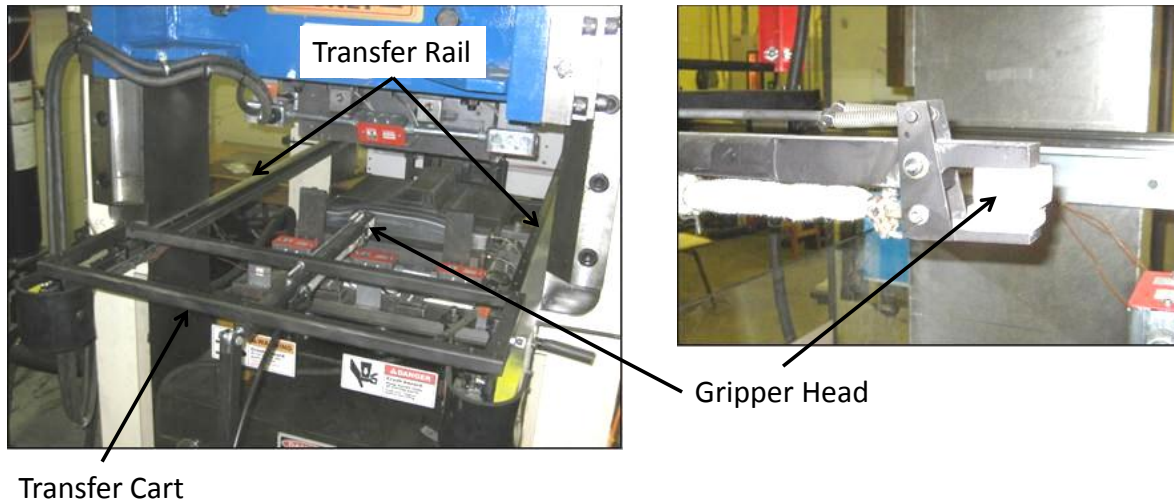
Figure 13: Transfer system.

2.3.6 Blank Design

The side impact beam is formed using a precut blank with a nominal dimension of 200 mm by 590 mm (Figure 14). Two small rectangular tabs are added to both ends of the blank, to aide with alignment of the blank prior to forming. These two tabs contain either a triangular cut out or a slotted hole that align the blank on two alignment pins installed long the die center line. The blanks were produced using water-jet cutting to prevent any heat-affected zone being introduced in the blank prior to austenization.
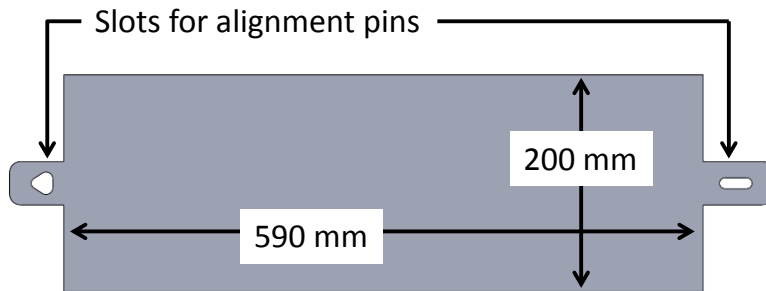
Figure 14: Blank design.

2.4 Forming Process

Prior to forming, the blank is inserted into the furnace set at 930°C for 5 minutes for austenization. After this time, the operator uses the transfer mechanism to grab the tab of the blank, removing it from the furnace and resting the blank on the spherical steel roller table for five seconds. This duration simulates the time period in industrial hot stamping during which a robotic transfer system would handle and position the blank prior to forming. Some heat loss occurs from the blank to the spherical steel rollers as the blank is transferred into the die over the ball roller platform, but the small contact area minimizes the

amount of heat loss through direct contact. The blank is then pulled further into the forming die until the blank catches the alignment pins and falls into place in the forming tool. The forming step is triggered automatically once the transfer mechanism is pulled back out of the die by the operator.

The forming operation is controlled by a custom LabVIEW software program. The displacement and applied force vs. time of the hydraulic press is shown in Figure 15. The program requires input for forming distance, forming time, and quench time. The upper die always starts at a pre-set zero position, which is an approximately 220 mm above the fully closed die position. The press is set to travel 5 mm past the bottom dead center position to ensure a fully closed position during quenching. Once the upper die reaches the fully closed position, the hydraulic press will ramp up to apply the maximum force of 891 kN on the closed tooling. It takes the press one second to reach the blank, one second to form the blank, reaching the fully closed position. The quench time (a hold period with the die closed under load) is set to either 4 or 10 seconds. At the end of the quenching period the upper die will retract to the pre-set zero position in approximately 1.5 seconds.
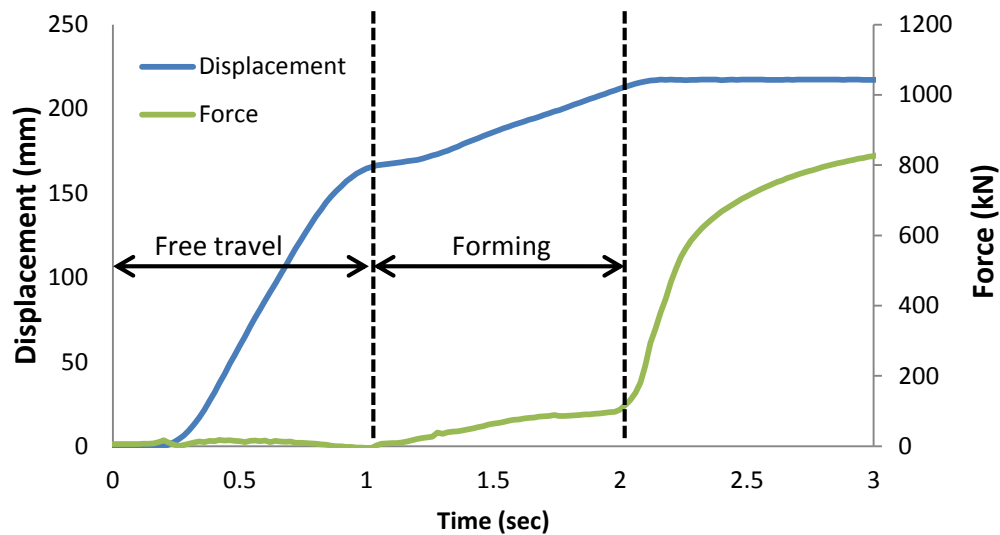
Figure 15: Side impact beam forming punch force and displacement.

Transferring the formed blanks out of the forming die must be done quickly to avoid any additional unwanted heat transfer between the formed side impact beam and the die. The tailored flange should not come into further contact with any part of the cooled punch. Two spring loaded ejector pins were installed in the upper female die opening to assist with preventing the part from becoming stuck onto the upper die. The operator removes the formed blank and places it on metal blocks located under the alignment tabs where it continues cooling for about five minutes during which the part reaches room temperature.

2.5 Samples for Mechanical Characterization

Hardness and tensile samples were extracted from selected as-formed parts at the locations illustrated in Figure 16. Hardness measurements of the tailored side impact beam were taken to confirm that significant difference in hardness between the fully martensitic top hat region and softened flange was achieved. Hardness values in the sidewall region were also acquired to characterize the transition zone in the tailored parts. Five 20 mm strips were cut along the cross sections at the ends and at every quarter-length locations for hardness measurements along the cross section. Tensile specimens were taken from flange, sidewall, and flat top locations between the hardness sample strips for tensile characterization of the mechanical properties after tailored hot forming.
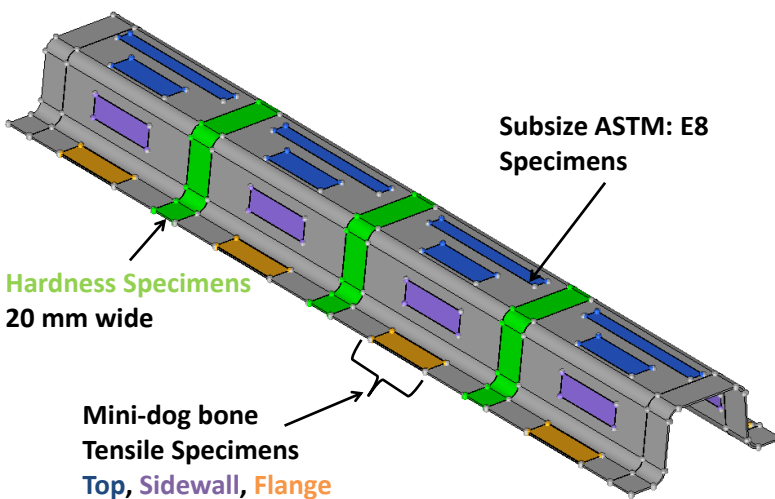
Figure 16: Laser cut samples from top hat side impact beam for Vickers micro hardness measurement and tensile specimens (ASTM: E8 subsize and mini-dog bone).

Side impact beams of all forming conditions were sent to Promatek Research Centre for laser cutting to produce hardness and tensile specimen blanks. The laser cut samples were sectioned using a 5-axis laser cell. The samples were left attached to the formed side impact beam using a small tab. The samples were labeled prior to removal from the beams by breaking the tabs.

2.5.1 Sample Preparation for Hardness Measurements

The laser cut hardness specimens are further cut into five smaller regions from the flange, bottom corner, sidewall, top corner, and top using a wet saw. Only one side of the hardness specimen strip is used with the assumption that the hardness values are symmetrical along the centerline. The five regions are then cut along the centerline of the original hardness specimen strip exposing the surface used for micro hardness measurement that is away from the laser cut HAZ location. The specimens are then held together with a binder clip and mounted in a puck with a diameter of 25 mm using a mixture of cold-

setting epoxy resin and a hardener solution. Figure 17 shows the steps for mounting the specimens in a resin puck. The mounted pucks are then polished with an automated machine using SiC paper up to 2000 grit to produce a mirror finish under the microscope of the hardness testing equipment. A clean surface without any visible scratch under the microscope is important to allow the operator to measure the size of the hardness indentation precisely. Figure 17 also shows the mounting order of a resin puck prepared for Vickers micro hardness measurement.
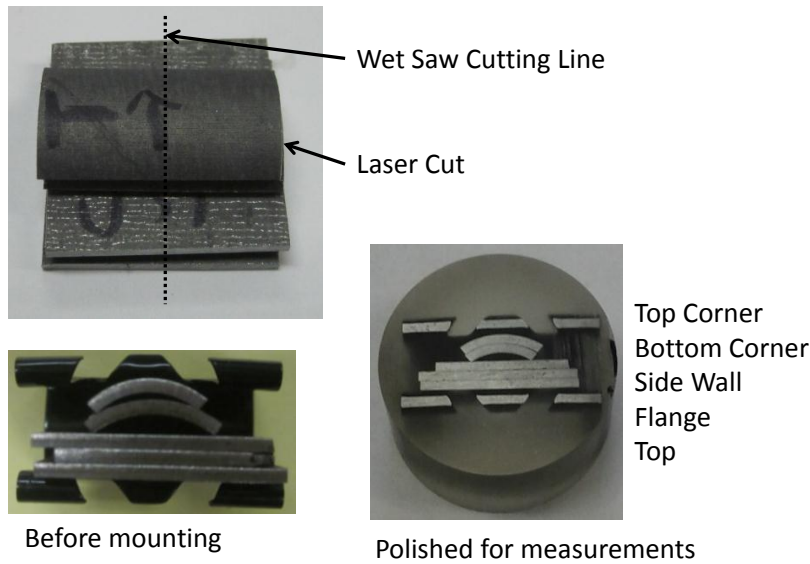
Figure 17: Hardness puck mounting preparation.

Hardness measurements were taken using a LECO MHT Series 200 hardness tester. The machine indents the sample with a diamond shaped indenter at a specified force of 1000 g. The tester has an optical lens that is calibrated to take an inline distance measurement between two points. Figure 18 shows an indentation mark for Vickers hardness measurement made on a flat and level surface with two almost identical diagonal distances.
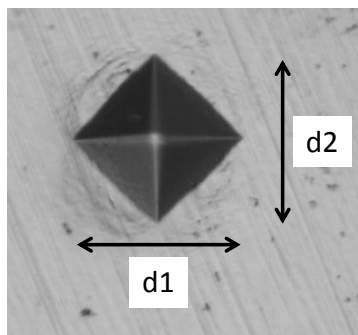
Figure 18: Optical micrograph of a Vickers micro hardness indentation on a flat and level surface.
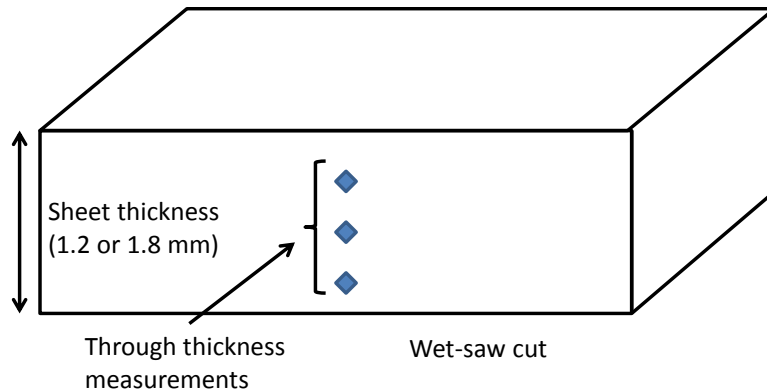
Figure 19: Through thickness hardness measurement details.

Three hardness measurements were taken through the thickness of the samples at each location. Figure 19 shows the details of the measurements taken at each location and provides the orientation of a measured sample. Each forming condition had one puck that had its hardness measured with more detail. The first puck of each forming condition had a measurement taken at a distance interval of 2.5 mm (0.1") starting the edge of the flange towards the flat top hat section. The wet saw disc cutter has a thickness of 1.5 mm that will create gaps between each section. To make the measurements consistent for every puck, the distance from the edge of the flange was reset for each new section and measurements continue at the same interval.

2.6 3-Point Bend Specimen Configurations

The as-formed 1.2 mm and 1.8 mm specimens are spot welded to backing plates in preparation for the 3-point bend experiments. The backing plate is made from 1.2 mm JAC590R steel supplied by ArcelorMittal. Both full back plate and a split back configurations are used in this study as illustrated in Figure 20. The full back plate specimen has a formed side impact beam welded to a single continuous backing plate with a dimension of 600mm by 125mm. This configuration completely covers the flange along the length and width of a side impact beam. Each flange has a total of 12 spot welds placed at 50 mm intervals. The four spot welds at the center are located 25 mm from the centerline of the beam. The split back plate configuration uses two smaller backing plates measuring 225 mm by 125 mm creating a 150 mm gap at the center of the beam. The spot weld closest to the end of the beam is placed 25 mm from the edge. The rest of the spot welds are placed at 50 mm intervals. The purpose of the split back plate configuration is to ensure direct loading of the flange region under the load point without the influence of the supporting backing plate.
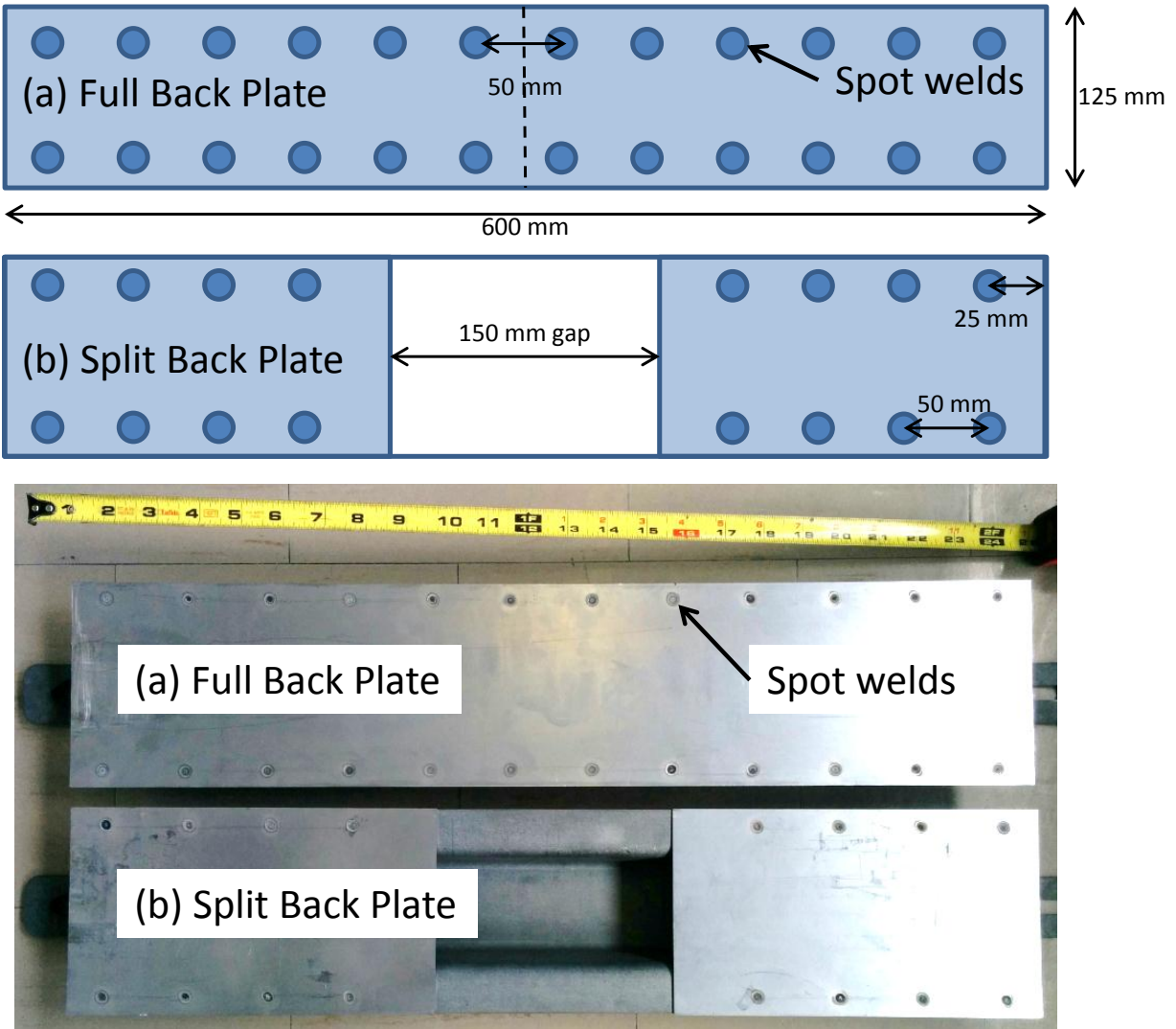
Figure 20: Spot welding configuration of (a) full and (b) split back plate side impact beam (not to scale).

2.7   3-Point Bend Quasi-Static and Dynamic Experiments

The spot welded side impact beams are tested in a 3-point bend configuration in quasi-static (Figure 21) and dynamic (Figure 22) experiments. The force vs. displacement response of the different tailored beams will be used to ascertain the effect of tailoring in the flange region during a crash event. The experiments will also be used to assess the numerical models of the forming and 3-point bending operations, described in Chapter 4.
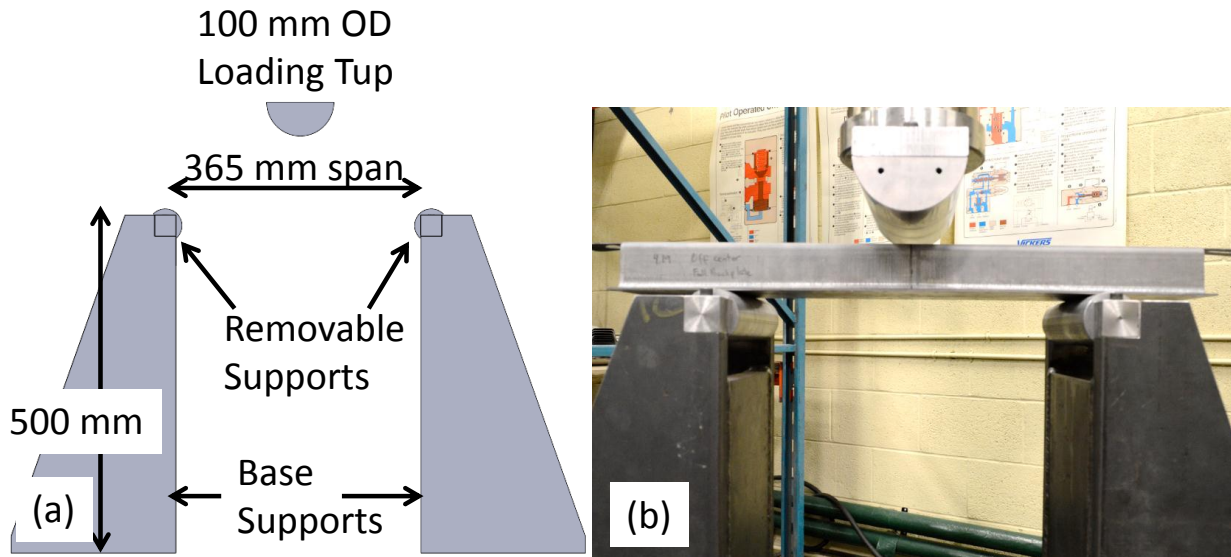
Figure 21: (a) 3-Point bend experiment setup and (b) quasi-static 3-point bend experiment setup.

2.7.1   Quasi-Static Experiments

The side impact beam is supported by two 50 mm (2") outer diameter cylindrical supports made from 4140 cold rolled steel machined to a smooth surface finish. The two rod supports are placed with a center to center span of 365 mm. Each support has a length of 177.8 mm (7") that can be used to contact the 125 mm width of side impact beam during the 3-point bend test. The base supports have a total height of 500 mm, required to provide enough space below the initial contact position to accommodate the deformation of the side impact beam. Figure 21 shows the basic set up of the 3-point bend experiments with the picture on the right showing the quasi-static experiment set up.

The "impactor" or loading tup for the 3-point bend experiment is made from 100 mm outer diameter 4140 hot rolled steel cut into two half cylinders and was machined to a smooth surface finish. The impactors were carburized to improve hardness of the surface to prevent surface damage during 3-point bend testing. The impactor is mounted to the hydraulic press using a mounting plate and a cylindrical adapter plate to mount to the load cell.

The hydraulic press system is capable of exerting a peak force of 496,000 N or 111,000 lbf in compression load. The hydraulic press is controlled by an MTS FlexTest servo controller with program signals generated by a PC-based Digital-to-Analog card driven by a custom LabVIEW program. The press cylinder can be retracted and extended using displacement control or force control, chosen by the operator. For the quasi-static deformation of the side impact beam, the impactor was programmed to deform the beam at a constant velocity of 0.76 mm/s (0.03 inch/s). The force response is measured using

a load cell. The force and displacement responses are collected for the quasi-static experiment with a frequency of 4 Hz for both force and displacement.

The test matrix for quasi-static 3-point bend experiments is shown in Table 4. The experiments consider specimens formed at all of the binder temperatures, both quenching periods, and both backing plate configurations.

Table 4: Quasi-static 3-point bend test matrix for 1.2 mm and 1.8 mm side impact beams.

Forming Flange Temperature (°C)	Quench Time (seconds)	Backing Plate
25	4	Full
		Split
	10	Full
		Split
400	4	Full
		Split
	10	Full
		Split
600	4	Full
		Split
	10	Full
		Split

2.7.2   Dynamic Experiments

The dynamic experiments were performed for a smaller test matrix since the cost for each experiment was significantly higher than for the quasi-static experiments. Fully martensitic and tailored beams formed with heated die regions at 600°C and both full and split backing plate configurations were tested. Tailored beams formed with a 400°C flange region were not tested to reduce cost and because the difference in peak force is very small (Section 4.2). In addition, the dynamic experiments were limited to a material thickness of 1.2 mm and a hold quenching period of four seconds. The test matrix for dynamic experiments is shown in Table 5.

Table 5: High-speed impact 3-point bend test matrix for 1.2 mm side impact beams formed with a 4 second quenching period.

Forming Flange Temperature (°C)	Backing Plate
25	Full
	Split
600	Full
	Split

The dynamic experiments were conducted at the University of Waterloo crash lab. The layout of the dynamic experiments is illustrated in Figure 22. This experiment was done with the same general loading arrangement as the quasi-static experiments; however, the dynamic experiments were done in a horizontal orientation. The "impactor" or loading tup and base supports were those used in the quasi-static experiments. For the dynamic experiments, the specimen and base supports were mounted on the moving sled wall and the loading tup and load cells were mounted on the fixed barrier wall.
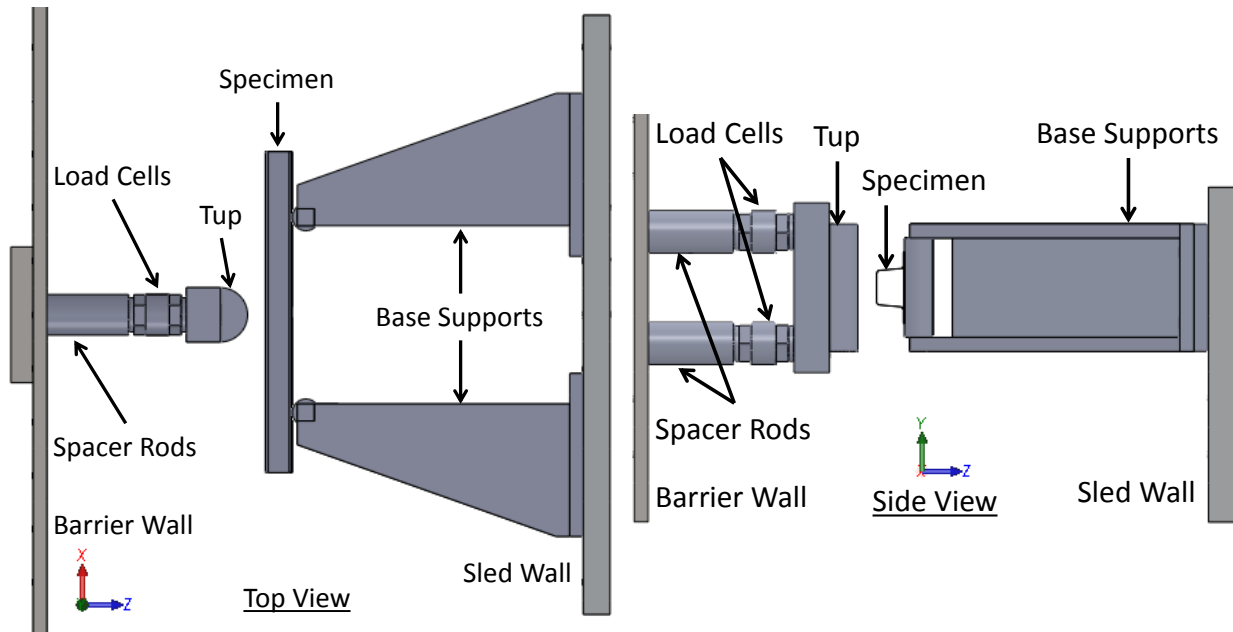
Figure 22: CAD layout of the high-speed 3-point bend experiment from Top View and Side View.

The barrier wall assembly comprising the impactor, adapter plate, and load cells set up is shown in Figure 23. On the barrier wall, two load cells are mounted onto spacer rods. The spacer rods are required to increase the distance between the impactor contact surface and the barrier wall, providing sufficient stand-off distance for the sled to stop safely during deceleration without contacting the barrier wall and

causing equipment damage. The load cell is also mounted away from the barrier wall to reduce the amount of potential bending moment that can damage the load cells.

Reducing the amount of vibration in the system is important to reduce mechanical ringing and improve the force vs. time data recorded by the load cells. A sheet of 1" thick plywood is installed as a damping element between the impactor and adapter plate, as shown in Figure 23.
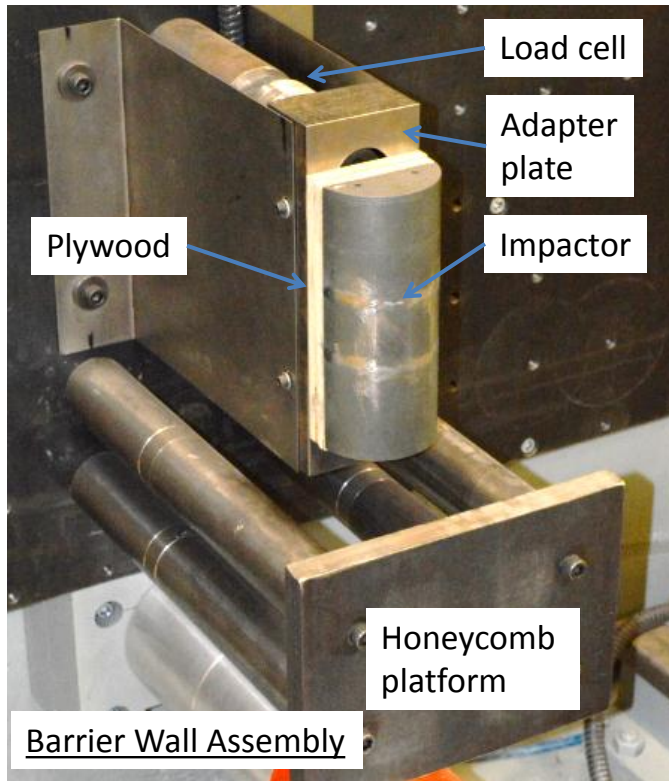
Figure 23: Barrier wall assembly for dynamic experiments.

The base supports and rod supports used in the quasi-static experiments are mounted on the sled wall (Figure 24). The over-hanging weight of the base supports on the sled wall is not ideal, but allows the tup and load cells to be mounted on the stationary wall which greatly simplifies data acquisition. From the quasi-static results, a peak force of approximately 25 kN is expected from the strongest, fully martensitic parts. This peak force is less than 10% of the load rating of a single load cell. The mounting configuration with two load cells on the barrier wall was chosen to reduce the potential of the load cell being overloaded in bending and shear modes. The overall mass of the sled, specimen and support assembly was 980 kg and the velocity of the sled is approximately 22 km/h (6.11 m/s).
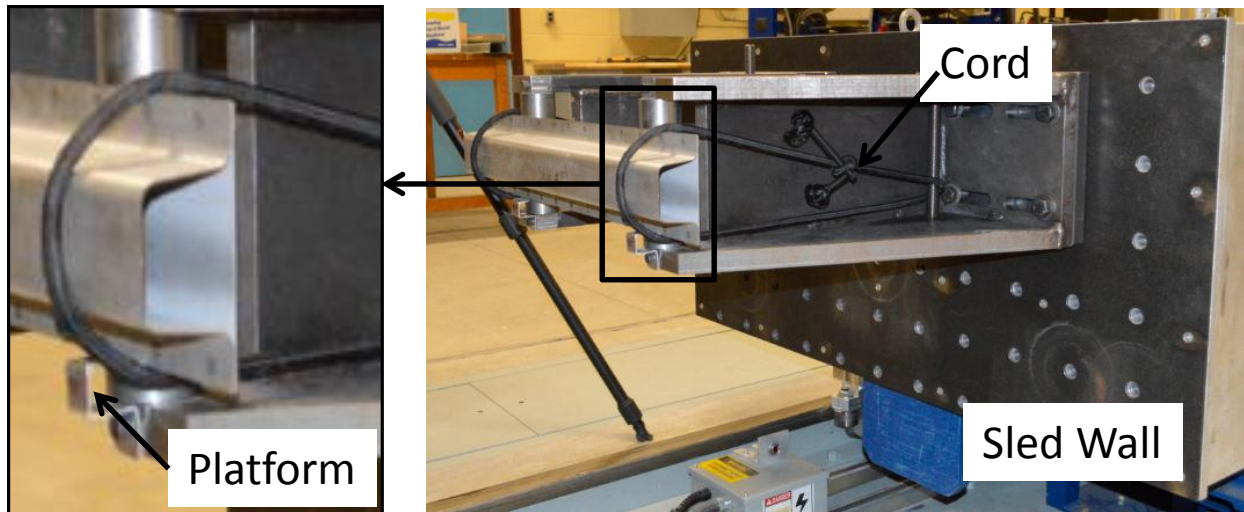
Figure 24: Sled wall assembly for dynamic experiments.

Due to the orientation of the test, the side impact beam must be supported to stay aligned with the support rods while the impact sled accelerates to 22 km/h. This was achieved by installing a small platform made out of aluminum sheet metal (Figure 24). The sheet metal platform is attached on to the fasteners used to secure the removable support rods to the base supports. The side impact beam is then secured to the support base using an elastic cord (bungee) looped from the base and over the ends of the side impact beam outside of the support span. The bungee cord provides support to prevent the side impact beam from falling away from the platform while the sled is travelling towards the barrier wall. The force applied by the bungee cord will resist the beam from bending; however, this effect is negligible compared to the force recorded during the test.

2.7.3   High-Speed Camera and Dynamic Specimen

Capturing the deformation of the side impact beam under dynamic conditions is important to know how the specimen responds to the impact. Two high speed cameras with an image acquisition frequency set to 10,000 Hz were used to capture the deformation during the dynamic experiments. One camera is located right above the experiment capturing a top view of all tests (Figure 25). The top view for the impact test is the same as the front view for the quasi-static test. A second camera is located at the side of the barrier wall placed slightly above the impact location to capture an angled side view. This view will capture the initial deformation of a side impact beam before its view is blocked by the moving base supports as the sled advances.
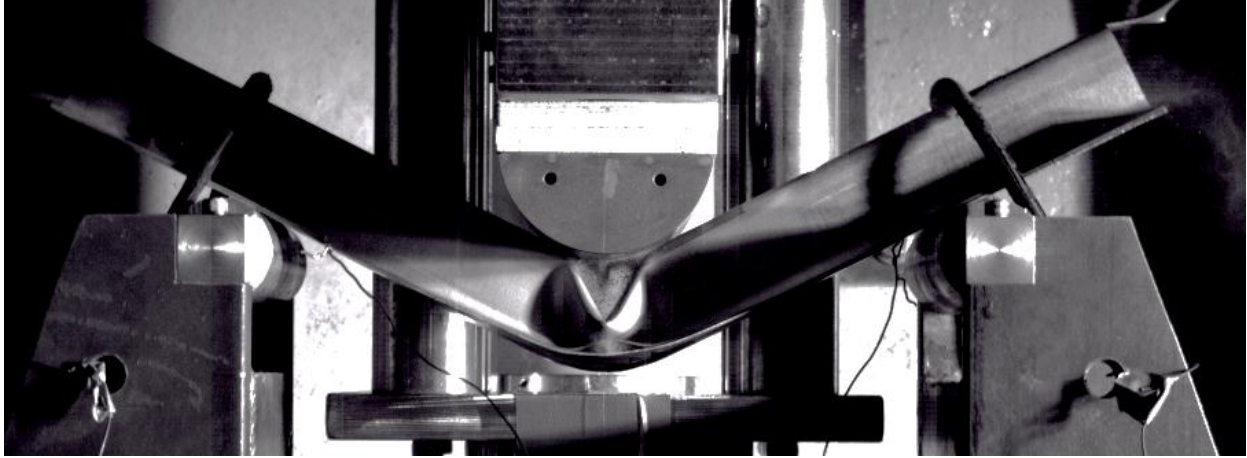
Figure 25: Top view from a high speed camera of a 3-point bend sandblasted side impact experiment.

During dynamic testing of the hot formed Usibor® 1500-AS, its brittle aluminum-silicon (Al-Si) coating spalls off the sheet metal substrate, forming a dust cloud during crash deformation. In quasi-static experiments, the coating comes off at a slow rate and the coating dust does not interfere with the camera view. Under high speed impact conditions, a larger cloud of dust obscures the camera view. To reduce the amount of dust during high speed impact, some coating near the impact and deformation site was removed by sand blasting the affected area. From an initial test, most of the coating layer that comes off to create a cloud dust comes from the side wall and flange surface near the impact site. The layer of coating that covers the side wall area in the center of the side impact beam was also sandblasted to remove the Al-Si coating. The flat top surface that comes into contact with the impactor was not sand blasted to keep the same friction condition as the quasi-static experiments. Masking tape and duct tape were used to mask these areas during sandblasting. The sandblasted and non-sandblasted areas are shown in Figure 26.
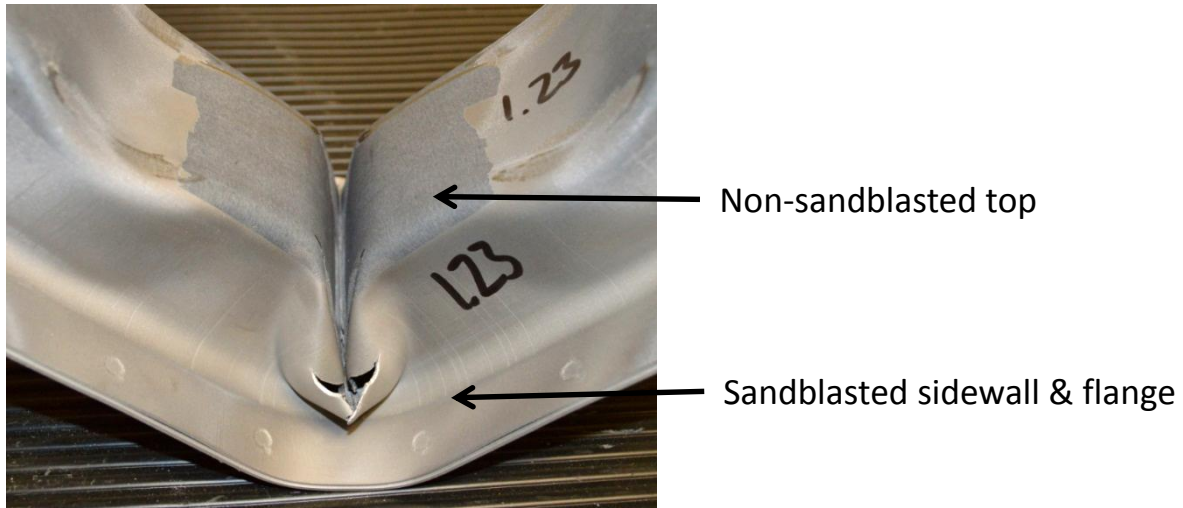
Figure 26: Sandblasted side impact beam after high speed 3-point bend experiment.

The side impact beams with a full back plate configuration are sand blasted only on the outside surface area. Split back plate side impact beams are also sand blasted on the inside of the beam through the split back plate opening to remove coating on the inside to reduce the amount Al-Si coating that would produce a cloud dust during a test.

3 Numerical Simulation

The forming and 3-point bend experiments were modeled using the LS-DYNA finite element software version 971 Revision 7 [54]. The forming simulation is divided into five stages as outlined in this chapter. The multiple simulations comprise: (i) steady-state temperature distribution in the tooling; (ii) air cooling during transfer between the press and tooling; (iii) forming of the part; (iv) cooling within the die (hold time); (v) air cooling after removal from the die; and, (vi) dynamic or quasi-static 3-point bend testing. These simulations each require different formulations (thermal, structural or both) and are run separately in stages to reduce computing cost and overall simulation time. Section 3.1 describes the first five simulation stages representing the forming part of this study. Section 3.2 describes the 3-point bend simulations with either quasi-static or dynamic loading conditions.

3.1 Hot Forming Process Simulation

3.1.1 Tooling Mesh and Material Properties for the Tooling Components

The forming tool is meshed using rigid 8-noded brick elements that will represent both the steel tooling and ceramic insulation. Both materials are modeled using an isotropic material model with different thermal and mechanical properties. The steel tooling physical properties are listed in Table 6 and the ceramic insulation properties are listed in Table 7.

Table 6: Steel material property.

Property	Value
Density	7890 kg/m^3
Young's Modulus	200 GPa
Poisson's Ratio	0.3
Specific Heat Capacity	0.519 kJ/kg-K
Thermal Conductivity	37.7 W/m-K

Table 7: Zircal-95 ceramic insulation material properties from [73].

Property	Value
Density	1400 kg/m^3
Specific Heat Capacity	11.72 kJ/kg-K
Thermal Conductivity	0.6 W/m-k

Both of the ceramic insulation and steel tools were meshed using rigid solid elements. The solid elements are required to predict the temperature distribution in the tool during the forming and quenching stage. The mesh made for the simulations has been simplified by excluding the fasteners required for assembling the tools together for the experiments. Only the female die, punch, blank holders, binder, and ceramic insulations are represented in the model. The model uses a quarter symmetry boundary condition to reduce the overall running time of the simulations. Figure 27 shows a full mesh of a model that has been reduced to a quarter symmetry condition.
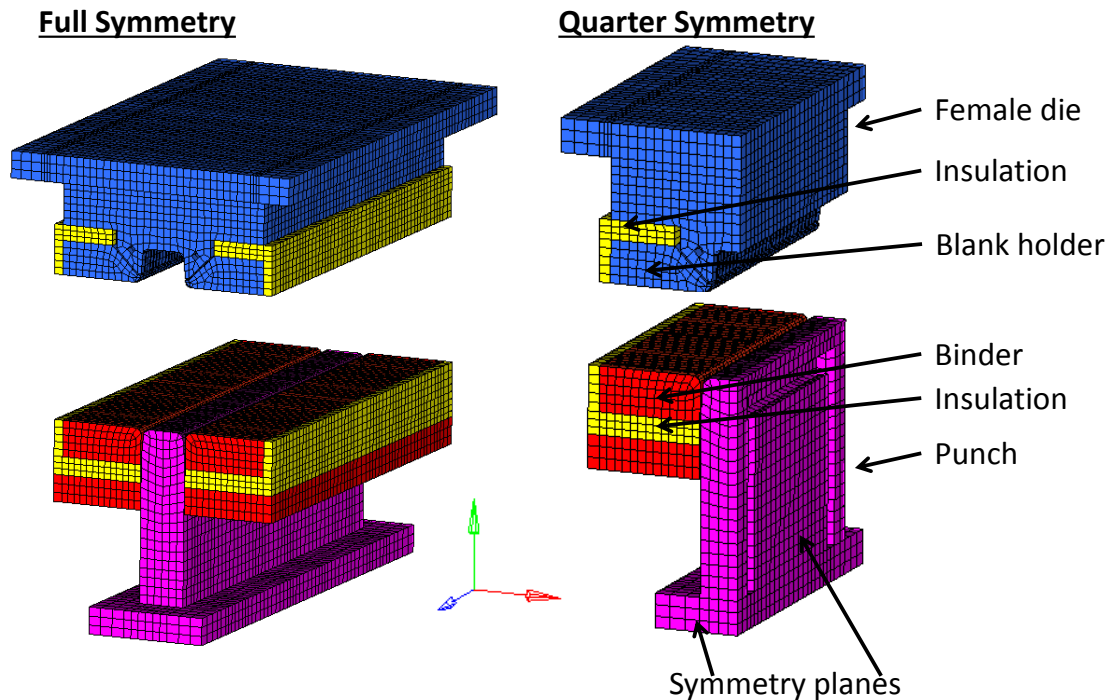
Figure 27: Full and quarter-symmetry models of the meshed tool.

The bulk of the tooling is represented in the mesh using rigid solid elements with a relatively large element size of 10 mm. This large element size will not capture the corner radius regions of the top hat cross section when the blank is formed. To better predict the final shape of the blank after forming, the large solid elements that contact the blank are blanketed with smaller rigid shell elements which are used to enforce the contact condition with the work piece. The shell elements that represent the contact surface of the tooling in the corner region are meshed with an element size of 1 mm. The rigid shell and solid elements that form the punch and its contact surface with the blank are shown in Figure 28. Additionally, the same method is applied to the forming surfaces of the binder and the upper die. These blanketing elements are given a zero thickness value to keep the proper top hat cross section.

43
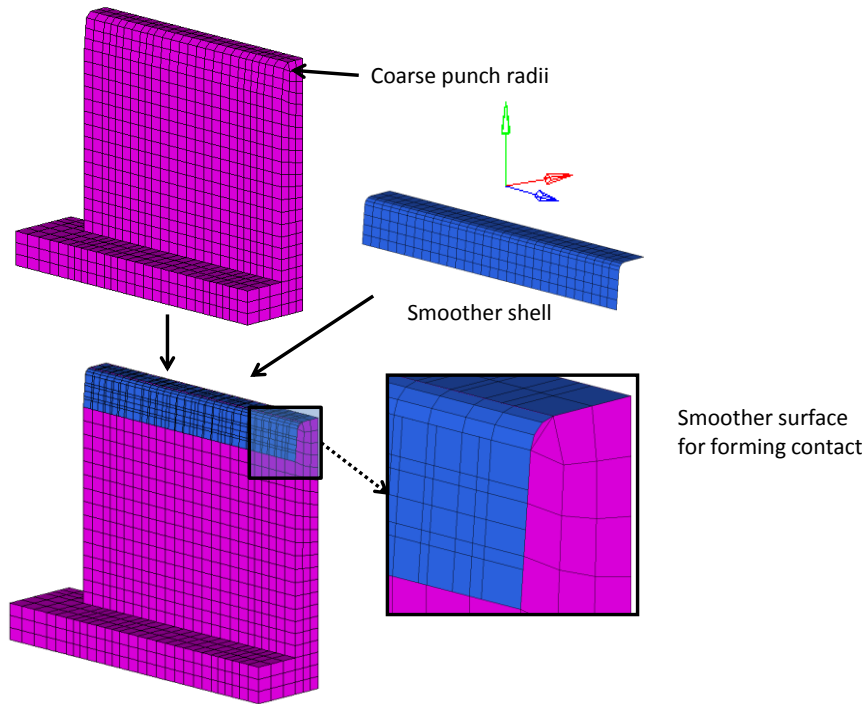
Figure 28: Shell elements tied with solid elements of the punch with quarter symmetry.

The fine shell elements and large brick elements are tied together thermally using the keyword *CONTACT_TIED_SURFACE_TO_SURFACE_OFFSET_THERMAL. This keyword ensures that the fine shell elements have the same temperature distribution as the temperature distribution predicted by the thermal boundary conditions applied to the solid elements of the tooling and insulation. The thermal boundary conditions of the forming simulation are explained in Section 3.1.2.

3.1.2   Thermal Boundary Conditions

All tooling surfaces that face the ambient room temperature air are given a boundary convection and a boundary radiation condition to simulate thermal energy loss to the surrounding environment. This corresponds to the method used for the cooling of an austenized blank in free air. The convection and radiation HTC vs. surface temperature is listed in Table 8 and Table 9 respectively [9].

Table 8: Convection HTC vs. temperature [9].

Temperature (K)	HTC (W/m^2-K)
100	4.93
302	4.96
502	12.23
702	13.38
1102	13.70
1502	13.37

Table 9: Radiation factor vs. temperature [9].

Temperature (K)	HTC (W/m^2-K^4)
0	0
100	0.5
373	0.5
648	0.65
873	0.7
1200	0.7
1300	0.7

The cooling channels and cartridge heaters in the die are simulated by removing solid elements from the meshed tooling at the location of drilled holes and channels. A constant boundary temperature of 25°C is specified on all nodes on the surfaces of the cooling channels. There is enough circulating chilled water to assume that the temperature of the circulating water at the tooling outlet is close to 25°C. The heat flux from the cartridge heaters is simulated using surface segments defined on the surface of the elements that have been removed where the cartridge heaters are to be inserted. The surface segments are given a constant boundary flux set as an input. The boundary flux is set to an amount that will provide enough thermal energy to the heated tools to stay at either 400°C or 600°C on the contact surface during a thermal steady state simulation, matching the experimental conditions. Figure 10 shows the location of the heater cartridges in the blank holders and the binder. A unique surface segment ID is created for each cartridge. This allows segments to be given a unique load curve defining the required heat flux. Three unique load curves are defined to represent the three regions of PID controlled cartridge heaters described in Section 2.3.1, to ensure each group of heaters applies the same amount of heat flux in the simulation. The thermal boundary condition used to simulate the forming of the fully hardened parts (heaters turned off) is done by removing the boundary thermal flux on the heated dies and giving all of the nodes for the tooling an initial temperature of 25°C.

The thermal boundary condition between the heated blank holder and cooled female die is simulated using boundary surface segments. The mesh of the heated and cooled die has a gap with a width of 2 mm that has been proven to be efficient to act as a thermal insulator to be used in hot stamping technology studied by George [9]. The surface on the heated blank holder that faces the cooled female die has a simulated radiation thermal boundary condition with a surrounding environment at a temperature of 25°C. The same technique is applied to the surface of the cooled female die facing the blank holder at a temperature of 400°C or 600°C. In the forming of a fully hardened side impact beam, the radiation heat transfer card is turned off and the temperatures of the two surfaces are assumed to be nearly identical. The same method is also applied between surfaces on the cooled punch and heated binder that are facing each other. Figure 29 shows the air gap between the heated flange holder and cooled female die highlighted with a red line. Also shown is the ceramic insulation in between the heated and cooled sections.
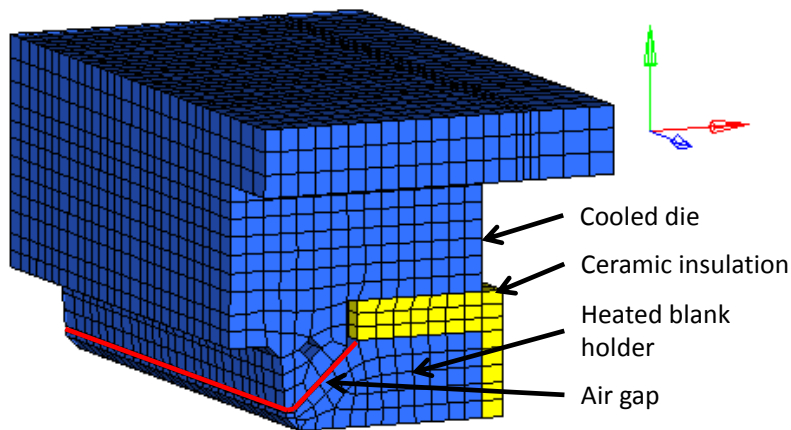
Figure 29: Insulation and air gap (highlighted in red) between heated flange holder and cooled female die.

3.1.3   Forming Simulation Contact Parameters

The contact conditions between the blank and the tooling dies were simulated using the *CONTACT_SURFACE_TO_SURFACE_THERMAL_FRICTION_ID keyword card. The input for this card specifies the coefficient of friction and the thermal condition between the die forming surfaces and the blank. The coefficient of friction between the blank and the forming die is set to 0.4 as recommended by Hora [67] and used by George et al. [9,18]. The rigid shell and solid elements that represent the contact surfaces of the tooling are thermally tied to each other as explained in Section 3.1.1. The thermal conductivity between the blank shell elements and the tool rigid shell elements is simulated using a heat transfer coefficient as a function of pressure based on the work of George et al. [18]. The HTC value vs. pressure used in this work is shown in Figure 30.
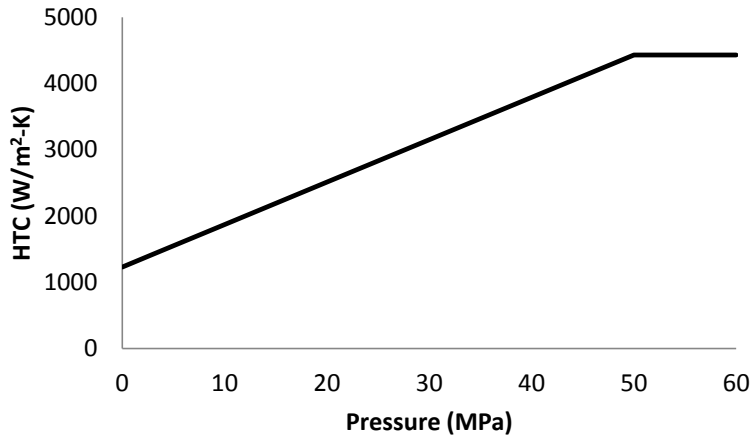
Figure 30: HTC vs. pressure for the blank to tooling contact heat transfer [18].

3.1.4   Blank Mesh Design

The blank is meshed using deformable quadrilateral shell elements with a size of 2.5 mm by 2.5 mm (Figure 31), which is consistent with industrial crashworthiness simulation practice. The overall original blank size is 200 mm by 600 mm which has been reduced to 100 mm by 300 mm due to the use of quarter symmetry condition. This is the size of the blank at the beginning of the transfer simulation with an austenization temperature of 930°C. The blank will shrink as it cools down during the forming simulations due to thermal expansion. The blank is meshed without the slotted alignment holes shown in Figure 14 to simplify the numerical computation.
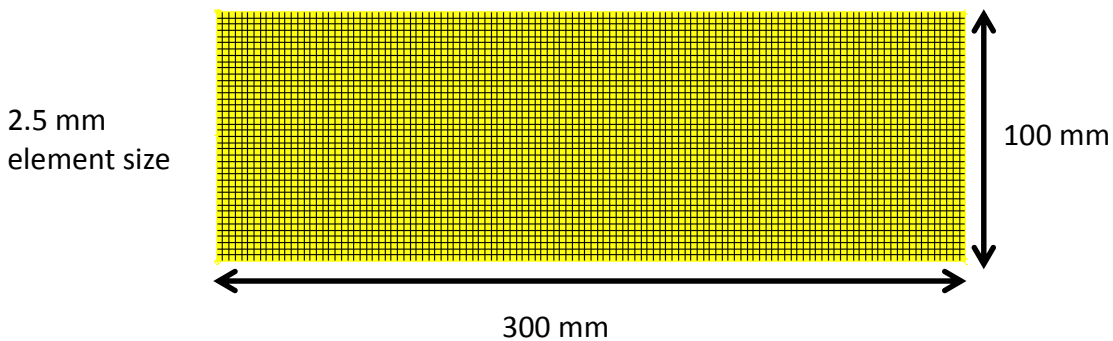
Figure 31: Blank mesh.

3.1.5   Blank Material Properties and Definition

The *MAT_UHS_STEEL or *MAT_244 from LS-DYNA is the material model used for simulating hot forming of boron steel. This model was developed by LS-DYNA based on the work of Akerstrom [46] at the University of Lulea, Sweden. The model is capable of predicting the transformation of austenite to form martensite, bainite, ferrite, and pearlite as the blank cools. The model also predicts the final Vickers

micro hardness and resulting yield strength based on steel composition and the instantaneous cooling rate at 700°C [48]. The physical properties of boron steel sheet metal are listed in Table 10. The material model requires many other parameters to define the material behaviour including composition percentage, phase activation energies, latent heat, and flow curves for each of the microstructure phases. The input parameters for the boron steel material model used in this work are due to Shapiro [44] and George et al. [18].

Table 10: Material Properties [5].

Property	Value
Density	7890 kg/m^3
Young's Modulus	200 GPa
Poisson's Ratio	0.3
Specific Heat Capacity	0.65 kJ/kg-K
Thermal Conductivity	32 W/m-K

There are five different hardening curves for each of the microstructure phases used in the forming simulation. These hardening curves are used to predict the mechanical behaviour of the blank during forming as the austenite phase is being transformed into one of its daughter phases depending on the cooling rate of each element and its current phase composition.
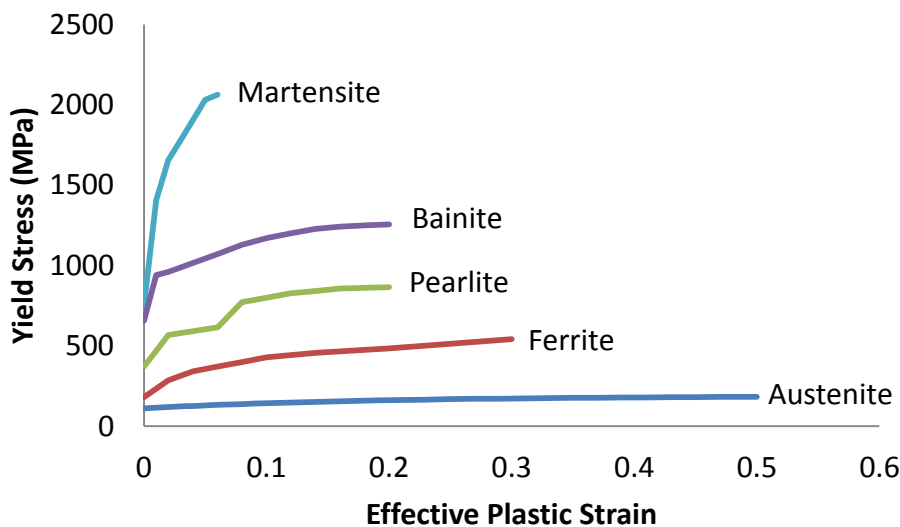
Figure 32: Hardening curves for the microstructure phases during the forming simulation.

The material model of a hot formed boron steel uses equation (1) to calculate the hardness of the individual elements. The hardness vs. temperature of bainite and martensite are input into the material model and are shown in Figure 33 and Figure 34, respectively. To detect any hold time in the temperature-time history of any element, the critical cooling rate was set to 2 seconds with a sampling rate of 0.5 seconds.
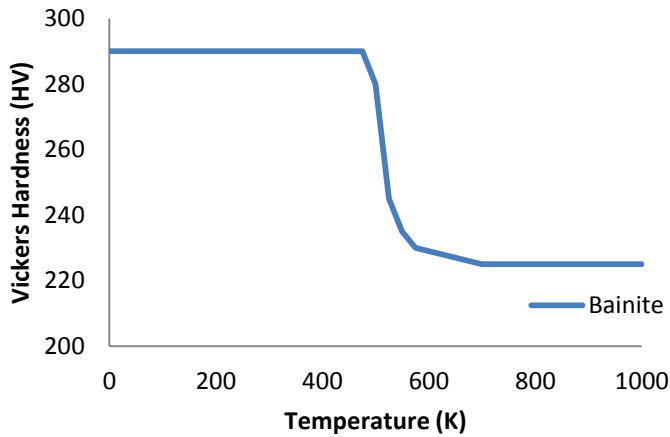
Figure 33: Bainite hardness vs. temperature.
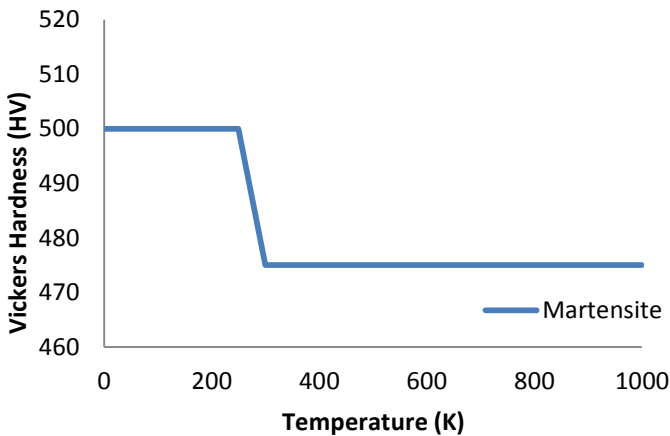
Figure 34: Martensite hardness vs. temperature.

The latest implementation of the material model in LS-DYNA allows the user to scale the activation energies for the daughter phases of austenite as a function of effective plastic strain. The CCT diagram for 22MnB5 steel (Figure 1) shifts to the left when plastic deformation is introduced to the material during the cooling of the formed part [8]. To account for this effect, the activation energy scaling factors determined by George et al. [74] were adopted. The activation energies for transformation of ferrite/pearlite and bainite are given in Table 11 and Table 12, respectively.

Table 11: Scaling factor of activation energy vs. effective plastic strain for ferrite/pearlite [74].

Effective Plastic Strain	Scaling Factor
0	1
0.2	0.491
0.5	0.491

Table 12: Scaling factor of activation energy vs. effective plastic strain for bainite [74].

Effective Plastic Strain	Scaling Factor
0	1
0.2	0.958
0.5	0.958

3.1.6 Forming Simulation

The experimental forming operation has been divided into five different individual simulations to reduce simulation time. The five simulation stages for the forming process comprise: establishing the steady-state temperature distribution in the tooling; air cooling during transfer between the furnace and tooling; forming of the part; quenching within the die; and air cooling after removal from the die. The forming process is broken into these five simulations to allow for different mass scaling to be used to improve the overall running time of the whole forming simulation (mass scaling is described below). Figure 35 shows the five different forming simulation stages that represent the actual forming experiments.
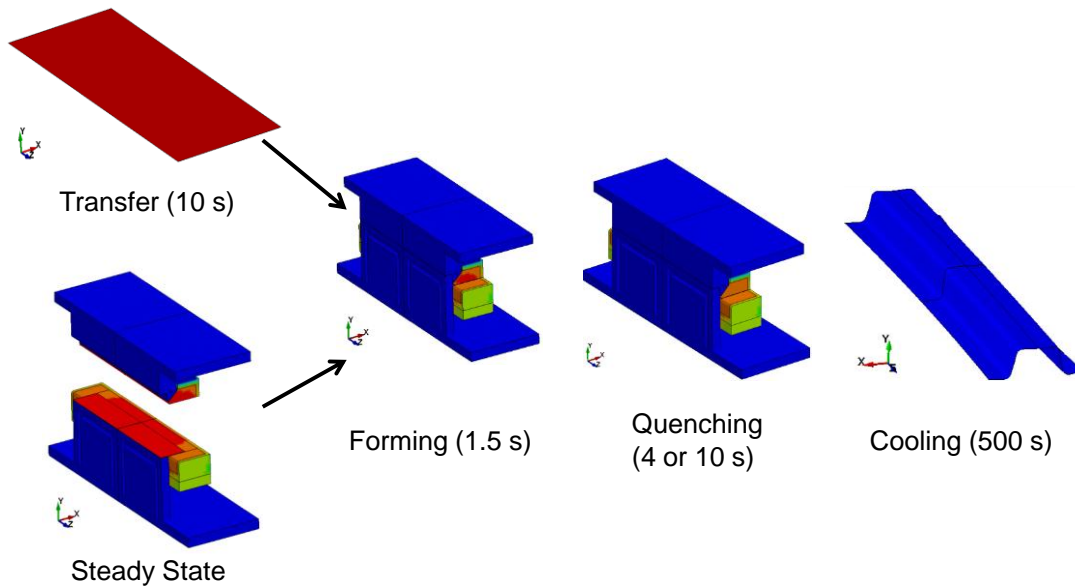
Figure 35: Forming simulation stages.

The first simulation predicts the steady state temperature distribution for the heated tooling configuration. This implicit thermal simulation is completed to determine the appropriate heat flux input required to create a steady state temperature of 400°C and 600°C at the forming surface. Two unique boundary fluxes, one for the cartridges located in the blank holder and one for the cartridges located in the binder are defined in the simulation. The required heat flux is determined by trial and error until the tooling surface reaches the desired forming and quenching temperatures. In the experiments, the cartridges located in the binder are controlled using two different PID control circuits as explained in Section 2.3.1. However, the numerical simulation assumes that the temperature distribution along the length of the binder is uniform and the applied heat flux will be identical.

The outer surfaces of the tooling have surface segments with applied boundary convection and radiation conditions to simulate the heat loss to the surrounding ambient environment, as explained in Section 3.1.2. The final temperature at the end of the steady state simulation is input to the forming simulation as an initial temperature condition of the tooling.

The second simulation predicts the cooling of the austenitized blank coming out from the furnace with an initial temperature of 930°C. The cooling in this simulation is calculated based on the amount of heat lost through convection and radiation to the ambient room temperature surrounding. This implicit simulation lasts for 10 seconds which includes 5 seconds for the blank to come out of the furnace and an additional 5 seconds of the blank resting in place on top of the ball roller transfer platform. The heat lost from the blank through contact with the transfer system and the ball roller platform in an experiment was considered negligible. The final temperature of the transfer simulation is input as the initial temperature for the blank in the forming simulation. The convection and radiation heat transfer parameters are listed in Table 8 and Table 9, respectively.

The third simulation is the forming of the blank within the tooling. The forming simulation uses the final temperature data from the steady state and transfer simulations as the initial temperature. The room temperature hot forming for the fully martensitic part will have an initial temperature of 25°C for all tooling parts. The thermal boundary conditions used in the forming simulation is identical to the ones used in the steady-state simulation. The forming utilizes an explicit dynamic simulation and lasts for a total of 1.5 seconds, starting with the hydraulic press at its fully opened position coming down to a fully closed position. This part of the simulation is driven using a load curve specifying the velocity vs. time of the upper die.

Figure 15 shows the displacement vs. time and force vs. time applied to the upper die. The binder is given a force vs. displacement curve to simulate the increasing upward force applied from the nitrogen gas

springs as the binder is displaced downward by the upper die. Figure 36 shows the force vs. displacement curve applied to the binder to mimic the nitrogen gas springs. The heat transfer between the blank and tooling forming surface will depend on the applied force from the nitrogen gas springs.
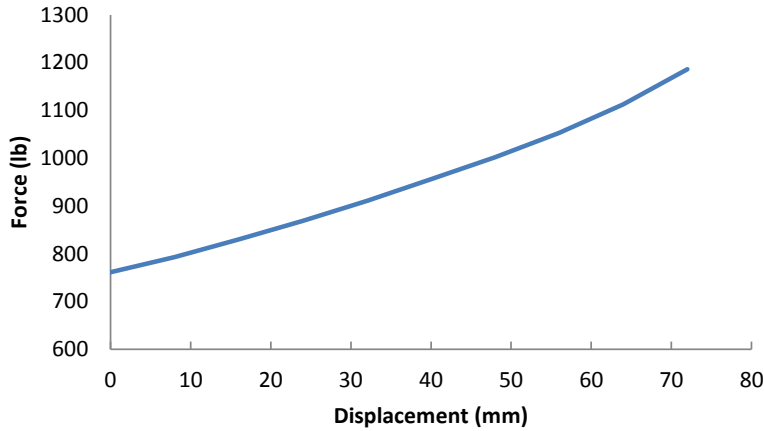
Figure 36: Total force vs. displacement from the nitrogen gas spring applied to the binder (at 1000 psi).

The fourth part of the forming simulation is a quenching simulation that lasts for either 4 or 10 seconds. In this simulation, the upper die is given the same amount of downward force as the 890 kN hydraulic press. The lower binder is given a constant upward force to simulate the force applied to the binder by the nitrogen gas spring cylinders at a displacement of 50 mm (see Figure 36). The thermal boundary conditions used in the forming simulation are identical to those used in the steady-state and forming simulations.

The fifth and last part of the forming simulation addresses air cooling of the hot formed blanks following removal of all tools. The cooling simulation considers boundary convection and radiation from the blank to its surrounding room temperature environment. The thermal boundary condition used in the air cooling of the blank simulation is the same as the ones used in the blank transfer simulation. The cooling simulation lasts for a total of 500 seconds and the final temperature of the side impact beam is approximately 5-10°C above room temperature. At the end of the quenching simulation, the final shape and mechanical properties of the blank elements are output to a dynain file which is used to initialize the 3-point bending simulations, described in Section 3.2.

The mass scaling technique is applied to the blank elements to reduce the computational time of a simulation with explicit dynamic time integration. The time step used in an explicit simulation has to be small enough to meet the Courant criterion [75]. The time step of the shell elements within the blank are

governed by the following equations, where L_s is the minimum characteristic element length in the model and c is the speed of sound in that material:

$$\Delta t_{max} = \frac{L_s}{c} \tag{11}$$

$$c = \sqrt{\frac{E}{\rho(1 - v^2)}} \tag{12}$$

Larger time steps will reduce the computational running time by reducing the number of computations. This is done by artificially increasing the density of the material, ρ, to increase the calculated speed of sound in the material. The order of magnitude that the density is increased must not be large enough to cause inertial effects within the simulation. During the air cooling simulations, the blank elements are sitting in air while losing thermal energy. Only small deformation due to thermal expansion happens at this stage. Larger mass scaling can be applied as inertia effects will be negligible. In the forming simulation, large deformation will take place and inertia effects due to mass scaling can be more significant. The amount of mass scaling used for each simulation stage is listed in Table 13. The larger mass scaling in the quenching and cooling simulations is acceptable since very little deformation occurs in reality during these processes.

Table 13: Mass scaling factors.

Forming Stage	Duration (seconds)	Mass Scaling Factor
Transfer	10	100
Forming	1.5	100
Quenching	4 or 10	100,000
Air Cooling	500	100,000,000

3.1.7 Free Cooling Validation

The blank goes through a cooling period of 10 seconds between exiting the furnace and being placed in the die for the beginning of the forming process. Some thermal energy will be lost through conduction to the ball roller platform used to transfer the blank from the furnace towards the forming die. The contact surfaces between the blank and the ball rollers are relatively small and the amount of heat transfer was assumed to be negligible for the simulation. The blank will be transferred in a horizontal position which creates two different convection heat transfer coefficients between the upper and lower surfaces and the air. The upper surface will have a higher heat transfer due to the rising of warm air and cold air replacing the air heated by the blank. The following equations give the formulae to calculate the convection heat

transfer coefficient of both upper and lower surfaces [76]. Nu_L is the Nusselt number and Ra_L is the Rayleigh number.

$$\text{Upper Surface } \overline{Nu_L} = 0.15 \, Ra_L^{\frac{1}{3}} \tag{13}$$

$$\text{Lower Surface } \overline{Nu_L} = 0.27 \, Ra_L^{\frac{1}{4}} \tag{14}$$

$$\text{Convection Coefficient } \bar{h} = \overline{Nu_L} \, \frac{k}{L} \tag{15}$$

The convection heat transfer coefficients are input as load curves in the form coefficient vs. current surface temperature. At higher temperature, radiation heat transfer is a major mode of heat transfer. This heat transfer calculation depends on the emissivity of the blank surface, which is difficult to predict due to the change caused by oxidation on the surface. A load curve for emissivity was estimated and plotted against surface temperature. The load curves for convection and radiation HTC vs. temperature are defined in Table 8 and Table 9 respectively.

In order to validate the free cooling predictions, an LS-DYNA cooling simulation with the same input keyword card as the transfer simulation, for which the blank has an initial temperature of 930°C and is cooled in room temperature air, was performed. The simulation considers a 500 second cooling period, which is longer than the actual transfer process, and the predictions were compared to corresponding blank cooling experiments. The experiments consisted of a blank instrumented with three thermocouples being austenized in a furnace at 930°C for 5 minutes. The blank is then moved to a platform elevated 100 mm above the ground to prevent direct heat loss to the ground through conduction. The blank is cooled in air in a horizontal position. The temperature recorded by the thermocouples is plotted against time in Figure 37 along with the predicted cooling rate from the model. In general, there is a good agreement between the predicted and the measured temperature histories lending confidence in the current transfer and cooling simulations.
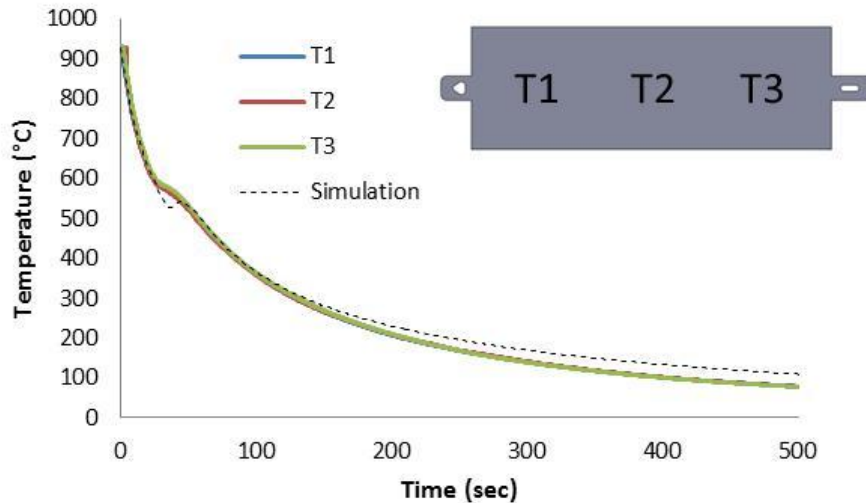
Figure 37: Blank free cooling measured vs. predicted temperature.

3.2   3-Point Bend Quasi-Static and Impact Simulations

This section presents the method of simulating the 3-point bend experiments done on the side impact beams formed using various forming parameters as well as different backing plate configurations. Both the quasi-static and impact experiments were simulated.

3.2.1   Mesh for Quasi-Static and Impact Simulation

The geometry set up for both the quasi-static and impact 3-point bend simulations is shown in Figure 38. Quarter-symmetry is used for both simulations to reduce the computational requirement. The impactor is shown in dark blue while the supports are represented using dark green. The backing plate is represented in light green.
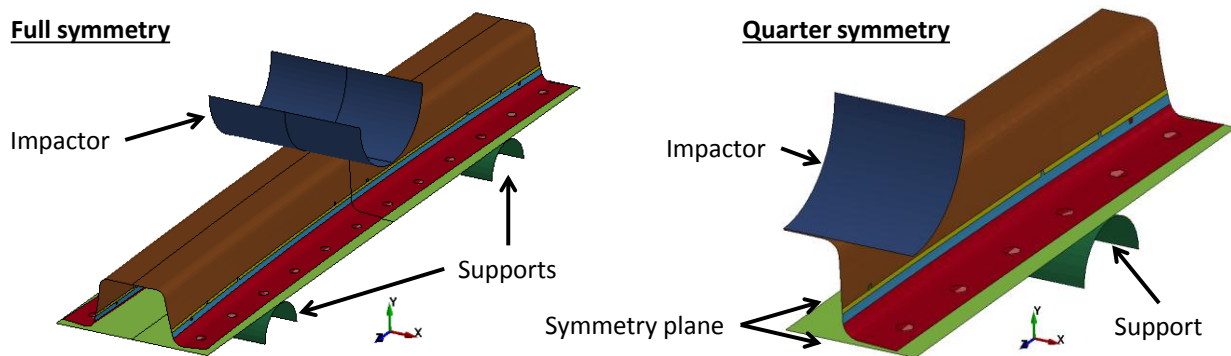
Figure 38: 3-point bend simulation set up.

The impactor and the support are meshed using rigid shell elements with a size of 5 mm by 5 mm. Both of the rigid shell parts have zero thickness assigned. The backing plate is meshed using deformable shell

elements with a size of 5 mm by 5 mm. All of the nodes for the backing plate are aligned on the horizontal XZ plane. The shape of the side impact beam is taken from the final shape of the formed blank at the end of the cooling simulation, as output in a dynain file. The original element size of 2.5 mm by 2.5 mm for the top hat structure is retained for the 3-point bend simulation. The element size of the backing plate is larger than the top hat structure, however, the amount of deformation expected to be seen by the backing plate is very low compared to the top hat structure. The simulation is done using quarter symmetry boundary conditions to reduce the computation time.

The placement of the backing plate shell elements is important to avoid any initial penetration between the backing plate elements and the shell elements in the flange region. When a formed side impact beam is placed on a flat level ground, the flange region of the side impact beam has some variation along the length in its elevation from the ground. The center of the side impact beam flange section tends to be higher than the end sections due to contraction experienced by the softer tailored flange during the microstructure transformation. The largest variation is seen with the tailored beams formed at the higher 600°C die temperature and the smallest variation is seen with beams formed using a fully cooled die. In the simulation, the backing plate is assumed to be in a flat initial position. The nearest element on the flange region is placed 1.2 mm above the backing plate elements to account for one-half of the thickness of the side impact beam and backing plate (both have a thickness of 1.2 mm). To simulate the 3-point bend experiments of the 1.8 mm side impact beams, the nearest node of the flange is located 1.5 mm above the backing plate elements. The impactor is located 0.6 mm above the nearest element along the center line while the support is placed 0.6 mm below the back plate.

3.2.2 Spot Weld Parameters

The backing plate is spot welded to the formed side impact beam. The dimensions and locations of the spot welds are described in Section 2.6. The spot welds are modeled in the simulation using the *MAT_SPOTWELD option within LS-DYNA [49]. This material model creates 2-noded beam elements with a given diameter and a length provided by the distance within the two nodes assigned for each spot welds. The given diameter for the spot welds in all of the 3-point bend simulations is 8 mm.

Both nodes for all spot welds are placed on the mid surface of the flange and backing plate elements. Placing the nodes on the flange elements was done by projecting a copy of the nodes placed on the backing plate along the Y-axis towards the surface of the flange region. Note that the length of each spot weld varies along the longitudinal axis due to deformation of the flange taking place during the cooling simulation due to the microstructure transformations. This is not a real representation of the actual spot welds as the flange and backing plate were clamped together during spot welding. The mechanical

properties assigned to the simulated spot welds are the same density, elastic modulus, and Poisson ratio as the parameters given to the side impact beam. The spot weld was not assigned a failure criterion since the experimental results did not show any post-experiment failure of any spot welds.

3.2.3   Contact Parameters for Quasi-Static and Impact Simulation

The contact parameters for the 3-point bend simulations use a coefficient of friction of 0.2 for both static and dynamic friction conditions. The contact condition is the same for both of the impactor and the support. Further assessment of the effect of the friction assumption on the predicted response is provided in Section 5.3.1.

3.2.4   Side Impact Beam and Backing Plate Material Model

The material model input data for the formed side impact beam for the 3-point bend simulation is created using a re-mapping program developed by Bardelcik et al. [26] called the "Tailored Crash Model (TCM)". The program is used to sort each element of the side impact beam taken from the end of the cooling simulation into multiple bins based on its predicted hardness. The tailored side impact beams formed with die temperature of 400°C and 600°C are re-mapped into a total of five different bins. Every bin has an equal range of hardness that each element can be sorted into. A different set of material properties are assigned to each bin based on the predicted hardness. As an example, a tailored flange part that has minimum and maximum hardness of 200 HV to 500 HV respectively will be sorted into five different bins, each with a hardness range of 60 HV. The TCM program outputs predicted effective stress vs. effective plastic strain at seven different strain rates based on the predicted hardness of each bin. The seven different strain rates range between 0.001 s^{-1} to 1000s^{-1}. This approach assigns a unique hardening response and strain-rate sensitive flow stress for each bin, with the assumption that all of the elements in a bin have the same hardness and mechanical properties. The hardness for each bin is calculated using a weighted average of all the elements in hardness range of that particular bin. Other mechanical properties such as density, elastic modulus, and Poisson's ratio have the same values from the forming simulation. In Figure 38, the elements of the side impact beam assigned to the different hardness bins are represented with a different colour. A re-mapped effective stress vs. effective plastic strain of a material model representing an element with a predicted hardness of 485 HV is shown in Figure 39 with its strain rate sensitivity.
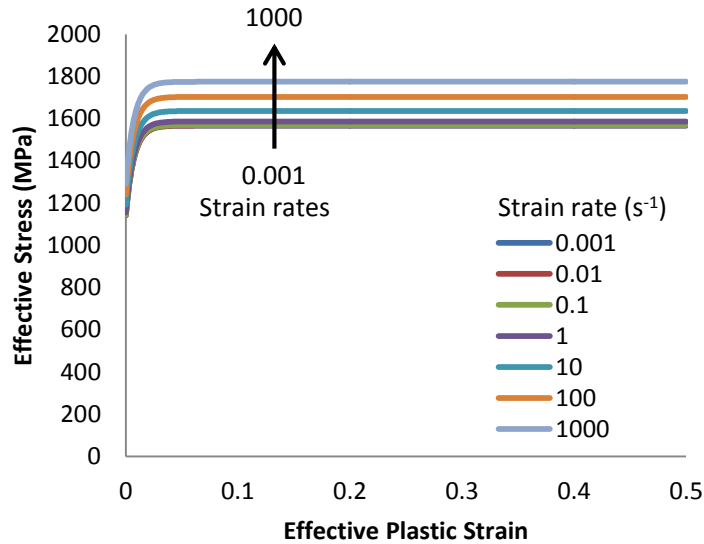
Figure 39: Re-mapped material properties of a hot stamped element with a predicted micro hardness of 485 HV.

The backing plate spot welded to the flange of the top hat structures is made from JAC590R that was produced and supplied by ArcelorMittal. Tensile test data for the backing plate material at a quasi-static rate is converted into an effective stress vs. effective plastic strain of the backing plate material and is input into the simulation for the backing plate material model. The load curve for the backing plate material model is shown in Figure 40.
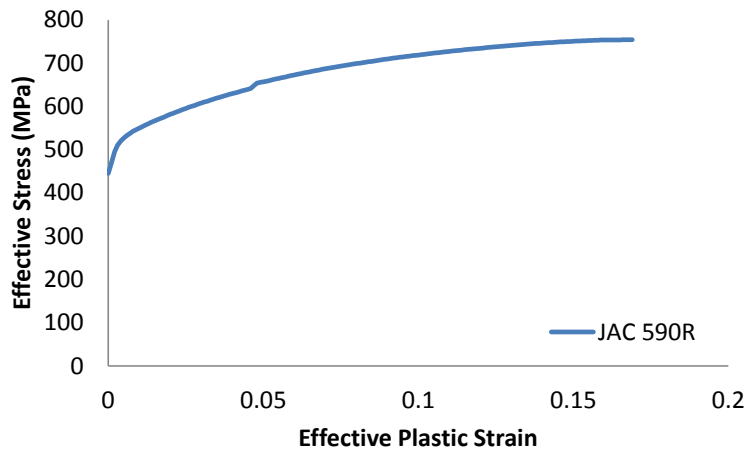
Figure 40: Material properties for the backing plate made from JAC590R.

3.2.5 3-Point Bend Simulation Boundary Condition

The quasi-static experiments were done with an impactor velocity of 0.76 mm per second and took just over two minutes for the impactor to travel 100 mm. To reduce the overall computation time to simulate the experiment, the actual impactor velocity modeled is 254 mm (10") per second. The quasi-static 3-

point bend simulation lasts for 0.5 seconds for the impactor to travel a total of 127 mm. The strain rates of the hot formed side impact beam material properties are multiplied with a factor of 333.3 to account for the time scaling of the simulation and avoid any artificial strain rate effect. No mass scaling was used in the quasi-static simulation.

The impact simulation does not have any time scaling or mass scaling applied as the experiment is completed within a very short period of time and mass scaling would introduce non-physical inertial effects. In the impact simulation, the impactor is stationary while the sled is represented by the moving support rods with an assigned mass of 980 kg to match the experimental conditions. Both the support rods and the side impact beam are assigned an initial velocity of 22 km/h (6.11 m/s) towards the impactor to simulate experimental velocity condition.

4 Experimental Results

This chapter presents the experimental results obtained from the forming and testing of a side impact beam formed with different die temperatures in the flange region and different quenching times. The results presented in this chapter include the Vickers micro hardness distribution within the side impact beam after forming. In addition, results from quasi-static and dynamic (impact) 3-point bend testing of tailored assemblies are presented. The experimental results are compared with the corresponding numerical predictions for validation purposes (in Chapter 5).

4.1　Measured Hardness Results

The hardness distributions for the side impact beam are presented in terms of the hardness as a function of distance from the edge of a flange to the center of the top section (Figure 41a). The hardness profile is assumed to be symmetrical with the longitudinal axis taken as the symmetry plane. Vickers micro hardness measurements were taken from three different parts for each forming condition, including three different forming die temperatures (RT, 400 and 600°C), two quenching periods (4 and 10 s), and two sheet metal thicknesses (1.2 and 1.8 mm). The first part for each condition was measured in detail with a distance interval of 2.5 mm (0.1") along the line shown in Figure 41a. For the other two parts for each condition, measurements were taken at the center of the flange, bottom corner, side wall, top corner, and top as shown in Figure 41b. Three through-thickness measurements were taken at each location and averaged. In the hardness plots presented in this section, the continuous line shows the average hardness along the distance of the first part. Additionally, error bars are included in the plot at the center of the five sections of top hat cross sections. The error bars show the minimum and maximum hardness value from nine measurements taken from three different parts.

(a) Direction of hardness measurement   (b) Measurement locations
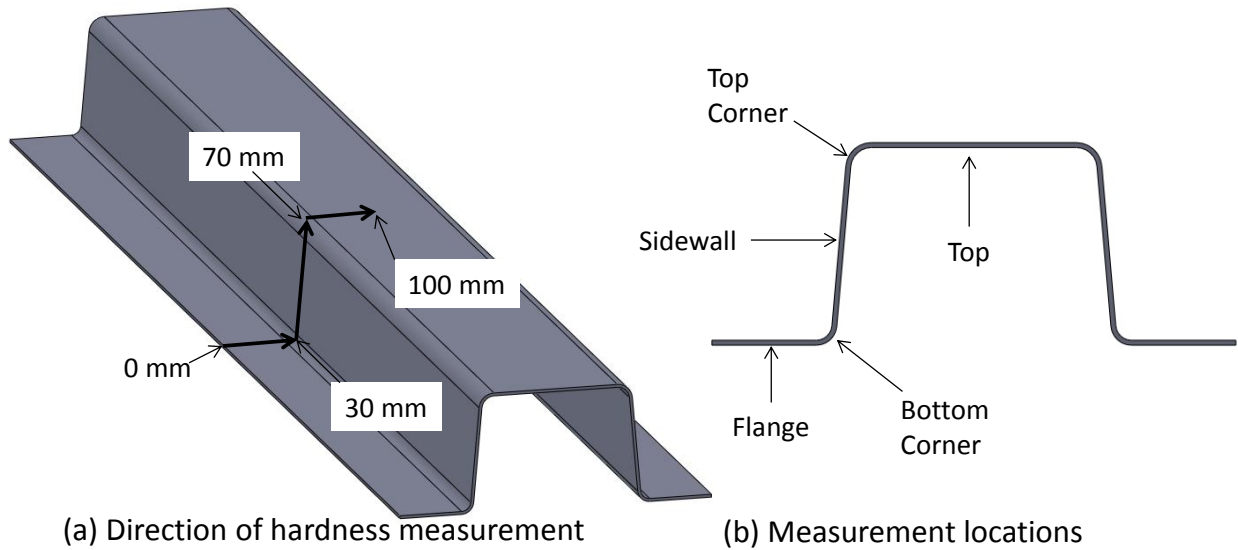
Figure 41: (a) Hardness measurements along the cross section and (b) measurement location.

4.1.1   Fully Quenched, 25°C Die, 1.2 mm Thickness

The measured hardness profile for the fully cooled side impact beam is plotted in Figure 42. The hardness values exceed 470 HV which indicates a fully martensitic condition across the entire section. Moreover, there is no significant difference in hardness between samples with 4 versus 10 s hold times. This is advantageous when a part is formed in an industrial setting, at least for this thickness level, since shorter cycle times can be achieved using a shorter in die quenching period without any compromise in the hardness distribution of the part.
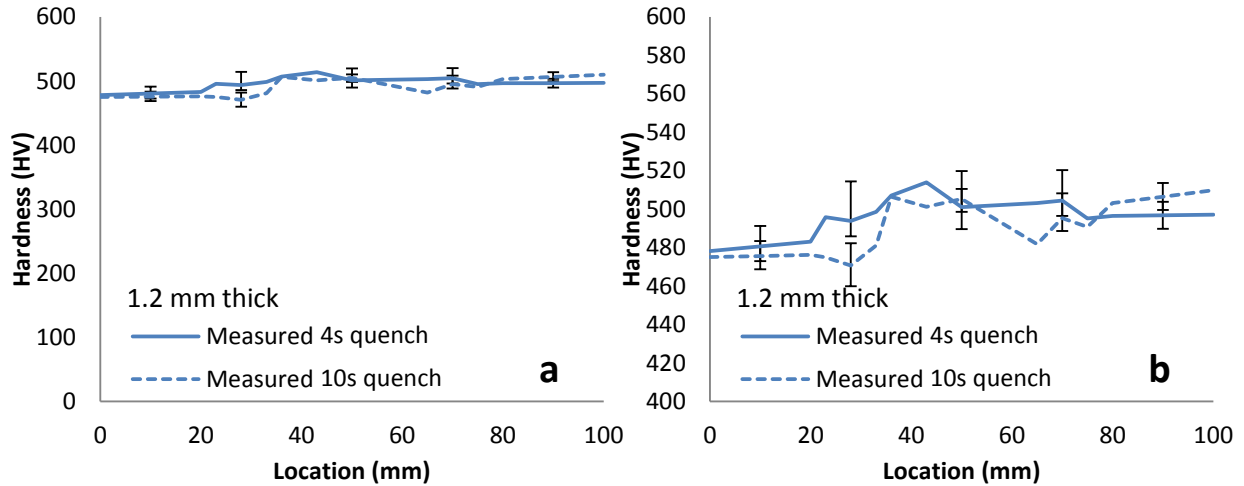
Figure 42: Micro hardness for 1.2mm side impact, 25°C die, with (a) a full and (b) a detailed hardness range. Location is plotted along the cross-section starting at the edge of the flange.

4.1.2   Tailored Flange, 400°C Die, 1.2 mm Thickness

The hardness across a top hat cross section formed with dies heated to 400°C in the flange region is shown in Figure 43. The tailored 1.2 mm side impact beam has a softer flange with a hardness of approximately 355 HV at the edge of the flange. This value is similar to the value of 330 HV reported by George [9] for a lab-scaled B-pillar formed using a die heated at 400°C. The top hat section shows that a fully martensitic region is achievable with an average hardness of 491 HV and 496 HV for the 4 s and 10 s quenching period, respectively. The hardness for the flange region was reduced to an average of 346 HV and 341 HV for the two quenching periods. The transition in hardness between the cooled and heated tooling region is quite gradual (as opposed to a sharp step function-like transition). The hardness increases almost linearly at the flange and plateaus to a fully hardened condition at 480 HV at a distance of approximately 40 mm away from the flange, roughly the beginning of the cooled sidewall section.
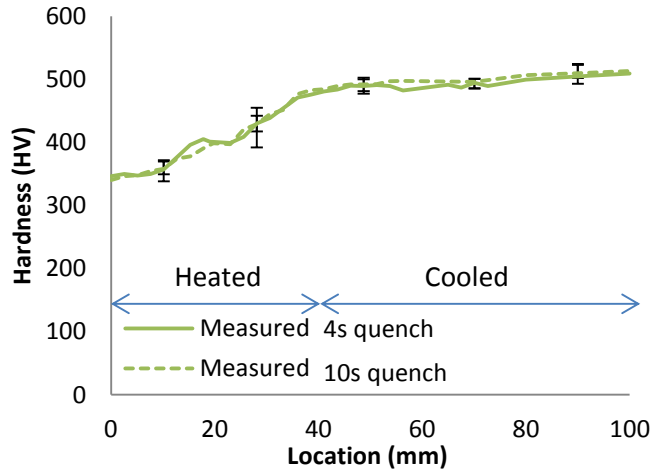
Figure 43: Micro hardness for 1.2 mm side impact, 400°C die. Location is plotted along the cross-section starting at the edge of the flange.

4.1.3   Tailored Flange, 600°C Die, 1.2 mm Thickness

The hardness of the top hat cross section formed with a die temperature heated at 600°C, shown in Figure 44, was lower in the flange area when compared to beams formed at 400°C. The flange has an average hardness of 210 HV which indicates there is some ferrite formation in the region [8,77]. The transition zone between the soft flange and hard top of the channel is better defined than that seen for the 400°C flange results (Figure 43) with clear hard and soft zone hardness plateaus and a steep transition near the location of the tooling temperature change (40 mm).
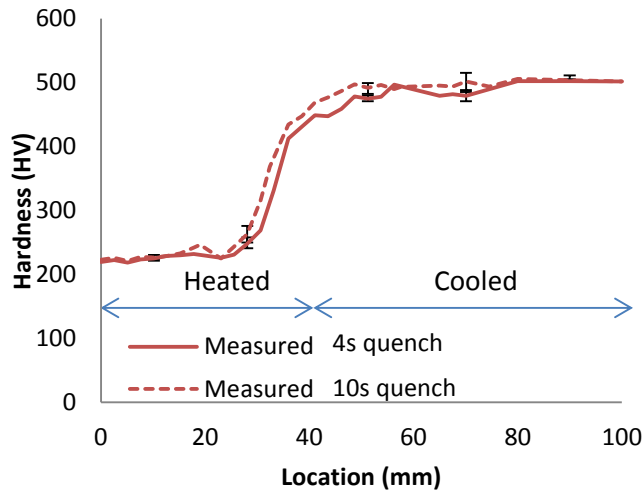
Figure 44: Micro hardness for 1.2 mm side impact, 600°C die. Location is plotted along the cross-section starting at the edge of the flange.

4.1.4 Fully quenched, 25°C Die, 1.8 mm thickness

Similar to their thinner counterparts, fully cooled side impact beams formed with 1.8 mm sheet show an overall fully martensitic part with an average hardness of 485 HV (Figure 45). There is no significant difference in hardness measured between the two different quenching periods. The average hardness of the fully hardened beams when formed with 4 and 10 s quenching periods were 480 HV and 487 HV respectively. The shorter quenching period is enough to produce fully hardened mechanical properties and is preferable for assembly line manufacturing purposes.
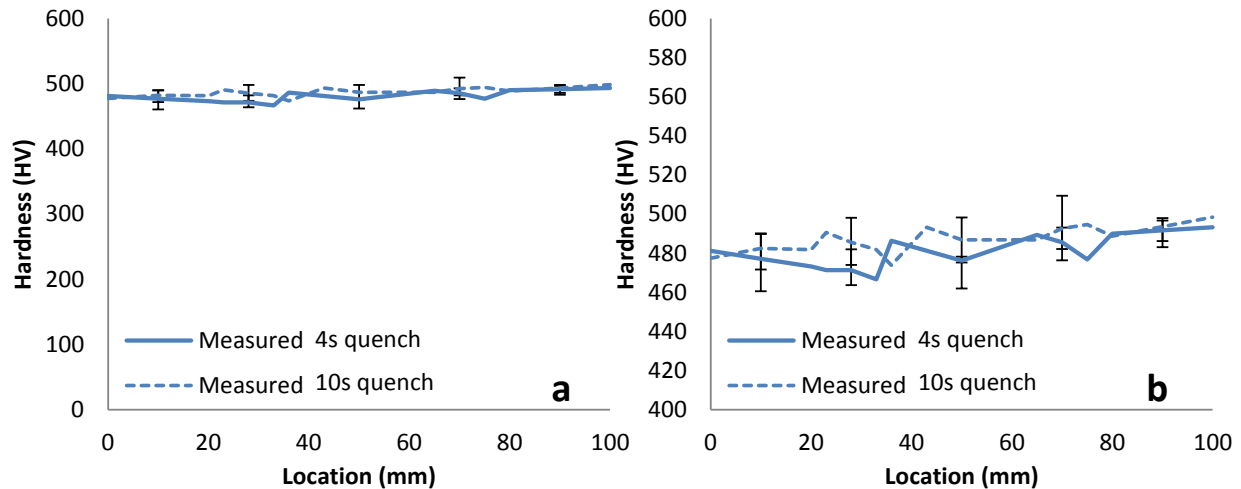

Figure 45: Micro hardness for 1.8 mm side impact, 25°C die, with (a) a full and (b) a detailed hardness range. Location is plotted along the cross-section starting at the edge of the flange.

4.1.5 Tailored Flange, 400°C Die, 1.8 mm Thickness

Measured micro hardness vs. location along the cross section of the 1.8 mm side impact beams formed with a 400°C heated flange region and both quenching periods is plotted in Figure 46. The thicker 1.8 mm sheet material shows a hardness value at approximately 280 HV in the flange area for both quenching periods. The transition zone begins at approximately 25 mm from the edge of the flange and reaches a fully hardened condition at 65 mm.

The hardness decreases just prior to 40 mm from the edge of the flange where the sidewall section begins. The hardness decrease can be observed for both quenching periods. This decrease in hardness in the sidewall region may be caused by the shift in CCT diagram (Figure 1) caused by plastic deformation in the sidewall during forming [78-80]. At measurement locations closer to the cooled die section, the increased cooling rate becomes more prominent once again to improve the hardness of the beam.
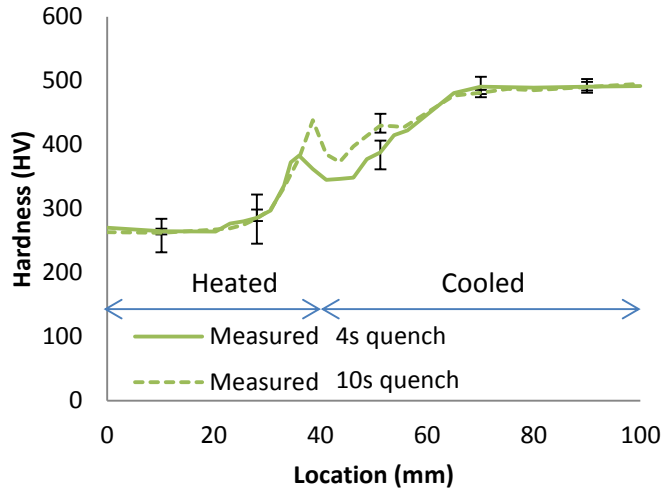
Figure 46: Micro hardness for 1.8 mm side impact, 400°C die. Location is plotted along the cross-section starting at the edge of the flange.

4.1.6   Tailored Flange, 600°C Die, 1.8 mm Thickness

Measured micro hardness vs. location along the cross section of 1.8 mm side impact beams formed with a 600°C heated flange region and both quenching periods is plotted in Figure 47. This tailored side impact beam formed produced the lowest hardness in the flange area for this study at an average hardness of 210 HV. There is a slight decrease in hardness for the side impact beam formed with a 4 seconds quench period similar to the ones formed with a die temperature of 400°C. The transition zone for parts formed with a 10 second quench exhibits a steeper increase in hardness over a smaller span of the bottom corner section. Both quenching periods produce a fully hardened condition with an average hardness of 485 HV at 65 mm from the edge of the flange. This distance is comparable to the tailored side impact beam formed with heated dies at 400°C.

65
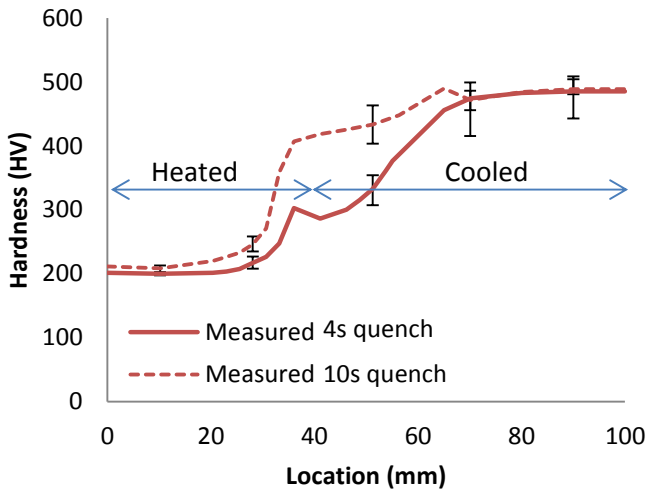
Figure 47: Micro hardness for 1.8 mm side impact, 600°C die. Location is plotted along the cross-section starting at the edge of the flange.

4.1.7   Overall Trends in Hardness Distributions

The overall trends from all of the die conditions and sheet thicknesses considered can be seen in Figure 48 and Figure 49 (error bars are omitted here for clarity). The drop in hardness in the flange region as the flange temperature is increased is clearly discernable. Flange hardness values for the 1.2 mm samples were 210 HV, 350 HV, and 490 HV for local die temperatures of 600°C, 400°C, and 25°C, respectively. For the thicker 1.8 mm material, the average hardness measured in the flange area is 200 HV, 270 HV, and 490 HV for local die temperatures of 600°C, 400°C, and 25°C, respectively. The hardness levels in the cooled sections of the tailored parts, away from the transition zone, all exhibit high hardness levels corresponding to a fully martensitic condition. The flanges formed at 400°C are likely to have a mixed martensite and bainite composition while the flanges formed at 600°C, with a hardness of less than 220 HV, are likely to have some ferrite in the final microstructure [8,26].
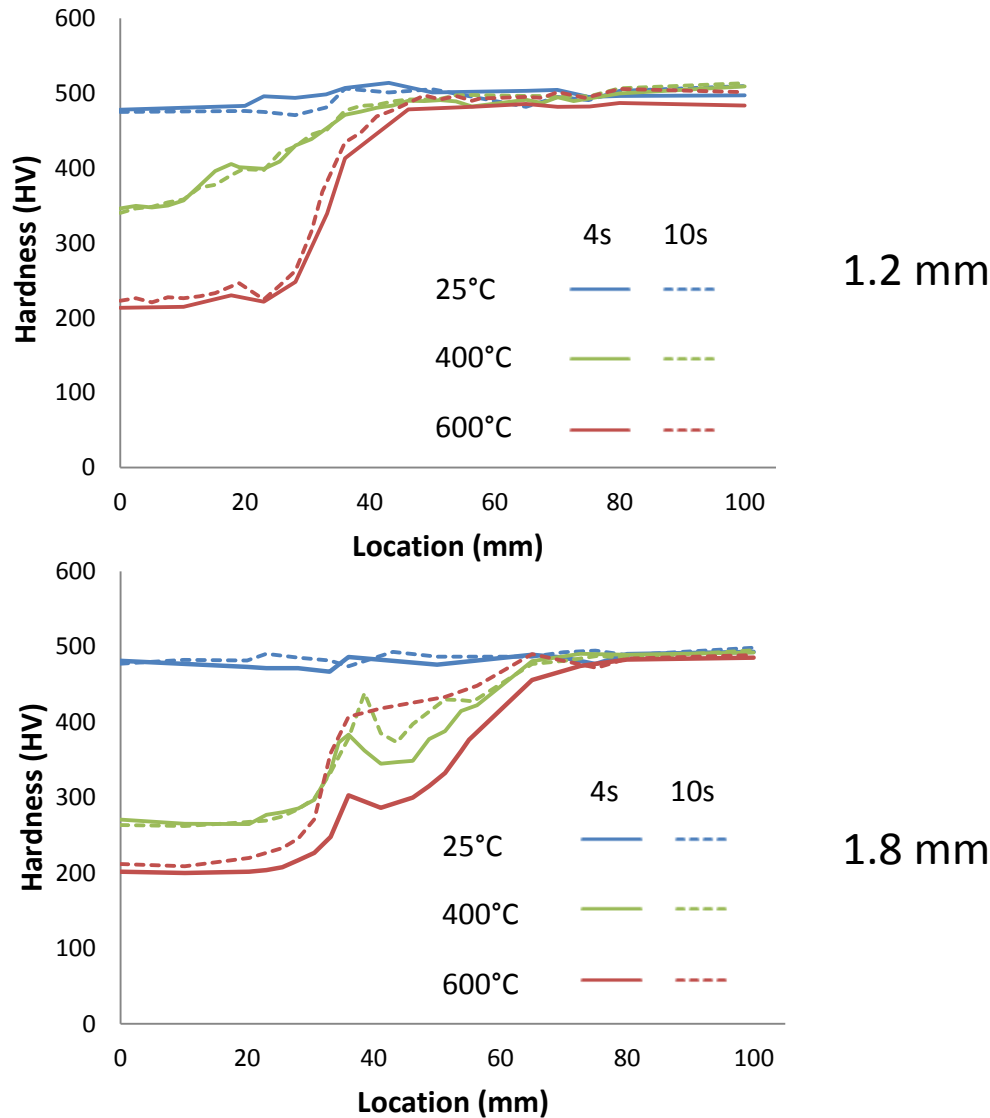
Figure 48: The effect of quenching period on measured micro hardness for all forming conditions.

Sheet thickness has a strong effect since the quench rates are lower for the thicker samples, which corresponds to lower hardness levels and wider transition zones for the 1.8 mm samples. The hardness in the flange area for both tailored beams formed at 400°C and 600°C are lower for the thicker 1.8 mm beams. When formed with a die temperature of 400°C, a flange hardness of 350 HV and 270 HV is achieved for the 1.2 mm and 1.8 mm blanks, respectively. At 600°C, the hardness achieved is 210 HV and 200 HV for blanks with 1.2 mm and 1.8 mm thickness, respectively. The transition zone between the soft flange and fully hardened top region is also affected by the different thickness; the 1.2 mm samples exhibit a narrower transition compared to the 1.8 mm samples.

The different quenching periods of 4 versus 10 s did not have a large effect on the hardness distribution of the 1.2 mm side impact beams. However, the longer quenching period for the thicker 1.8 mm beams did result in higher hardness levels in the transition zones of the tailored parts. This trend is attributed to lower cooling rates for the thicker samples (and higher die temperatures) and the need for longer quench times to complete the quenching operation.
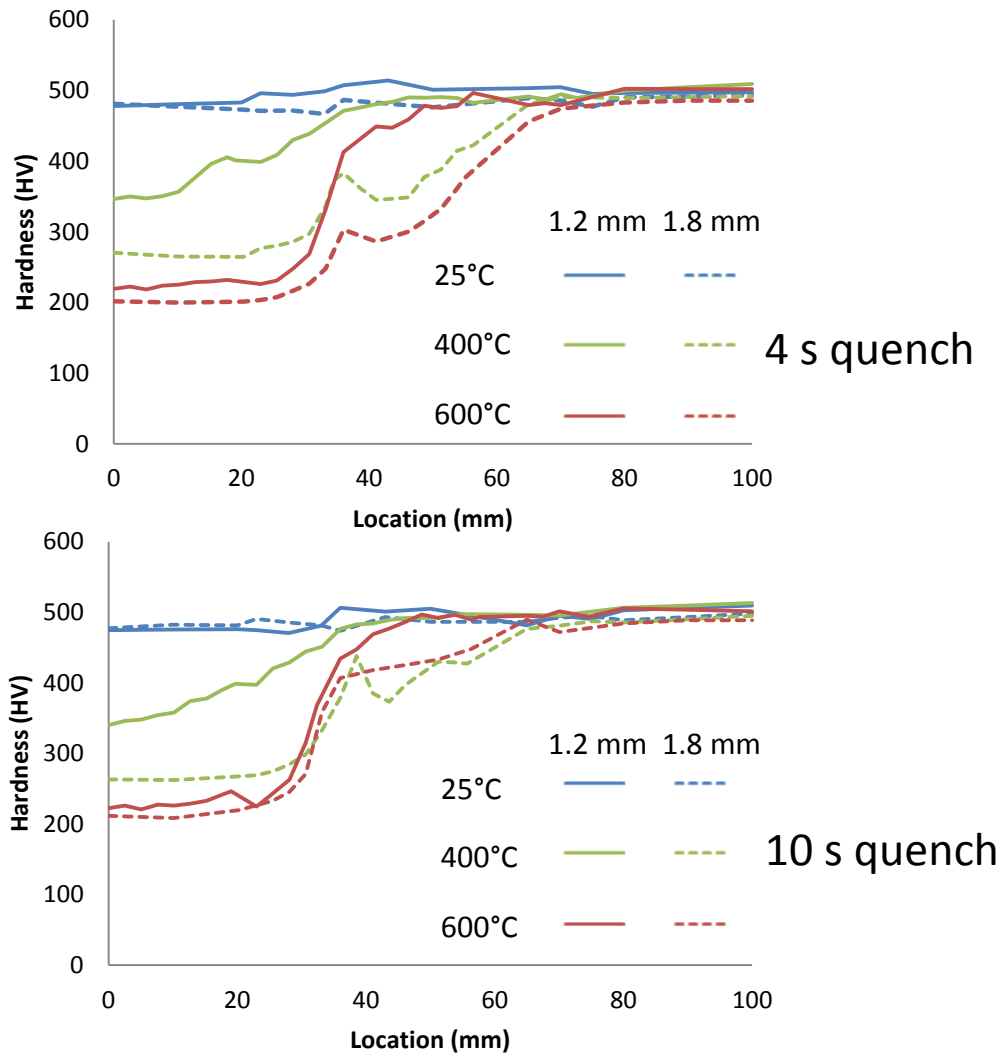
Figure 49: The effect of thickness on measured micro hardness for all forming conditions.

4.1.8 Variation in Hardness along Longitudinal Axis of the Beams

In order to assess potential variation in hardness along the length of the side impact beams, measurements were taken at three locations, as shown in Figure 50. Samples were taken from each formed part along three 20 mm wide strips located at one-quarter (Section A), one-half (Section B), and three-quarters (Section C) of the part length. Section A is closer to the furnace door while Section C is further into the

68

furnace during austenization prior to forming. To assess whether the hardness of the tailored hot stamped parts is uniform along the length, a 1.2 mm tailored part formed at 400°C with a 4 second quench period was selected for hardness measurements at Sections A, B and C. For each section, three hardness measurements were taken from each of the five areas of interest, also indicated in Figure 33. The results from the three sections are shown in Figure 50 and show that the variation in hardness along the longitudinal axis is relatively small, with the largest difference of 13 HV seen in the bottom corner area between Sections A and B.
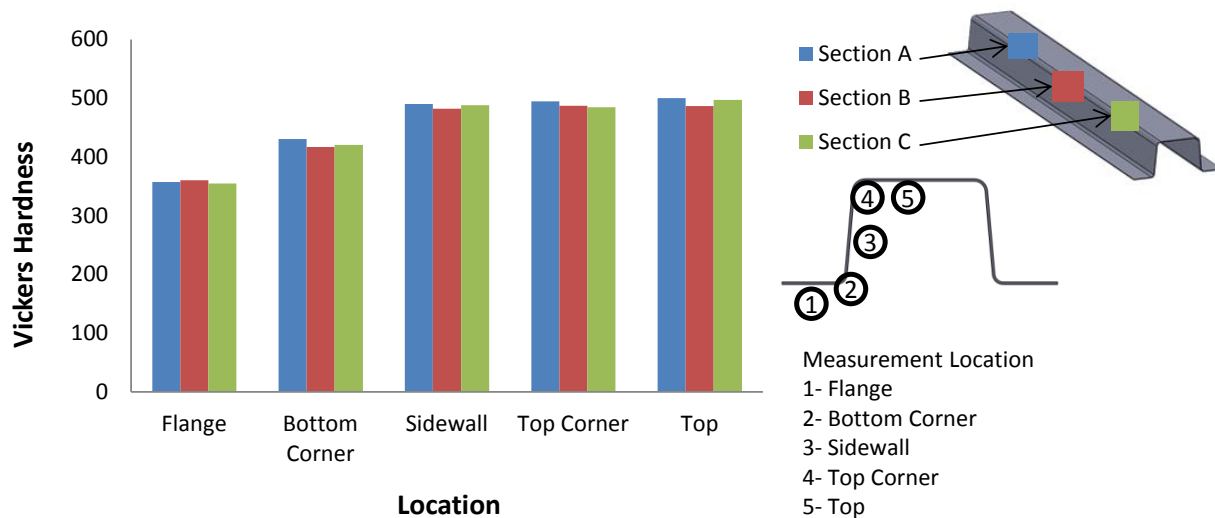
Figure 50: Hardness value along the length for 1.2 mm tailored side impact beam formed at 400°C.

4.2 Quasi-Static Three-Point Bend Experiment Results

The quasi-static experiment records the force vs. displacement response of a side impact beam under 3-point bend loading. The geometric parameters of the test were explained previously in section 2.7. In this study, the effects of forming die temperature, quenching period, backing plate configuration and material thickness on mechanical response are examined. A test matrix for the quasi-static experiment is shown in Table 4 of section 2.7.1.

The fully hardened side impact parts formed with a cooled die were taken as a baseline for comparison with the tailored side impact beams. A total of 12 parts were formed using the room temperature, cooled die configuration with six of the parts formed with a 4 second quenching period and the other six with a 10 second quenching period. Each of the six parts were split into two groups of three with one group welded using a full backing plate configuration and the other group welded using a split backing plate configuration (see section 2.6). Another 12 parts were made with a thickness of 1.8 mm and were divided into the same spot welding and quenching configurations. The same number of parts was created for each

69

tailored side impact beam configuration formed with heated die temperatures in the flange region of either 400°C or 600°C. Only the first 100 mm of the impactor displacement is shown in all force vs. displacement results reported this study. Beyond this displacement, the side impact beams collapse and no longer support significant load.

4.2.1   Fully Quenched, 25°C Die, 1.2 mm Thickness

Figure 51 shows the recorded force-displacement response from the three repetitions of quasi-static 3-point bend testing of the 1.2 mm side impact beams formed in a fully cooled die with a 4 second quench period and a full back plate. The measured response is very repeatable up to an impactor displacement of 35 mm. At this point, the beams exhibit one of two deformation modes, either a "collapsing mode" or a "wrapping mode".
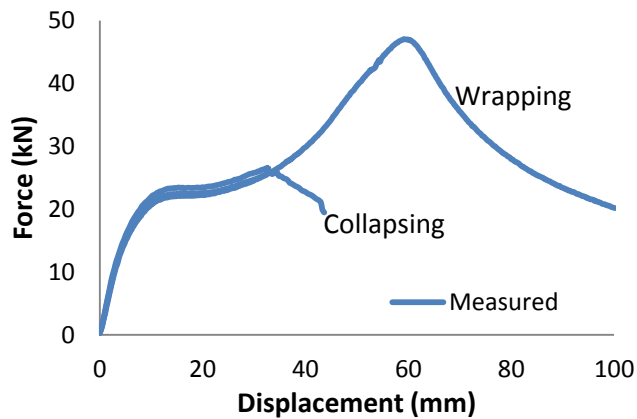
Figure 51: Force vs. displacement of beams formed with a room temperature die, a 4 second quenching period, and a full back plate configuration.

The "wrapping" deformation mode (Figure 52b) happens when there is sufficient friction between the top of the side impact beam and the surface of the impactor (indentor) such that the beam maintains contact and is wrapped around the indentor. The collapsing mode (Figure 52a) corresponds to a loss of contact with the bottom of the indentor such that the beam folds underneath the indentor, resulting in a much lower force-displacement response. The actual mode occurring in a particular test was somewhat random. In general, it is known that a high friction coefficient between the indentor and beam will tend to promote a wrapping mode. Although the indentor was hardened, it was noted that some scoring of the indentor was observed over the course of the experimental program. The indentor was polished manually between experiments with a 120 grit sand paper to remove any high spots created on the surface.
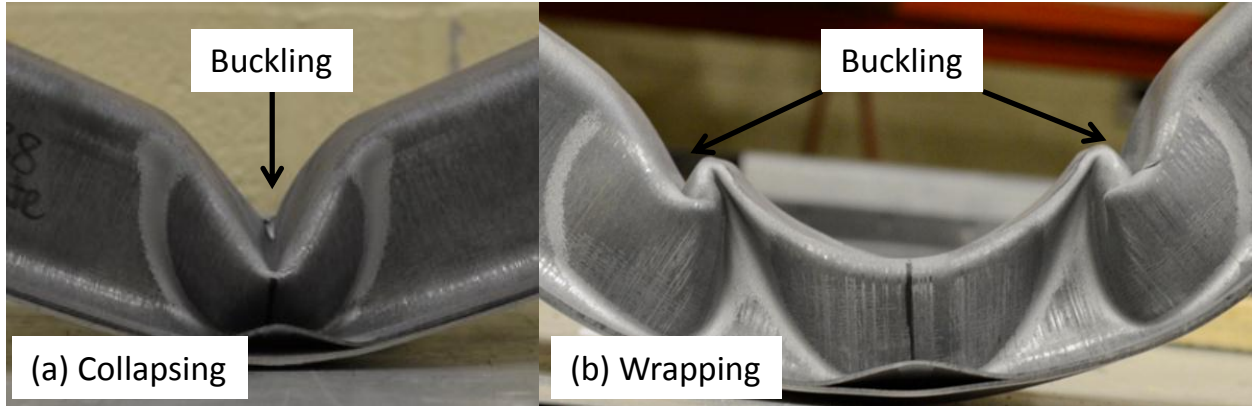
Figure 52: (a) 'Collapsing' and (b) 'Wrapping' side impact beams.

In Figure 51, the initial peak load happens at a displacement of approximately 10 mm when the side wall region of a side impact beam begins to collapse under the center of the indentor. The two deformation modes have different subsequent maximum load peaks. The collapsing mode has a lower second peak when contact is lost between the surface of the indentor and the specimen and the beam begins to collapse under the indentor. The wrapping mode exhibits an increasing load response to a higher maximum second peak at which point the top section of the top hat profile buckles in two locations around the impactor where the beam is not in contact with the impactor.

The deformation level of a side impact beam with a full back plate at an indentor displacement of 10 mm is shown in Figure 53. The level of the second peak depends on which deformation mode a side impact beam follows. In this study, the first peak will be the load response that will be used to compare the effects of all side impact forming parameters. This is chosen because the first peak load is less dependent of the friction condition between a side impact beam and an indentor.

10 mm indentor displacement
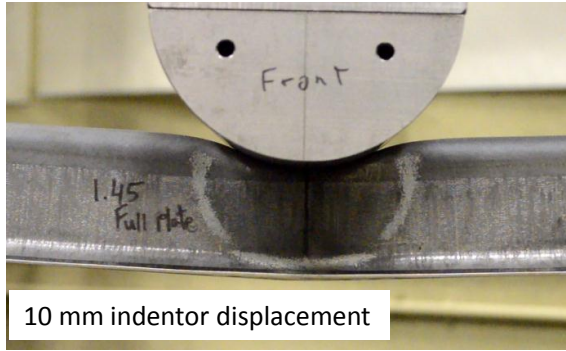
Figure 53: Quasi-static 3-point bend experiment of a 1.2 mm fully hardened side impact beam with a full back plate at an indentor displacement of 10 mm.

The force vs. displacement result for beam formed with a fully cooled die and a 4 second quenching period with a split back plate is shown in Figure 54. No spot weld failure was observed in this spot weld configuration. All three specimens tested with this configuration followed the collapsing deformation mode as the second peak load is reached at a displacement of just after 35 mm.
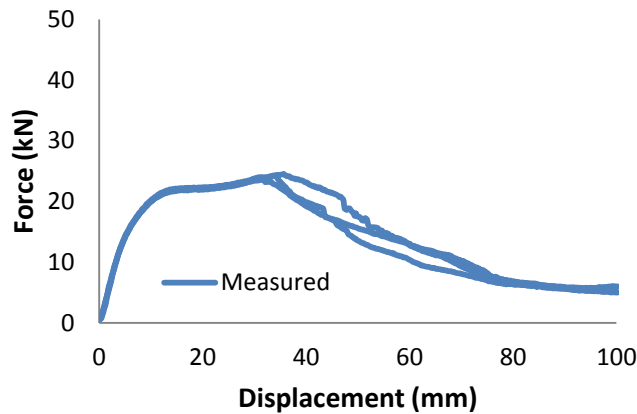
**Figure 54: Force vs. displacement results for the side impact beams formed with a room temperature die, a 4 second quenching period, and a split back plate configuration.**

The result for a 3-point bend experiment of side impact beams formed with a room temperature die, a 10 second quenching period, with full and split back plate is shown in Figure 55. The load response for full back plate side impact beams showed all three test repeats following the wrapping deformation mode. The split back plate configuration showed one specimen deformed in a wrapping mode and two in a collapsing mode. The observed deformation modes within the 1.2 mm side impact beam formed using a room temperature die shows that both wrapping and collapsing deformation modes can happen in both backing plate configurations.
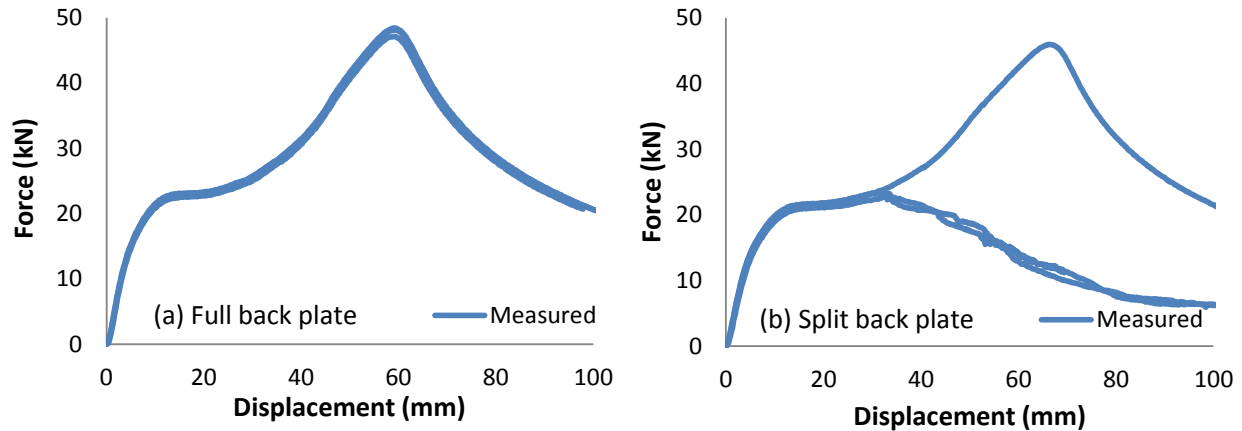
Figure 55: Force vs. displacement results for the (a) full back plate and (b) split back plate side impact beams formed with a room temperature die and a 10 second quenching period.

4.2.2   Tailored Flange, 400°C and 600°C Die, 1.2 mm Thickness

The force-displacement response for tailored side impact beams formed using heated dies with flange temperatures of 400°C and 600°C are shown in Figure 56 and Figure 57. The four second quench results are in Figure 56, while the 10 second quench results are in Figure 57. The figures compare the fully-quenched response against the tailored response from specimens formed using partially heated dies. The difference in the peak loads is not significant for the full backing plate configuration samples. However, differences are more evident when comparing the force displacement response between the different temperatures for the split back plate configuration. The difference in peak loads between the forming die temperatures for the full back plate beams is small because the softer flange in the center of a tailored beam is supported by the backing plate. In a split back plate configuration, the flange in the center of a beam has a tendency to open up during a test where it is not supported by a backing plate. More deformation is seen in the flange area, resulting in the larger difference in peak force. It is also noted that there were no spot weld failures in any of the side impact beams formed with a 4 second quenching period for both full and split backing plate configurations.
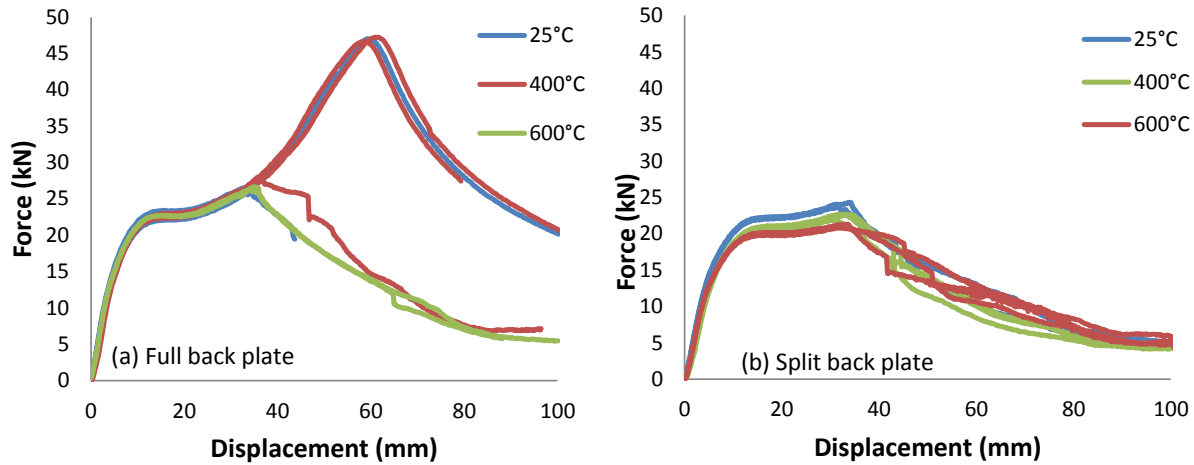
Figure 56: Force vs. displacement results for the tailored (a) full back plate and (b) split back plate 1.2 mm side impact beams formed with a 4 second quenching period.
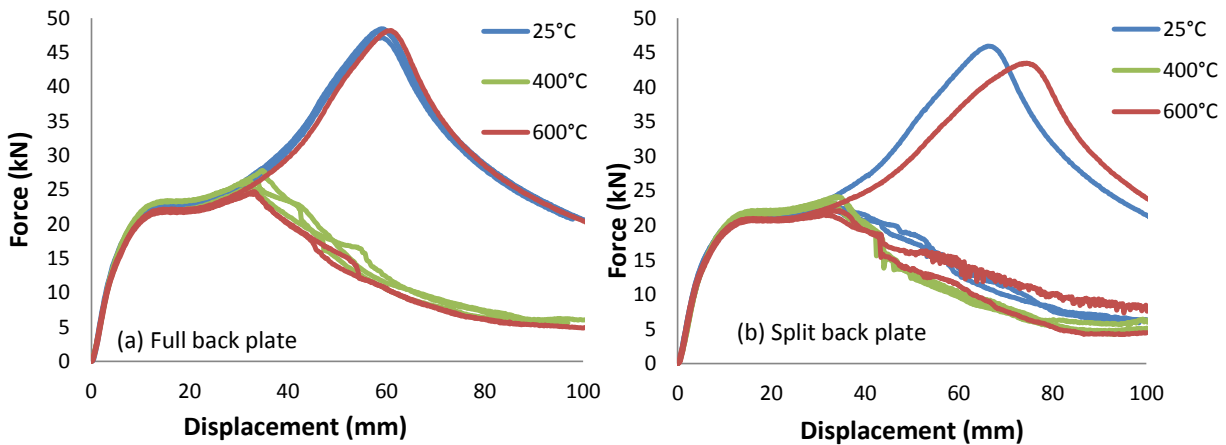
**Figure 57: Force vs. displacement results for the tailored (a) full back plate and (b) split back plate 1.2 mm side impact beams formed with a 10 second quenching period.**

The difference in peak force response for the tailored side impact beams with a full and a split back plate formed with a 10 second quenching period is almost the same as the specimens formed with a 4 second quench period. The difference in peak loads between the different forming temperatures is slightly more evident for the split back plate configuration.

4.2.3   Fully Quenched, 25°C Die, 1.8 mm Thickness

The side impact beams made from a thicker 1.8 mm sheet material were produced using all three die temperatures and both quenching periods. These parts were welded in the same way as the 1.2 mm side impact beams using the full and split back plate configurations. The backing plate material and thickness,

as well as the geometrical constraints were the same as those used in the 3-point bend testing of the 1.2 mm side impact beams.

The force-displacement response of the fully quenched 1.8 and 1.2 mm beams are compared in Figure 58. The general shape of the force-displacement response is generally the same; however, the 1.8 mm beams have a much higher peak force and none of the thicker 1.8 mm side impact beams exhibited the wrapping deformation mode. When the side wall collapses, the amount of load it can bear begins to decrease. The center of the beam loses contact with the indentor as the beam collapses and the contact friction between the beam and indentor does not increase the force response after the first peak load. The 1.8 mm side impact beams can carry approximately twice the load of a 1.2 mm side impact beams during the first 30 to 40 mm of indentor displacement. The peak load for a 1.8 mm and 1.2 mm full back plate is 42.9 kN and 23 kN, respectively. The noise in the response seen in Figure 58b after a displacement of 35 mm for the 1.8 mm split back plate specimens is caused by the frictional behaviour between the beams and indentor. Instead of continuous sliding between the beam and indentor as the beam collapses, the 1.8 mm beams exhibit a stick-slip response causing periodic rise and fall in load response.
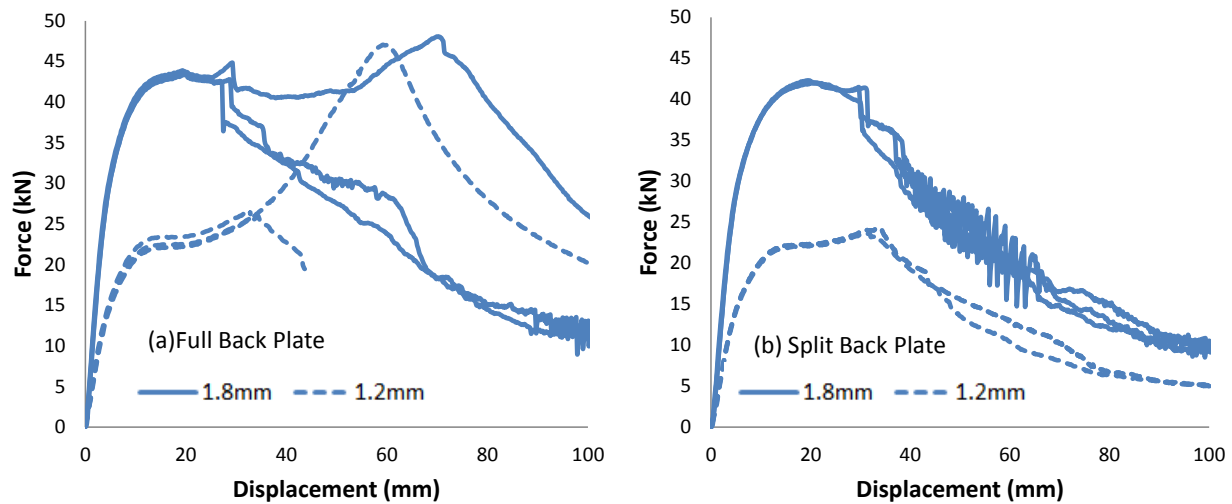
Figure 58: Force vs. displacement results for the (a) full back plate and (b) split back plate 1.8 mm side impact beams formed with a room temperature die compared to the 1.2 mm side impact beams.

4.2.4   Tailored Flange, 400°C and 600°C, 1.8 mm Thickness

The force-displacement response of the 1.8 mm tailored side impact beams with 4 and 10 second quenching periods are shown in Figure 59 and Figure 60, respectively. Also plotted are the results from the 1.8 mm fully quenched beams using a 25°C die temperature.

75
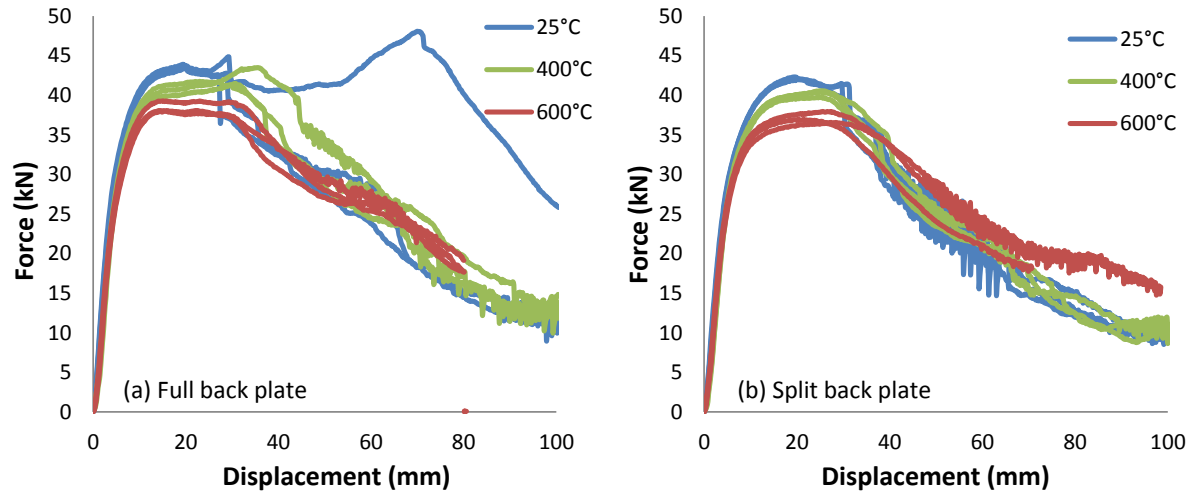
Figure 59: Force vs. displacement results for the tailored (a) full back plate and (b) split back plate 1.8 mm side impact beams formed with a 4 second quenching period.

The 1.8 mm side impact beams shows a more discernable difference in peak load as a function of flange die temperature. The drop in peak load is attributed to a reduction in hardness in the side wall region of the tailored 1.8 mm specimens, formed using a heated die, as shown in Figure 48. As the die temperature is increased, the sidewall collapses sooner during loading for the higher die temperature conditions. A smaller difference in force-displacement response due to tailoring was observed for the 1.2 mm specimens (Figure 56 and Figure 57) since the difference in hardness is mostly in the flange region and not in the sidewall (Figure 48).

The 4 second quenched specimens show a better correlation between the die temperatures and the peak loads for both the full and the split back plate configuration. Some noise in the response is seen in the split back plate configuration due to variations in the friction conditions between the specimen and indentor, as previously explained.
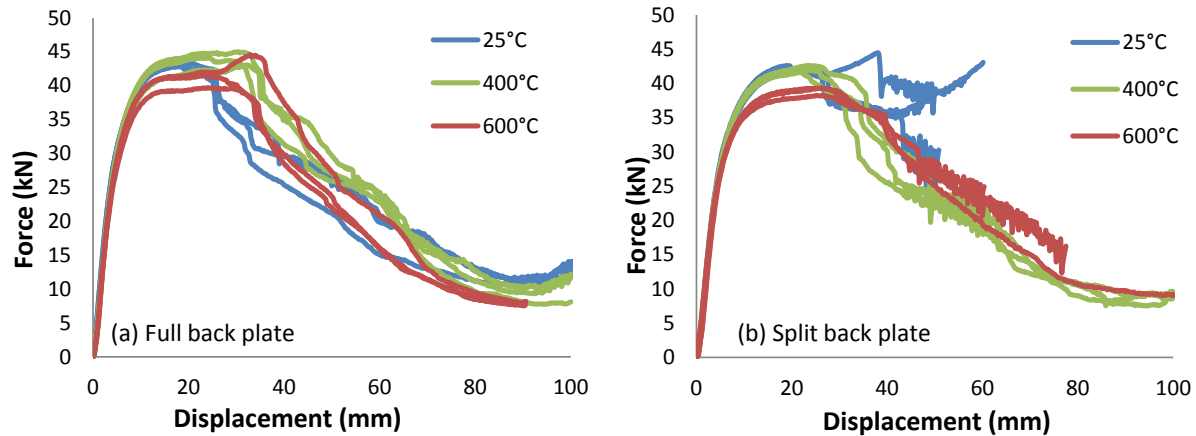
Figure 60: Force vs. displacement results for the tailored (a) full back plate and (b) split back plate 1.8 mm side impact beams formed with a 10 second quenching period.

4.3   Impact Experiment Results

Impact experiments were performed on the side impact beams using an impact sled at the University of Waterloo to examine dynamic effects on the force displacement response. The same geometry as used in the quasi-static 3-point bend test is used in the dynamic experiments, as described in section 2.7. Note that only 1.2 mm thick specimens in a fully quenched condition and those after tailored quenching with a 600°C flange die temperature with a 4 second quenching period were considered in the dynamic experiments. The 400°C tailoring condition was not considered since there was not a large difference between the mechanical response of the 600°C versus 400°C quasi-static experiments (Figure 56 and Figure 57). Both full and split backing plate configurations were studied in the dynamic experiments.

The force vs. displacement response from an impact test of a full back plate, tailored side impact beam formed with a heated die at 600°C and a 4 second quenching period is shown in Figure 61. This figure shows both the raw, unfiltered force-displacement data, as well as a filtered curve obtained using a low pass filter with a cutoff frequency of 60 Hz according to the SAE J211 standard. The energy absorption calculated from the unfiltered response of the impact test is plotted against the secondary Y-axis. Also plotted is one of the corresponding quasi-static responses of a collapsed 1.2 mm side impact beam from Section 4.2.1. Note that the filtered response only shows one load peak unlike in the unfiltered dynamic data and the quasi-static result. The initial contact between the beam and impactor is determined at the point where the unfiltered recorded force begins to increase from zero. The current displacement is calculated by integrating the recorded sled deceleration vs. time curve twice combined with the initial velocity of the sled recorded by a speed trap prior to impact and the initial displacement taken at the moment when force begins to increase. The point where the sled wall contacts the honeycomb is determined by a sudden increase of sled deceleration recorded in the unfiltered data. The sled contacts the

front of the honeycomb structure at an impactor displacement of approximately 100 mm. The peak load value of the filtered impact data is very similar to the quasi-static data, falling between the two peak loads from quasi-static test. For reference, all side impact beams tested under 3-point bend impact loading deformed in a collapse deformation mode as shown in Figure 62.
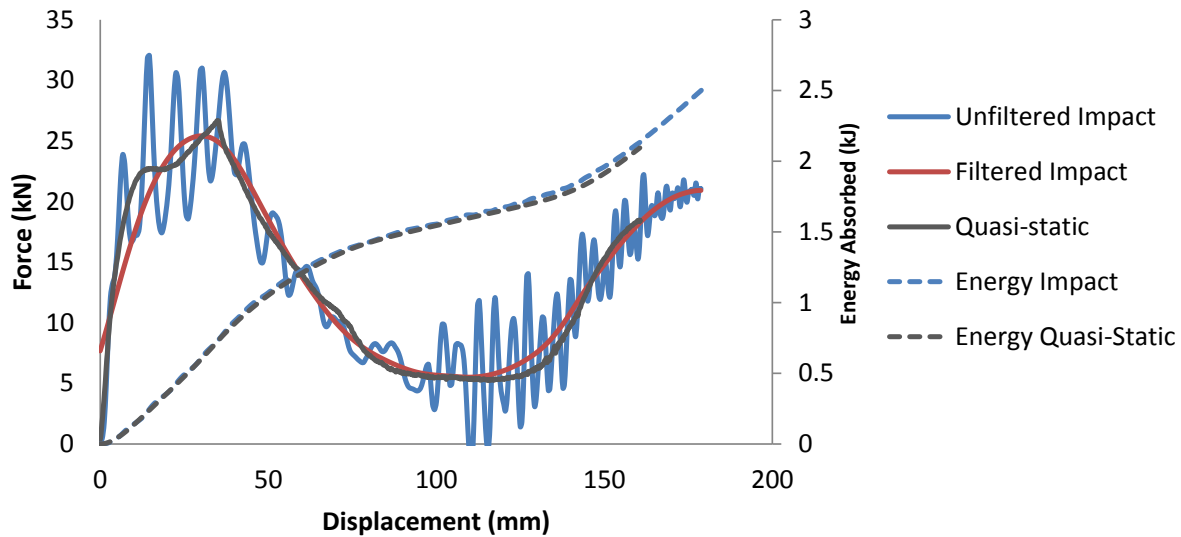
Figure 61: Filtered and unfiltered force vs. displacement results from the impact experiment compared with the quasi-static experiments of a tailored side impact beam with a full back plate and 4 second quenching period. Energy absorption vs. displacement of the unfiltered impact response is also shown.
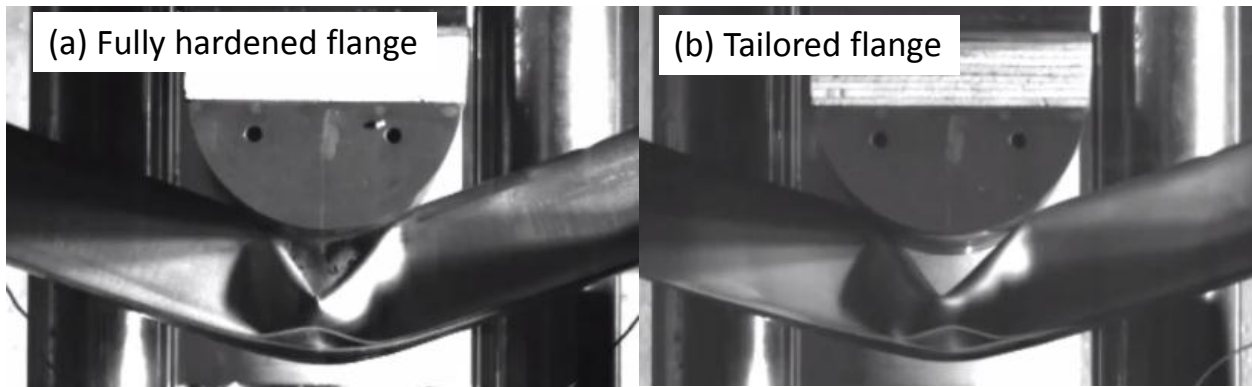
Figure 62: Images from high speed videos of impact tests of a 1.2 mm (a) fully hardened and (b) tailored flange side impact beams with a full back plate configuration.

The results for the remainder of the impact tests are presented only in terms of the filtered data. All results from the dynamic 3-point bend experiments are plotted in Figure 63. This figure has all 12 repeat experiments, shown in two plots to illustrate the repeatability of the test parameters. Figure 63a shows the force vs. displacement results for the full back plate specimens for both forming temperatures. Figure 63b shows the force vs. displacement results for the split back plate specimens. The data from the fully

hardened side impact beam is shown as a blue line while the tailored results are shown in red. The average peak load (filtered data) for impact tests on full back plate side impact beams are 26.8 kN and 25.6 kN for beams formed using a fully cooled die versus a tailored die, respectively. The average peak loads for beams with split backing plate are 23.3 kN and 22.2 kN for beams formed using a fully cooled die and a tailored die, respectively.
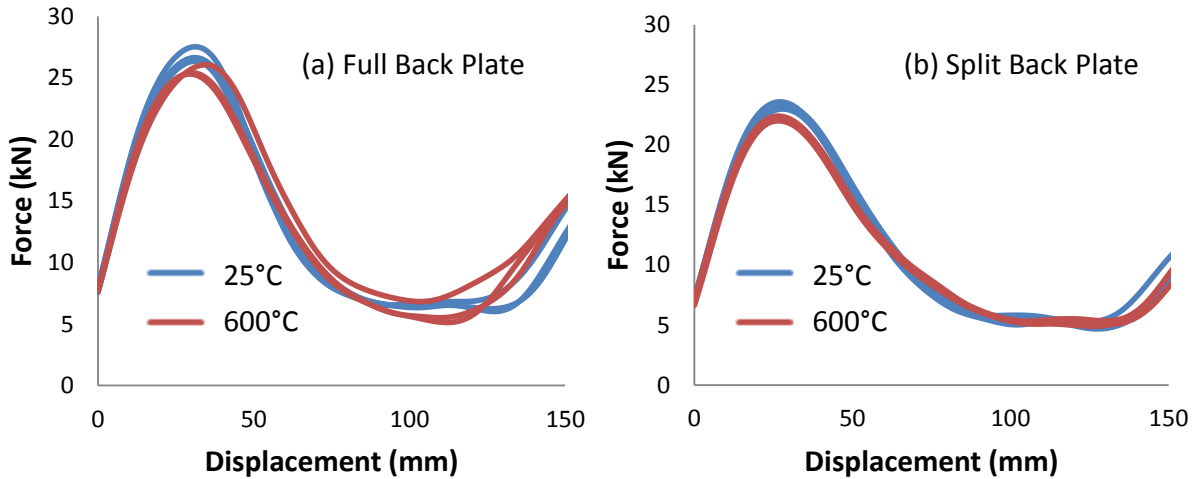
Figure 63: Filtered force vs. displacement results of (a) full back plate and (b) split back plate side impact beams formed with a 4 second quenching period.

Figure 64 shows the energy absorption vs. displacement for the different test conditions. The continuous lines are the energy absorbed for the full back plate beams, while the dotted lines are the results for beams with a split back plate configuration. The difference in energy absorbed between full and split back plate side impact beams mainly comes from the difference in maximum peak loads between an impactor displacement of approximately 35 to 50 mm. This difference is caused by the unsupported sidewall and flange that begins to open up due to the absence of support from a backing plate. The energy absorbed vs. displacement curve between the different back plate configurations remains mostly parallel after 50 mm of impactor displacement. The difference in energy absorbed between the fully hardened and tailored side impact beams is small. The total energy absorbed by the impacted beams at a displacement of 150 mm are calculated to be 2.39 kJ and 2.45 kJ for full back plate, fully hardened and tailored side impact beams, respectively. The split back plate side impact beams have calculated energy absorptions of 2.0 kJ and 1.97 kJ for fully hardened and tailored side impact beams respectively. The tailored side impact beams absorbed more energy than the fully hardened beams for impact tests with a full back plate configuration; however, the reverse effect was seen for beams spot welded with a split back plate configuration.
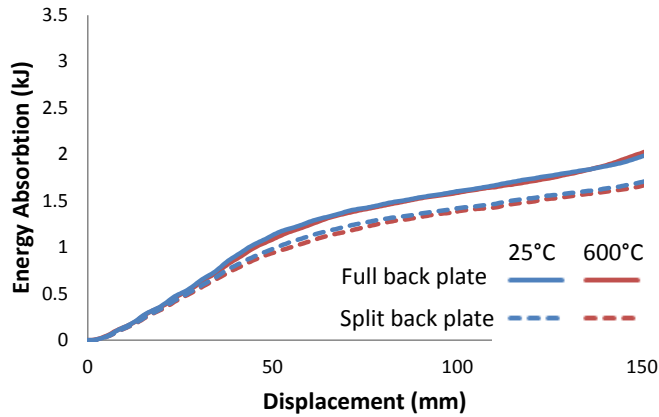
Figure 64: Energy absorbed vs. impactor displacement results from 3-point bend impact test of tailored side impact beams formed with a 4 second quenching period.

The deformation mode of both fully hardened and tailored beams are similar with the fully hardened beams having a slightly larger fracture in the center of its sidewall. Figure 65 shows the final shape of the fully hardened 1.2 mm side impact beams of both backing plate configurations after an impact test. No spot weld failure was observed in any of the impact tests conducted. The two secondary deformations on the top hat on both sides of the main impacted area are caused by the impactor having a large displacement before the sled wall comes into a complete stop. The side impact beams begin to wrap around the impactor as the beams go deeper in between the two base supports.
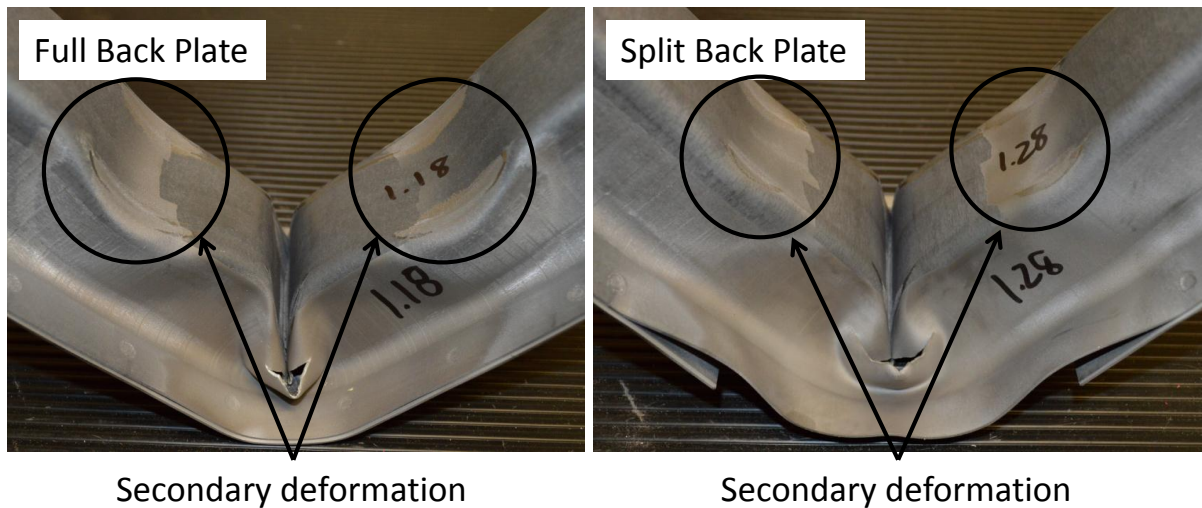
Figure 65: Side impact beams after an impact experiment of full back plate and split back plate fully hardened beams.

5 Numerical Simulation Results

This chapter presents the results from the numerical simulations done using the explicit dynamic finite element code LS-DYNA. The hardness predictions for all forming conditions are presented in contour plots. The predicted hardness vs. position from the edge of a flange towards the center of the beam across the top hat cross section are also plotted and compared to the measured results. The results serve to examine the effect that different die temperatures, quenching periods, and material thicknesses have on the predicted hardness.

The second part of this chapter presents the numerical simulation of the quasi-static and dynamic 3-point bend experiments. The results include the effect of die temperature, quenching period, material thickness, and backing plate configuration on the mechanical response for the quasi-static and dynamic 3-point bend tests.

5.1   Predicted Hardness Distributions

The predicted hardness distributions for side impact beams with a thickness of 1.2 mm and different forming die temperatures and quenching periods are shown in Figure 66. The contour plots are created using a range of 200 HV to 500 HV to show the full range of hardness achieved when a tailored side impact beam is formed using partially heated tool.
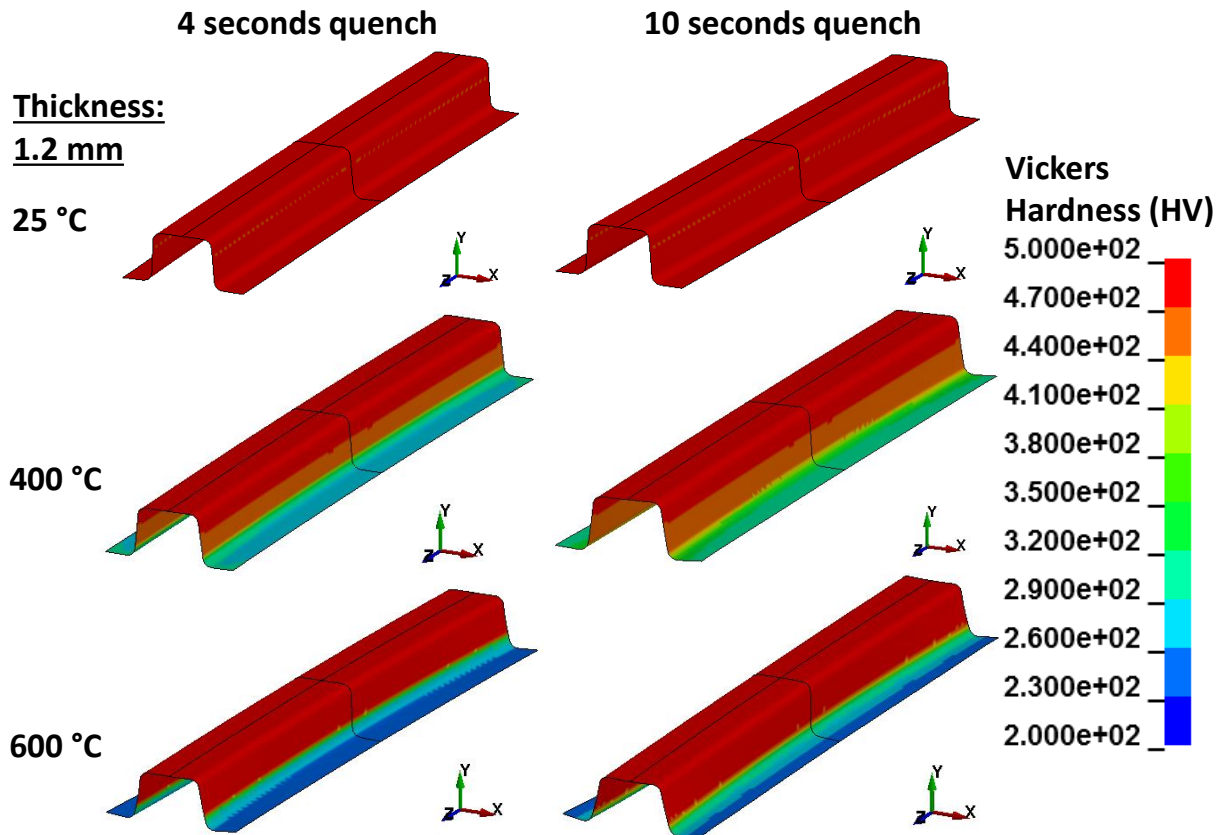
Figure 66: Contour plot of predicted Vickers hardness for 1.2 mm side impact beams.

A fully hardened side impact beam quenched in a room temperature die has a predicted uniform hardness of above 470 HV (Figure 66). An increase in local die temperature creates a softer flange region. The hardness of the side wall region is also affected by the heated die in the flange region even though the side wall is formed while contacting a cooled die. Tailored beams formed using a heated binder temperature of 400°C have a predicted hardness of the flange in the range 280 HV to 310 HV. The predicted hardness range is lower at 240 HV to 280 HV for tailored beams formed using a heated binder temperature of 600°C.

The predicted hardness for the 1.8 mm side impact beam is shown in Figure 67. The simulation results for this material thickness did not correspond to the measured results as well as the thinner material. The beams formed using a room temperature die did not show a fully hardened material condition throughout the part. It has a slightly lower hardness in the sidewall region and a very small soft sidewall region near the top corner. The overall hardness of a beam formed with a room temperature die, other than the softer elements shown in blue, is predicted to be 460 HV or higher. The small softer regions are predicted to have a hardness of 250 HV. The reason for this anomaly is unclear. To avoid propagating this error into

the 3-point bending simulations, the hardness for these elements was remapped into a higher hardness bin to match a fully hardened condition.
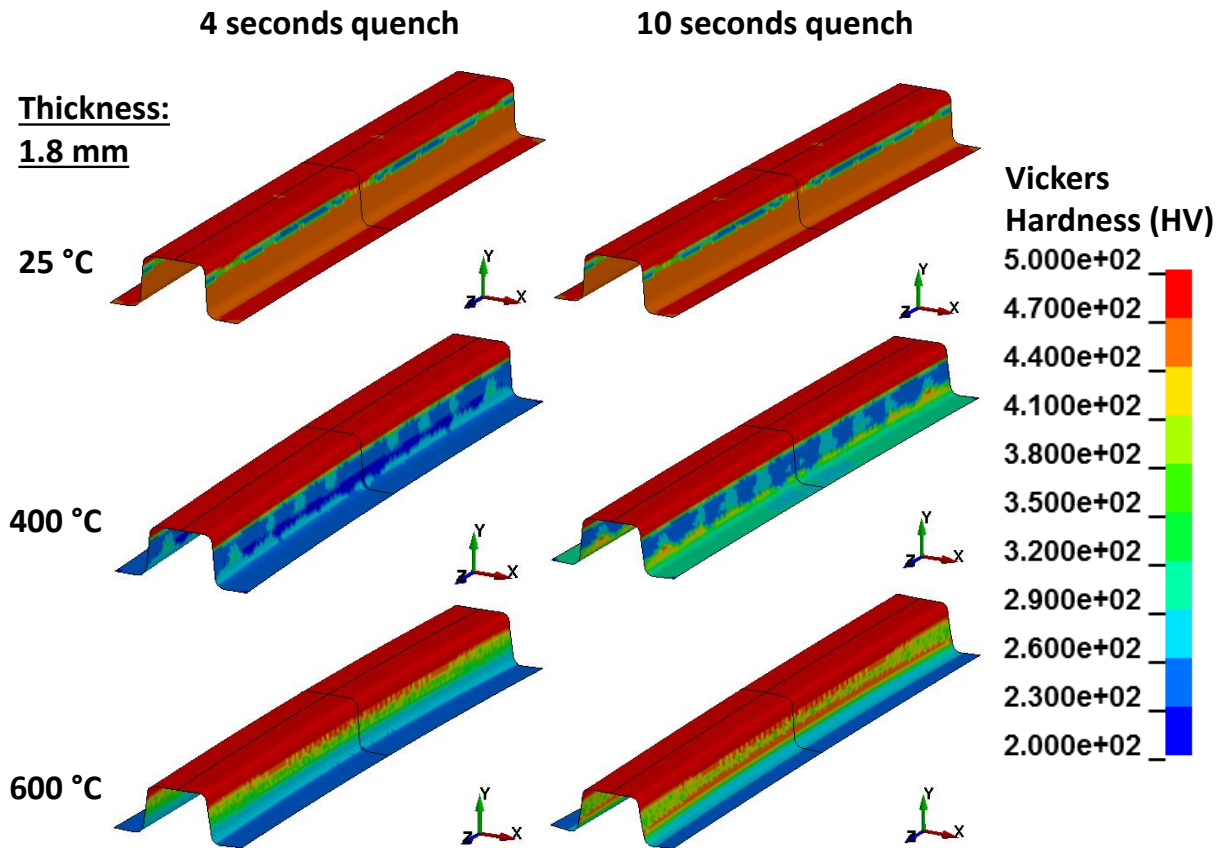
Figure 67: Contour plot of predicted Vickers hardness for 1.8 mm side impact beams.

The 1.8 mm tailored side impact beams have correct hardness predictions for the flat top and top corner where the elements are shown in red, indicating a predicted hardness above 470 HV. However, the forming simulation is under predicting hardness in the sidewall region. Both elevated temperature forming die simulations predict the transition zone between the soft flange and hard flat top to be very close to the top corner region. There is little difference in predicted hardness between the two quenching periods for a side impact beam formed at room temperature. However, the tailored beams formed with a tailored heated die show a difference in hardness prediction of the side wall region between the two quenching periods.

5.2   Predicted vs. Measured Vickers Micro Hardness

The measured hardness distributions presented in Figure 48, are compared here with the numerical simulation results. The measured hardness distributions are plotted in Figure 68 along with the corresponding numerical results in dotted lines.

1.2 mm Beam Hardness
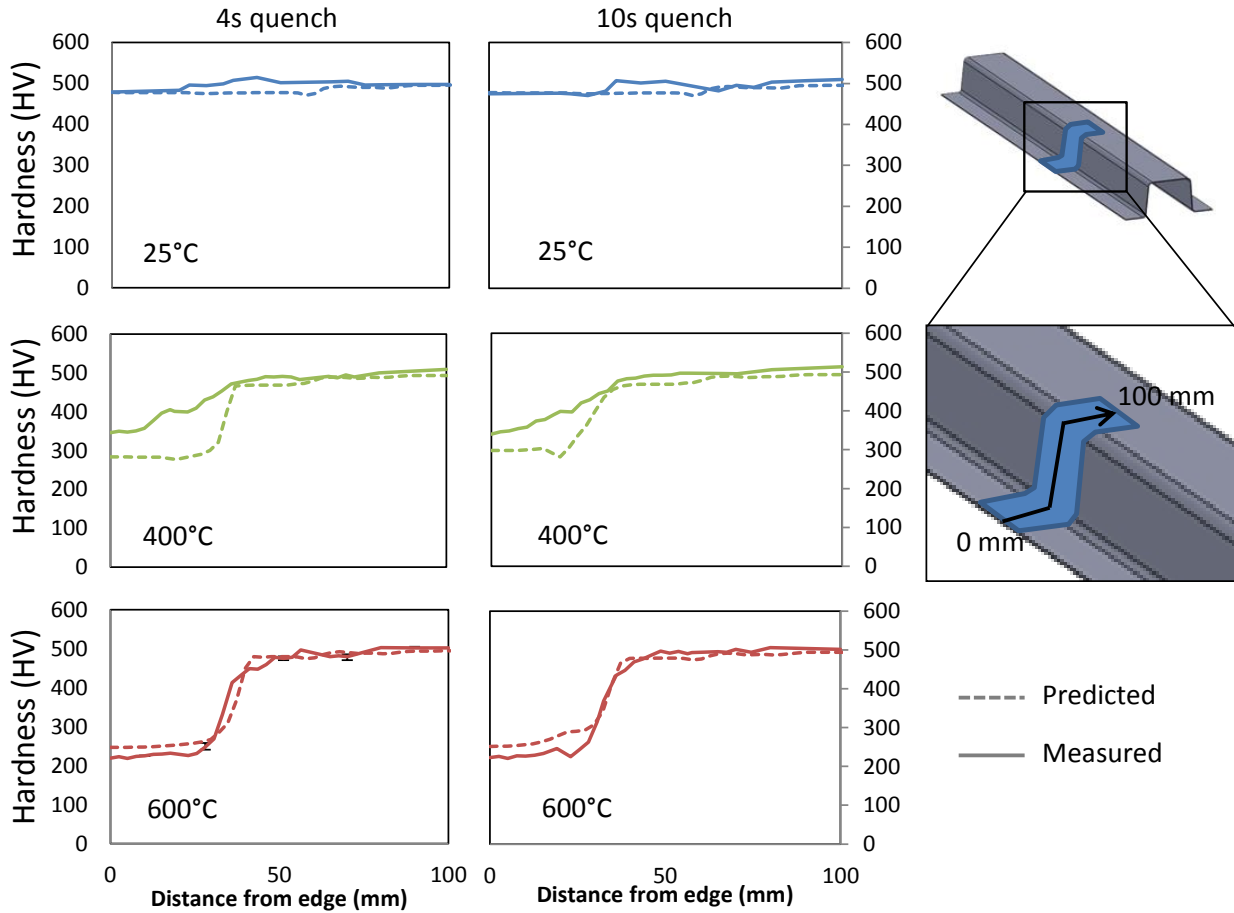
Figure 68: Predicted vs. measured hardness for 1.2 mm side impact beams along the mid-cross section of a top hat for both quenching periods.

The forming simulation for 1.2 mm side impact beams has a very good hardness prediction for side impact beams formed with a binder temperature of 25°C along the whole cross section. The hardness of the tailored beams formed at a temperature of 400°C is under-predicted in the flange and transition area. In the flange edge, the degree of hardness under prediction is 62.6 HV for the 1.2 mm tailored side impact beams formed using a heated binder at 400°C and 4 second quenching period. The predictions for the side impact beams formed at 600°C offer very good agreement with the measured hardness. The hardness of the flange region of specimens formed at 600°C is somewhat over-predicted by the simulation. This may be caused by formation of ferrite in the actual specimen that is not accounted for by the model.

The measured Vickers hardness data presented in Figure 68 shows a very small difference in hardness between the two quenching periods for 1.2 mm side impact beams, as also seen in the predictions. A small difference in predicted hardness for side impact beams formed with a 400°C heated die exists. The

transition zone between the soft flange and hard top hat is smaller and steeper in the forming simulation with a 4 second quenching period. The simulation with a longer quenching period predicts a larger transition zone with a more gradual increase in hardness.

The measured and predicted hardness for the 1.8 mm side impact beams are plotted in Figure 69. The hardness for beams formed at room temperature was predicted accurately except for a small region in the sidewall near the top corner for both quenching periods. The cause of this discrepancy is unknown. Predictions for tailored beams formed with a heated binder at 400°C show a good agreement with the measured hardness in the soft flange and hard top hat area. However, the sidewall region hardness is severely under-predicted for both quenching periods. The models of the tailored beams formed at 600°C exhibit slight over prediction in the flange area for both quenching periods. The largest hardness over prediction at the edge of the flange is 40 HV for a tailored 600°C beam with a 4 second quenching period. The under predicted hardness in the sidewall region of 1.8 mm beams formed at 400°C is caused by the over prediction of ferrite volume fraction by approximately 75%.

1.8 mm Beam Hardness
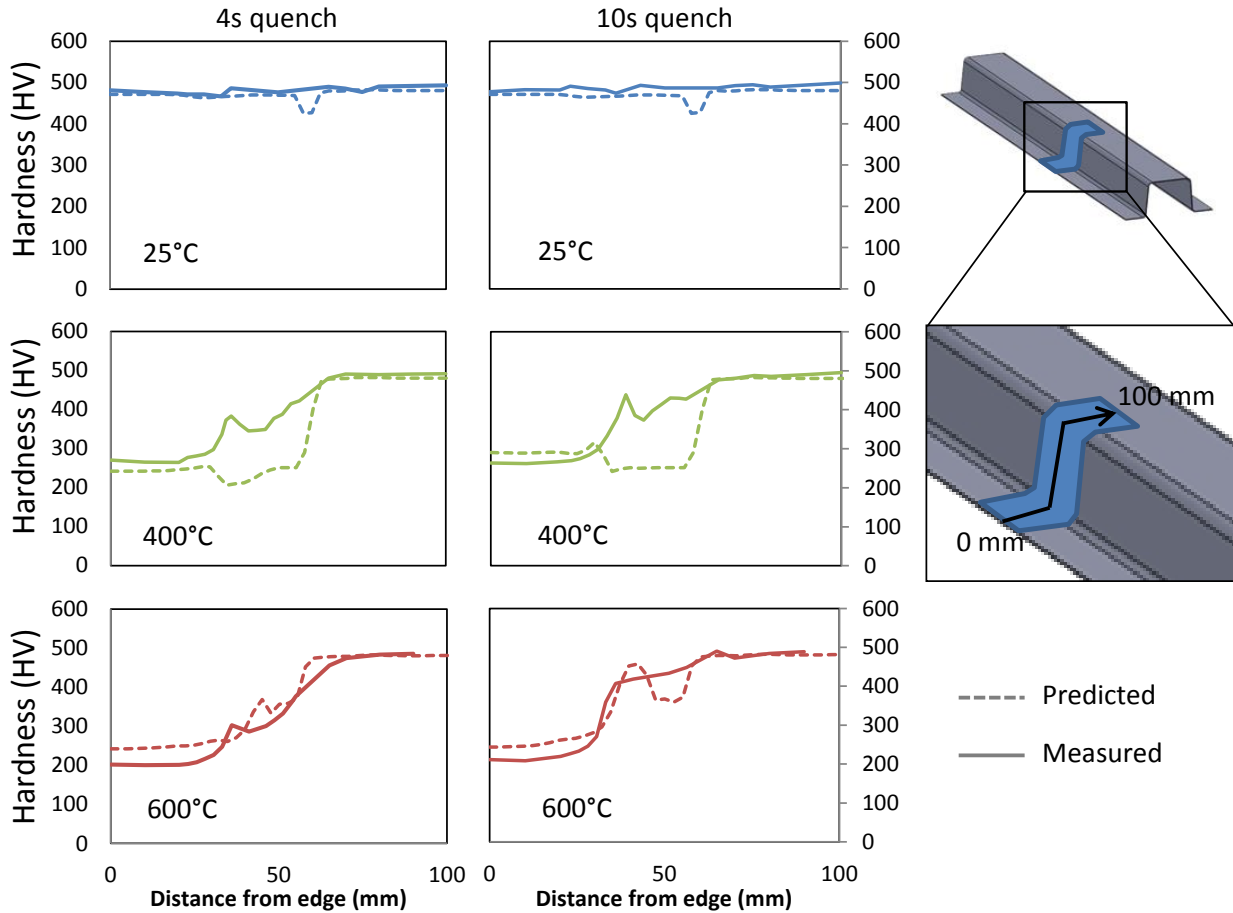
Figure 69: Predicted vs. measured hardness for 1.8 mm side impact beams along the mid-cross section of a top hat for both quenching periods.

5.3   3-Point Bend Simulations

The results from the quasi-static and dynamic 3-point bend simulations are discussed here. The predicted force vs. displacement response and the predicted deformation of the beams are shown and compared to the measured results.

5.3.1   Effect of Friction on Quasi-Static Force Response and Deformation Mode

Prior to comparing the predictions to experiment, the effect of friction between the indentor and beam surface is examined in a parametric fashion. Figure 70 shows the predicted force-displacement response for a fully hardened 1.2 mm side impact beam formed with a 4 second quenching period and spot welded with a full back plate. The curves plotted are predictions for friction levels between 0.2 and 0.3. The level of friction between the indentor and the 3-point bend specimen changes the deformation mode between

the wrapping and collapsing modes identified in Section 4.2, with dramatic changes in the resulting force versus displacement response.
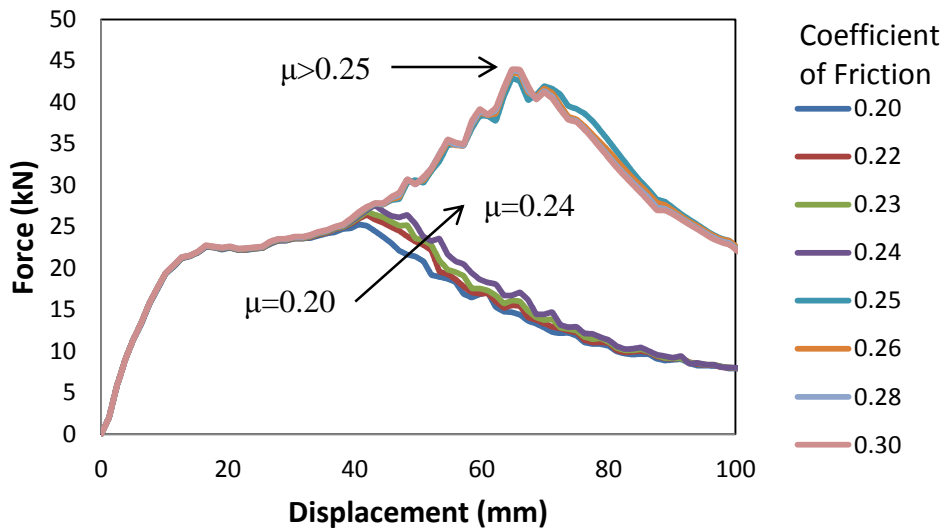
Figure 70: Predicted force-displacement response for 3-point bend simulation considering varying coefficient of friction between side impact beam and indentor.

In Figure 70, the response for the first 40 mm of indentor displacement is equal across all friction conditions. At roughly 40 mm displacement, the response diverges depending upon the friction coefficient. For friction coefficients of 0.24 or less, a collapse mode ensues (Figure 71) and the second peak force increases with coefficient of friction and corresponds to the point at which the beam begins to slide under the impactor and starts to collapse. Figure 70 further illustrates this behaviour, showing the deformed meshes for the two friction coefficients, 0.24 versus 0.25, and the resulting transition between the wrap and collapse deformation modes.
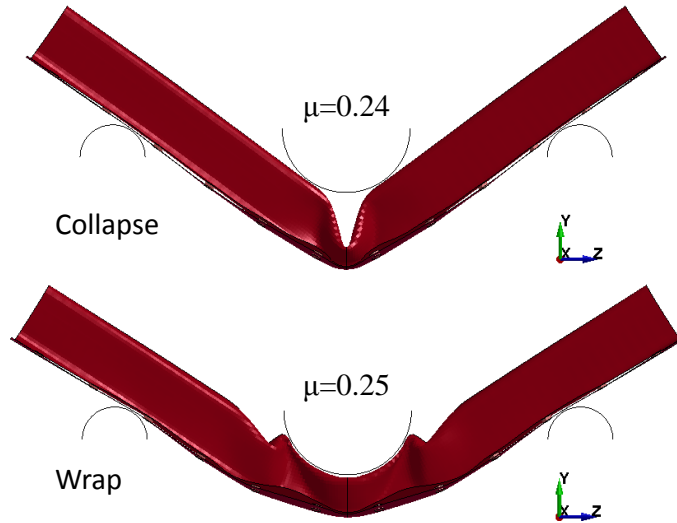
Figure 71: Predicted deformation mode based on contact friction between beam and indentor.

Note that a friction coefficient of 0.2 was adopted for the balance of the simulations presented herein which resulted in a folding deformation mode in all of the models. This coefficient was chosen based on the results of twist compression testing performed by Bardelcik et al. [81] that yielded a measured friction coefficient between 4130 steel and a fully martensitic Usibor® 1500-AS specimen in the range 0.15 to 0.2.

5.3.2   3-Point Bend Quasi-Static – 1.2 mm Side Impact Beams

This section of the thesis presents results from numerical simulations of the quasi-static 3-point bend experiments, in comparison with the corresponding experimental results. Figure 72 compares the numerical and experimental results for the fully hardened and tailored 1.2 mm side impact beams with a full backing plate. The results shown include all three die temperatures and both quenching periods.
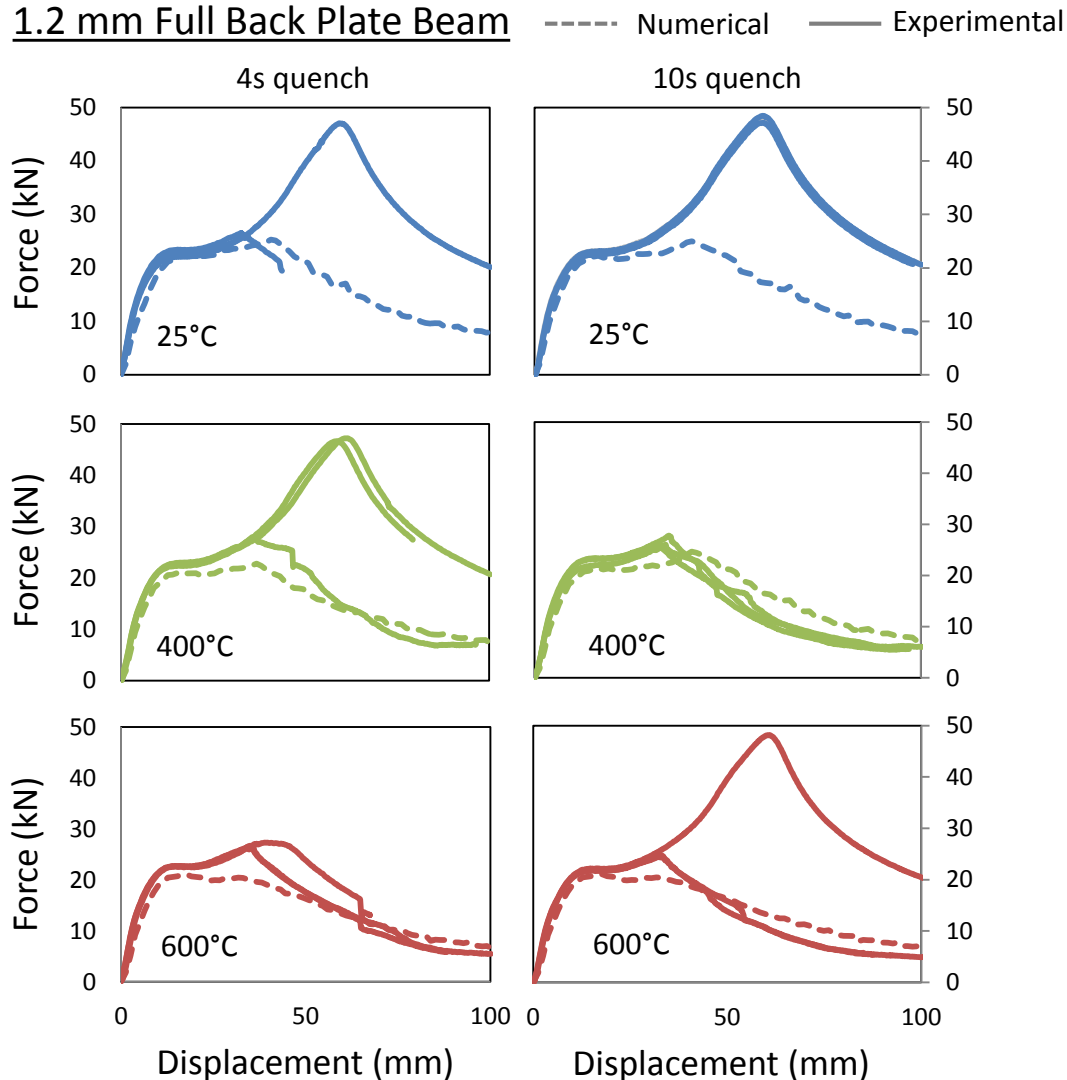
Figure 72: Numerical vs. experimental force-displacement results for 1.2 mm quasi-static 3-point bend test with full back plate configuration.

The predicted force vs. displacement response matches the measured force-displacement response produced by the side impact beams that exhibited a collapsing deformation mode. Generally, all six simulations have a first and second peak at which the sidewall begins to buckle and when the top surface begins to slide against the indentor, respectively. The behaviour of the specimens that exhibit a wrapping deformation mode is not captured by the model due to the selected friction coefficient of 0.2 for all numerical simulations. The model can be "tuned" to capture either mode by altering the friction coefficient; however, this approach was avoided in the current work. The exact explanation for the difference in mode selection in the experiments is unclear; nonetheless, the numerical results indicate that only a minor change in friction condition results in a dramatic difference in force-displacement response.

Top views of the center of a deformed side impact beam and the corresponding deformed finite element mesh are shown in Figure 73. The collapsing deformation mode is captured very well by the numerical simulation. Note that failure criteria are not implemented in the simulation, such that the observed cracking along the center line and at top and bottom of the center line (circled in Figure 73) is not predicted. Note that the addition of failure criteria is left for future work.
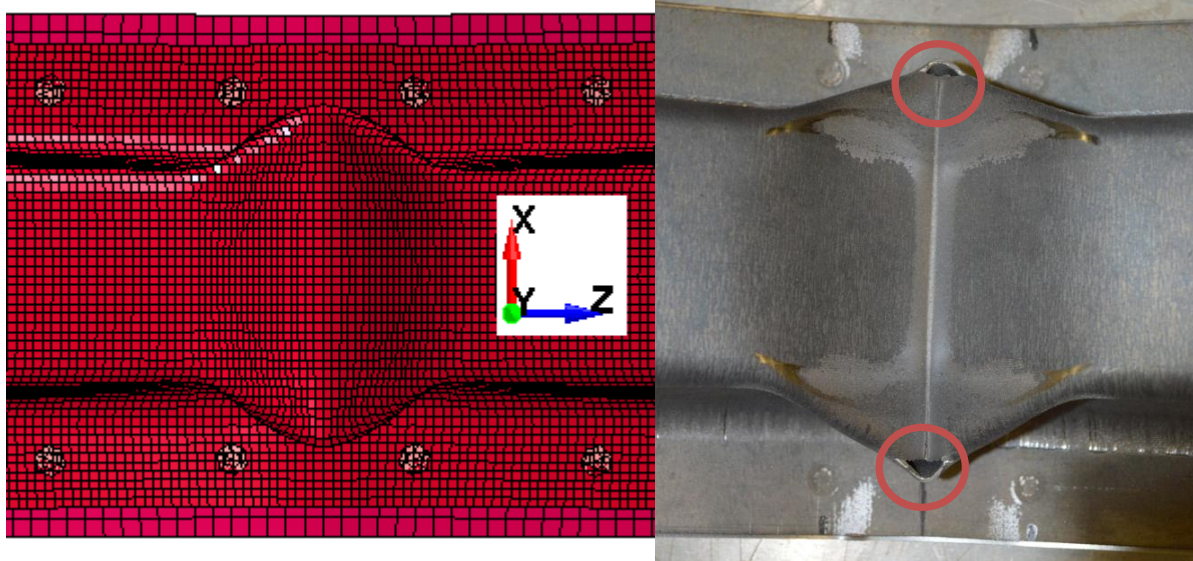
Figure 73: Fully hardened 1.2 mm with full back plate, predicted vs. actual deformation.

The results in Figure 74 shows the predicted and measured force versus displacement response of the 1.2 mm split back plate beams under quasi-static 3-point bend conditions. The simulations were also able to capture the general profile of the response as well as the deformation of a side impact beam collapsing under an indentor.
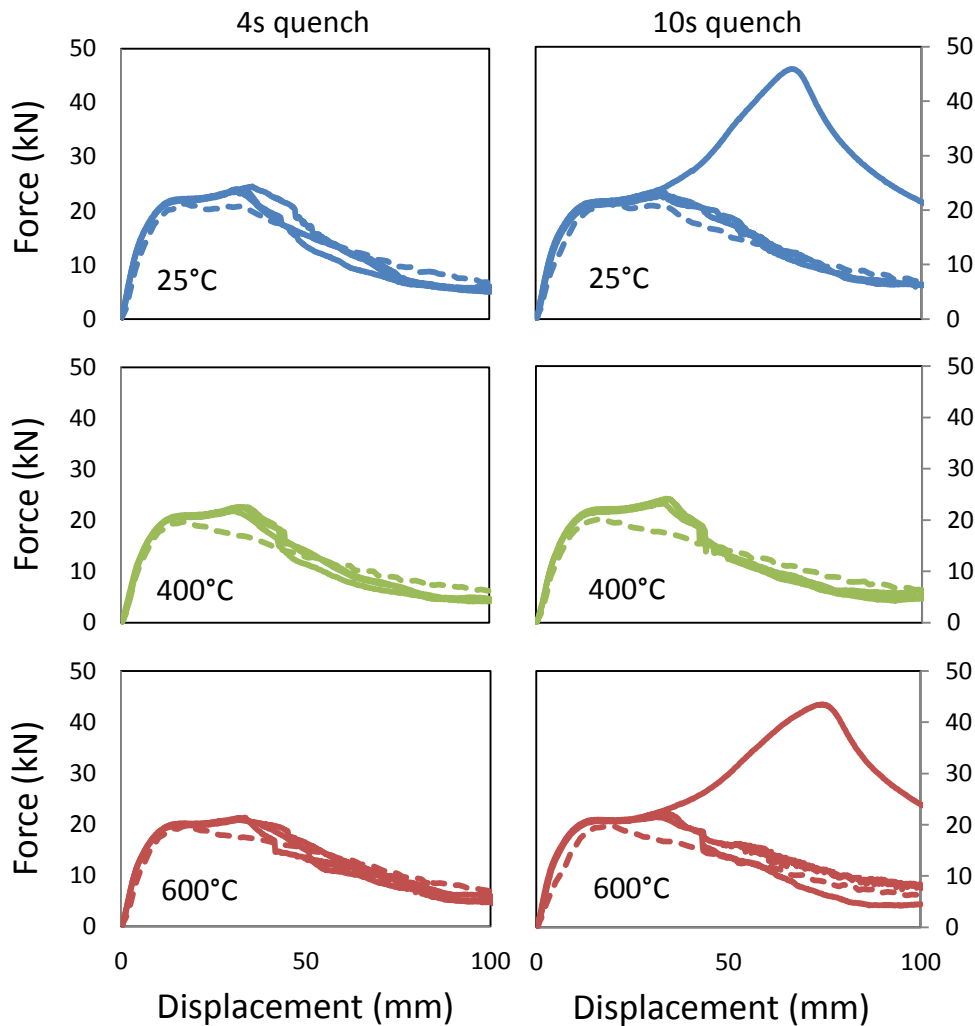
Figure 74: Numerical vs. experimental force-displacement results for 1.2 mm quasi-static 3-point bend test with split back plate configuration.

The split back plate 3-point bend models of the tailored specimens were not able to capture the second peak in the force versus displacement response. The predicted force response begins to descend after the first peak when the side wall begins to collapse. This may be caused by a softer as-formed flange resulting from the forming simulation (Section 5.2). In addition, there was a degree of warping of the as-formed hat section which resulted in a poor fit-up of the backing plate in the numerical model. This fit-up issue was addressed in the actual experiments by clamping the backing plate and hat section prior to welding.

Figure 75 compares the predicted deformation of a 1.2 mm side impact beam with a split back plate against the final deformation of an actual part. The simulation captured the correct shape in the deformed

area. The predicted deformation does not show the two fractures on both sides of the sidewall or the crack along the center line due to the absence of failure criteria in the model.
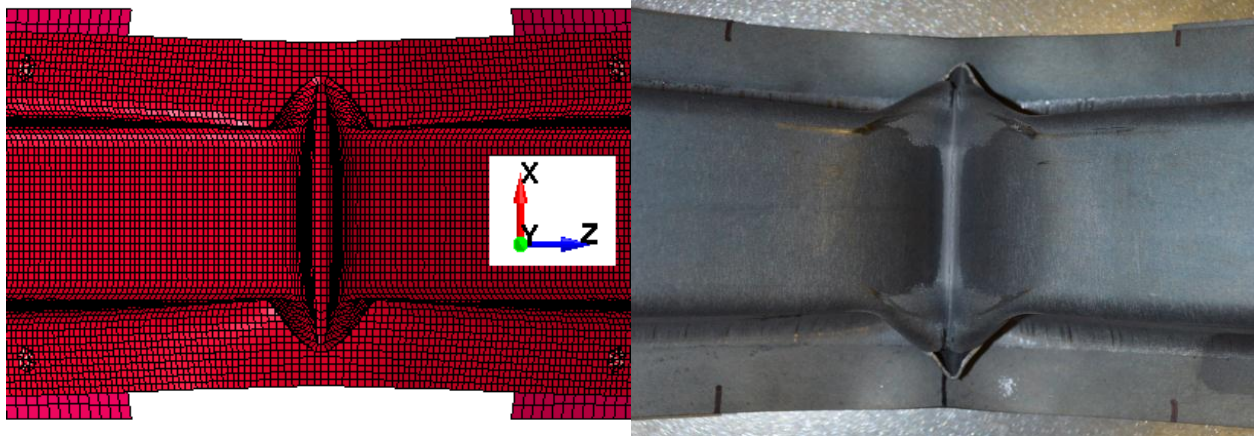
Figure 75: Fully hardened 1.2 mm with split back plate, predicted vs. actual deformation.

5.3.3 3-Point Bend Quasi-Static – 1.8 mm Side Impact Beams

The 50% increase in thickness inherent in the 1.8 mm side impact beams (relative to the 1.2 mm beams) nearly doubled the peak load in the predicted force vs. displacement response. The predicted and measured force-displacement results for the 1.8 mm side impact beams are plotted in Figure 76 and Figure 78 for the full back plate and split back plate configurations, respectively.
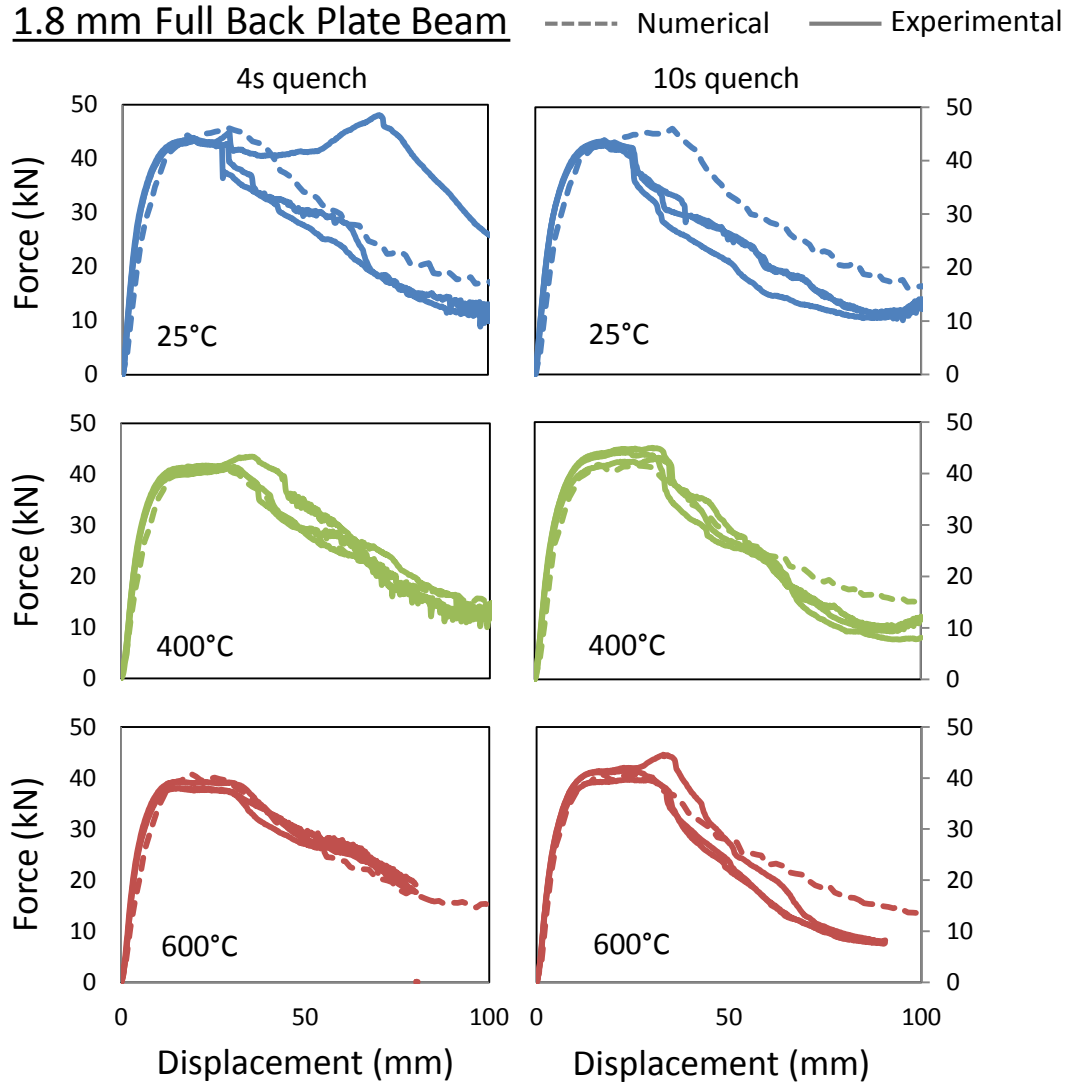
Figure 76: Numerical vs. experimental force-displacement results for 1.8 mm quasi-static 3-point bend test with full back plate configuration.

The numerical simulations were able to more accurately predict the overall force vs. displacement response of the 1.8 mm beams compared to that presented for the 1.2 mm beams; a primary reason being that all of the 1.8 mm beams exhibited a collapsing deformation mode which was matched by the model. The thicker 1.8 mm beams typically exhibited only one peak load before the specimens collapse under the impactor. Note that none of the thicker 1.8 mm side impact beams wrapped under the impactor in any tests for all forming temperatures and quenching times.

The models for the 1.8 mm beams also predicted the peak load more accurately than was the case for the 1.2 mm beams. The thicker specimens have a peak load in the range of 40 kN to 45 kN for all as-formed conditions. Due to the absence of failure criteria in the model, the predicted force response after a

displacement of approximately 40 mm is higher than most of the experimental cases. The best agreement between model and experiment was for the specimens formed using a 4 second quenching period with 400°C or 600°C die temperature.

Figure 77 compares the predicted deformation of a 1.8 mm side impact beam with a full back plate against the final deformation of an actual part. Similar to the 1.2 mm counterpart, the simulation captured the general deformation mode without the fracture due to the absence of failure criteria in the model.
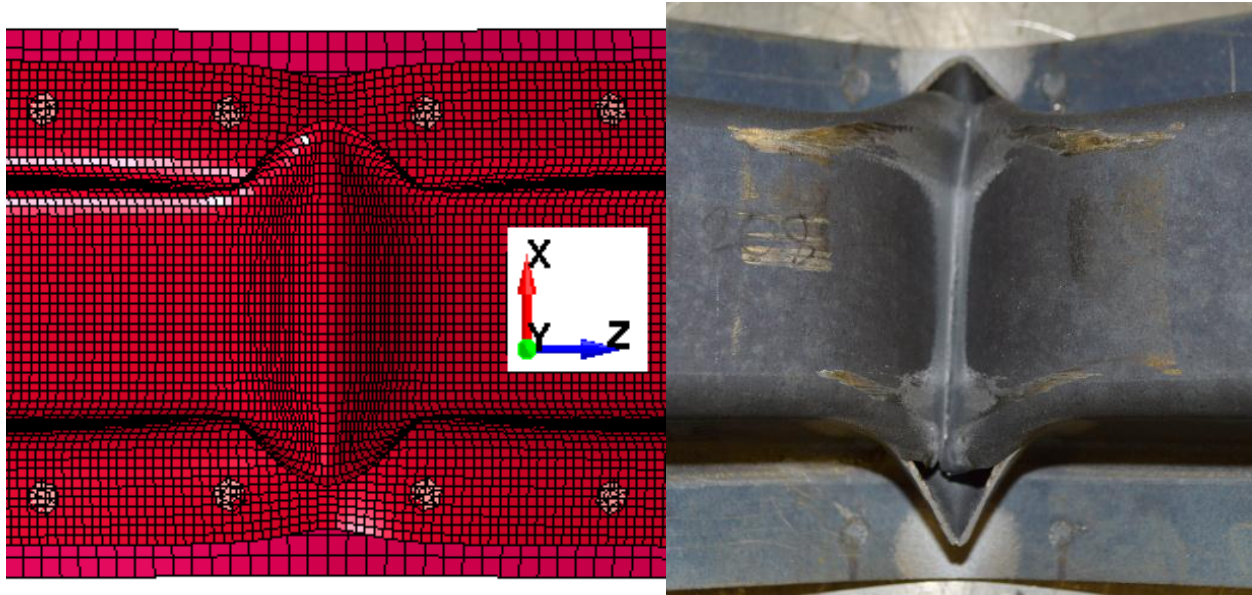
Figure 77: Fully hardened 1.8 mm with full back plate, predicted vs. actual deformation.

The predicted deformation is also very similar to the observed deformation in the experiments except for lack of failure due to absence of failure criteria in the model. Similar good agreement was obtained between the models and experiments on the 1.8 mm split back plate beams (Figure 78, Figure 79).
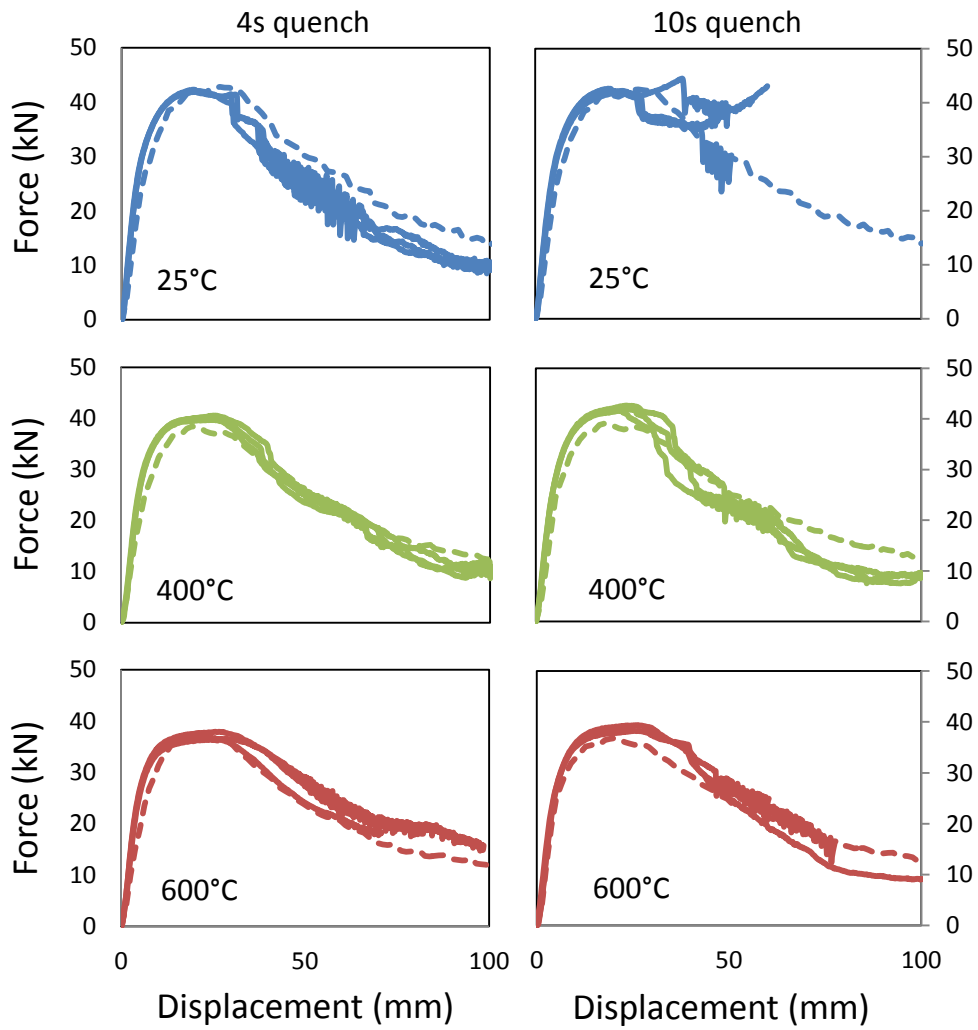
Figure 78: Numerical vs. experimental force-displacement results for 1.8 mm quasi-static 3-point bend test with split back plate configuration.
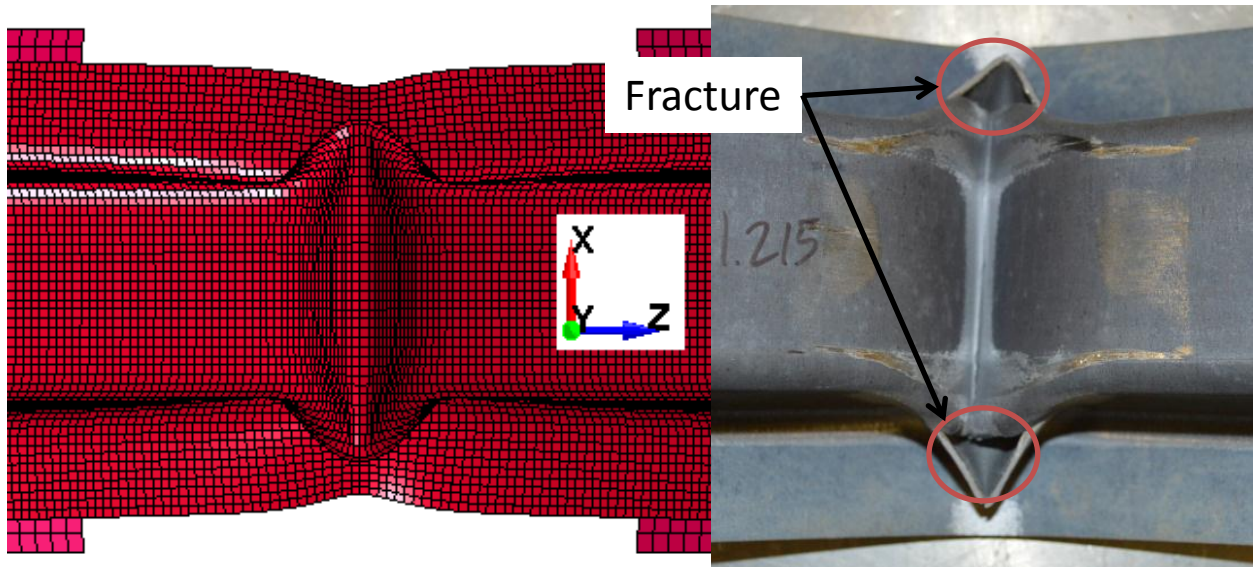
Figure 79: Fully hardened 1.8 mm with split back plate, predicted vs. actual deformation.

5.3.4　Impact Simulation Results

Impact simulations were performed corresponding to the limited impact test matrix. Due to the small difference in peak load between all three die temperatures used to form the tailored side impact beams, only fully hardened and tailored beams using a 600°C die temperature with a thickness of 1.2 mm were tested under dynamic loading. The impact test matrix was further limited to parts formed using a four second quenching period and both full and split back plates were tested. Numerical simulations were completed for each of these dynamic cases using the same finite element mesh as the corresponding quasi-static simulation. The simulation results are compared against the filtered measured load-displacement data in Figure 80. The numerical predictions match well with the filtered experimental results in terms of the predicted peak force, rate of increase, and rate of decrease in force response.

1.2 mm Impact 3-Point Bend Test:
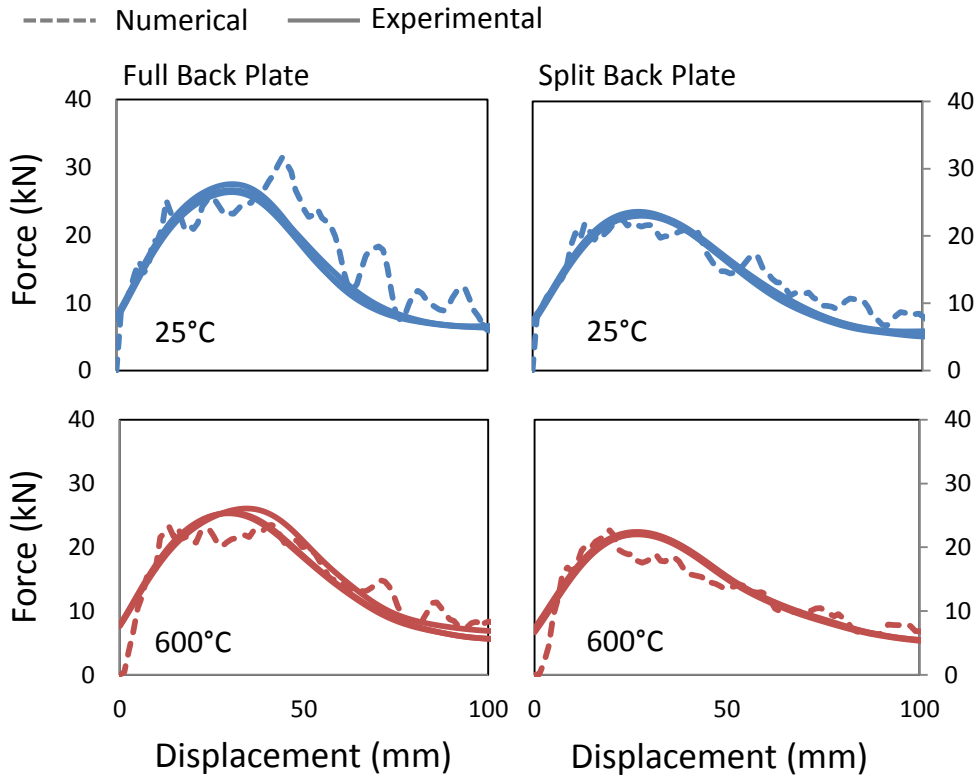
Figure 80: Predicted and measured force vs. displacement from impact experiments. Note that the experimental data was processed using a low pass SAE J211 filter with a cut off frequency of 60 Hz.

The area under the force vs. displacement curve of the impact test and simulation has been calculated and plotted in Figure 81 as cumulative energy absorbed vs. impactor displacement. The absorbed energy responses were calculated from the unfiltered experimental data to obtain a more accurate result. Overall, the absorbed energy predictions are relatively good, with some over-prediction for the fully hardened beams and under-prediction for the tailored beams. A summary of the predicted and measured absorbed energy at an impactor displacement of 100 mm is provided in Table 14.

1.2 mm Impact 3-Point Bend Test:
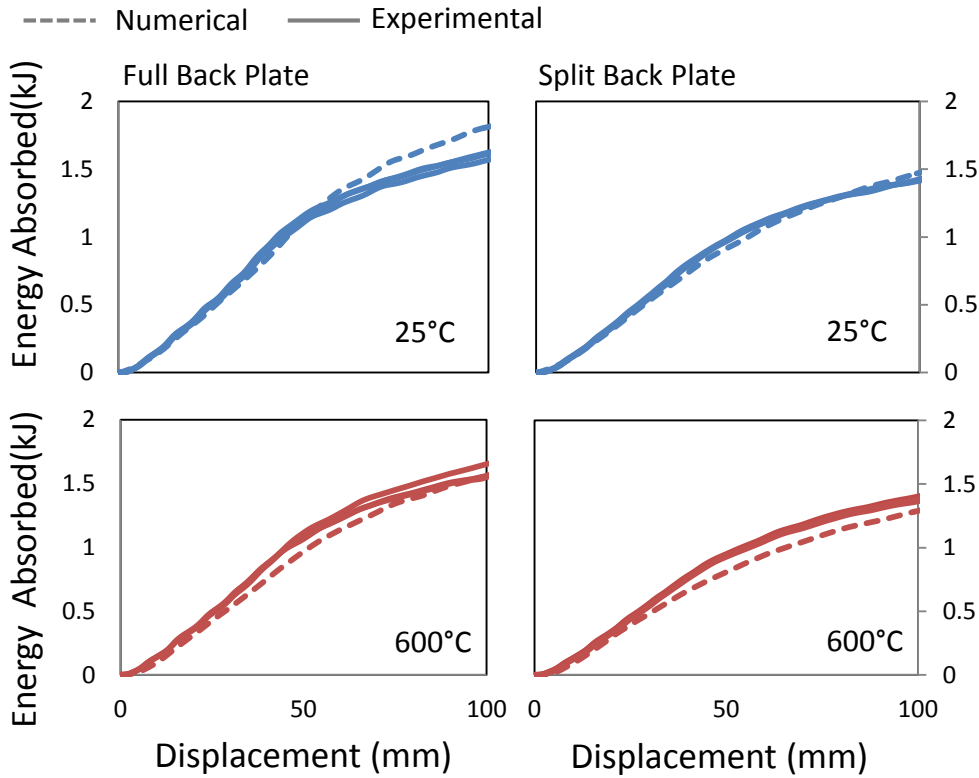
Figure 81: Cumulative energy absorbed vs. displacement of 1.2 mm side impact beams under high speed 3-point bend experiment.

Table 14: Energy absorbed during a 3-point bend impact test at an impactor displacement of 100 mm – Numerical and Experimental.

		Energy Absorbed (kJ)		
Forming Flange Temperature	Back Plate	Experimental Average	Numerical Result	% Difference
25°C	Full	1.60	1.81	13.1%
	Split	1.42	1.48	3.7%
600°C	Full	1.59	1.56	-1.6%
	Split	1.39	1.29	-7.1%

The over prediction of absorbed energy vs. displacement for the fully hardened beams can be attributed to the lack of failure criteria in the impact model. Under prediction of the energy absorbed for the tailored beams may be caused by the poor fit-up of the backing plate discussed in Section 5.3.2.

6 Conclusions and Recommendations

6.1 Conclusions

In this study, side impact beams were produced with hardenable Usibor®1500-AS to form top hat structure using tailored in-die heating hot stamping technology. Fully hardened and tailored specimens with softened flange were produced. The hardness distribution, force-displacement, and energy absorption of the side impact beams were reported. The following conclusions can be made from the results of this study:

1. The shorter quenching period of 4 seconds was able to produce a hardness of greater than 480 HV throughout the whole top hat structure for both thicknesses. The potential to reduce cycle time is very attractive from a manufacturing perspective.

2. Forming the flange with a locally heated tool reduced the hardness of the flange. When formed using a 4 second quenching period, the 1.2 mm beams have a flange hardness of 350 and 225 HV when formed at 400 and 600°C, respectively. The 1.8 mm beams achieved a low hardness of 265 and 200 HV when formed at 400 and 600°C, respectively. The 10 second quenching period yielded a flange hardness of 365 and 225 HV for the 1.2 mm formed at 400 and 600°C, respectively. The 1.8 mm beams have a hardness of 280 and 208 HV when formed at 400 and 600°C, respectively. Based on the findings of Bardelcik et al. [8,26], some ferrite is likely formed in the flanges produced using a 600°C die temperature.

3. The tailored 1.8 mm beams are more susceptible to change in its hardness distribution along the transition zone across the sidewall caused by a longer quenching period compared to the 1.2 mm beams. At 400°C, the sidewall hardness increased from 360 HV to 430 HV when the quenching period is increased from 4 to 10 seconds. At 600°C, the sidewall hardness is increased from 300 HV to 425 HV. In contrast, the 1.2 mm counterparts have a hardness difference of less than 10 HV between the two quenching periods. The transition zone is also wider for the 1.8 mm beams, measuring approximately 40 mm compared to 20 mm for the transition zone of the 1.2 mm beams formed at 600°C

4. In the three-point bending experiment, softening the flange caused a reduction in the measured peak load. The peak load difference is more pronounced in the beams spot welded using a split back plate configuration which loads the flange more directly without the back plate reinforcement. The 1.2 mm beams with a split back plate have a peak load of 21.6 kN, 20.7 kN, and 20.0 kN when formed with flange die temperatures of 25°C, 400°C, and 600°C, respectively. Similarly, the 1.8 mm beams with a split back plate have a peak load of 42.0 kN, 40.4 kN, and

37.0 kN when formed with flange die temperatures of 25°C, 400°C, and 600°C, respectively. The peak loads between the two quenching periods are comparable to each other.

5. The filtered force response of the dynamic experiments yielded similar peak load compared to the quasi-static force response. At an impactor displacement of 150 mm, the total energy absorbed is comparable at 1.96 kJ and 1.92 kJ for the dynamic and quasi-static cases, respectively.

6. Two deformation modes were seen in the quasi-static three-point bending experiments for the 1.2 mm side impact beams. The "collapse mode" takes place when there is insufficient friction to keep the beam in static contact with the indentor. The "wrapping mode" was not observed in the 1.8 mm beams or any of the dynamic experiments.

7. The numerical simulation of the hot forming process was able to predict the hardness distribution of the 1.2 mm beams. The hardness of the sidewall region of the thicker 1.8 mm beams was under predicted by the simulation due to the over prediction in the ferrite phase fraction for beams formed at 400 °C.

8. The numerical simulations of the three-point bending experiments were able to predict the force vs. displacement response well for the range of material condition and loading cases considered. Some under prediction for the tailored beams was seen due to the non-uniform node-to-node distance between the beam and back plate representing the spot weld.

6.2 Recommendations

In future work, the following recommendations should be considered to improve upon the work included in this thesis:

1. Tailoring regions that are more prone to deformation or fracture would lead to more differentiation in the force-displacement response and the amount of total energy absorbed. In this work, the sidewall region takes most of the load, while most of the deformation and fracture is located in the top area of the structure.

2. A computation fluid dynamics (CFD) simulation of the circulating chilled water should be done to predict a more accurate temperature distribution across the tooling die. It can also be used to predict the minimum flow rate of the chilled water through the cooled die to keep the die cool enough to provide sufficient cooling rate required to produce a fully martensitic component.

3. A beam with a longer span could be used to repeat three-point bending experiment using a larger support span. Sato et al. [41] showed that a larger span would allow for a more consistent deformation mode throughout all of the different forming parameters reducing the potential for the beams to wrap under the indentor. A longer span can also be used to test the beams using an indentor with a larger diameter.

4. Failure criteria should be implemented in future work which should improve the predicted force-displacement and absorbed energy responses of both the quasi-static and dynamic three-point bending simulation.

5. Metallurgical characterization should be done on the tailored parts formed at 600°C to determine the phase composition of specimens with a hardness of less than 240 HV. The final metallurgical properties can be used to calibrate the Akerstrom [46] model to better predict the actual microstructure phase composition.

6. A three-point bending experiment with additional supports added at both ends of the side impact beam to keep the specimen from rotating freely will simulate the mounting of a side impact beam to a car door frame. Such experiments would promote more deformation of the beam and may provide a larger differentiation of the force-displacement and absorbed energy-displacement responses between the different forming parameters.

References

[1] M. Kleiner, M. Geiger, A. Klaus, "Manufacturing of Lightweight Components by Metal Forming," CIRP Ann. Manuf. Technol., vol. 52 (2), pp. 521-542, 2003.

[2] R. Neugebauer, T. Altan, M. Geiger, M. Kleiner, A. Sterzing, "Sheet metal forming at elevated temperatures," CIRP Ann. Manuf. Technol., vol. 55 (2), pp. 793-816, 2006.

[3] B. Kinsey, Z. Liu, J. Cao, "A novel forming technology for tailor-welded blanks," J. Mater. Process. Technol., vol. 99 (1-3), pp. 145-153, 2000.

[4] H. Karbasian and A. E. Tekkaya, "A review on hot stamping," J. Mater. Process. Technol., vol. 210 (15), pp. 2103-2118, 2010.

[5] ArcelorMittal, "Steels for hot stamping -Usibor®", 2014.

[6] M. Maikranz-Valentin, U. Weidig, U. Schoof, H. H. Becker, K. Stienhoff, "Components with optimised properties due to advanced thermo-mechanical process strategies in hot sheet metal forming," Steel Research International, vol. 79 (2), pp. 92-97, 2008.

[7] P. Hein and J. Wilsius, "Status and innovation trends in hot stamping of USIBOR 1500 P," Steel Research International, vol. 79 (2), pp. 85-91, 2008.

[8] A. Bardelcik, M. J. Worswick, M. A. Wells. "The influence of martensite, bainite and ferrite on the as-quenched constitutive response of simultaneously quenched and deformed boron steel − Experiments and model," Mater. Des., vol. 55 (0), pp. 509-525, 2014.

[9] R. George, "Hot Forming of Boron Steels with Tailored Mechanical Properties: Experimental and Numerical Simulations, Masters Thesis, University of Waterloo, 2011.

[10] T. Svec, M. Merklein, "Tailored Tempering - Heat Transfer and Resulting Properties in Dependency of Tool Temperatures," 3rd International Conference of Hot Sheet Metal Forming of High-Performance Steel, Kassel, Germany, pp. 21-29, 2011.

[11] R. George, A. Bardelcik, M. Worswick, "Development of a hot forming die to produce parts with tailored mechanical properties - Numerical Study," 2nd International Conference of Hot Sheet Metal Forming of High Performance Steel, Lulea, Sweden, pp. 189-198, 2009.

[12] T. K. Eller, L. Greve, M. T. Andres, M. Medricky, A. Hatscher, V. T. Meinders, A. van den Boogaard, "Plasticity and fracture modeling of quench-hardenable boron steel with tailored properties," Journal of Materials Processing Tech., vol. 214 (6), pp. 1211-1227, 2014.

[13] K. Omer, "Development and Testing of a Hot Stamped Axial Crush Member with Tailored Properties," Masters Thesis, University of Waterloo, 2014.

[14] Y. Prajogo, K. Omer, A. Bardelcik, R. George, M. Worswick, N. Adam, D. Detwiler, "Development of a Hot Stamped Side Impact Beam and Axial Crush Member with Tailored Properties - Numerical Models," 4th International Conference of Hot Sheet Metal Forming of High-Performance Steel, Lulea, Sweden, pp. 15-22, 2013.

[15] K. Mori and Y. Okuda, "Tailor die quenching in hot stamping for producing ultra-high strength steel formed parts having strength distribution," CIRP Ann. Manuf. Technol., vol. 59 (1), pp. 291-294, 2010.

[16] A. E. Tekkaya, H. Karbasian, W. Homberg, M. Kleiner, "Thermo-mechanical coupled simulation of hot stamping components for process design," Production Engineering, vol. 1 (1), pp. 85-89, 2007.

[17] R. Perez-Santiago, E. Billur, A. Ademaj, C. Sarmiento, R. Berlanga, T. Altan, "Hot Stamping a B-Pillar with Tailored Properties: Experiments and Preliminary Simulation Results," 4th International Conference of Hot Sheet Metal Forming of High-Performance Steel, Lulea, Sweden, pp. 83-90, 2013.

[18] R. George, A. Bardelcik, M. J. Worswick, "Hot forming of boron steels using heated and cooled tooling for tailored properties," J. Mater. Process. Technol., vol. 212 (11) pp. 2386-2399, 2012.

[19] M. Sigvant, M. Fermer, O. Hedegard, R. Johansson, P. Nystrom, "Improved Ductility and Spot Weld Strength by Local Annealing of Hot-Formed Steel," 4th International Conference of Hot Sheet Metal Forming of High-Performance Steel, Lulea, Sweden, pp. 387-395, 2013.

[20] H. S. Choi, S. G. Kim, S. K. Lee, B. M. Kim, D. C. Ko, "Improvement Technology of Tool Performance in Mechanical Trimming of Hot Stamped 22MnB5 Steel," 4th International Conference of Hot Sheet Metal Forming of High-Performance Steel, Lulea, Sweden, pp. 191-198, 2013.

[21] K. Mori, T. Maeno, S. Fuzisaka, "Punching of ultra-high strength steel sheets using local resistance heating of shearing zone," Journal of Materials Processing Tech., vol. 212 (2) No. 2, pp. 534-540, 2012.

[22] K. Mori, S. Saito, S. Maki, "Warm and hot punching of ultra high strength steel sheet," CIRP Ann. Manuf. Technol., vol 57 (1), pp. 321-324, 2008.

[23] A. Naganathan, "Hot Stamping of Manganese Boron Steel (Technology Review and Preliminary Finite Element Simulations)," Masters Thesis, The Ohio State University, 2010.

[24] R. Kolleck, R. Veit, H. Hofmann, F. Lenze, "Alternative heating concepts for hot sheet metal forming," 1st International Conference of Hot Sheet Metal Forming of High-Performance Steel, Kassel, Germany, pp. 239-246, 2008.

[25] A. Bardelcik, C. P. Salisbury, S. Winkler, M. A. Wells, M. J. Worswick, "Effect of cooling rate on the high strain rate properties of boron steel," Int. J. Impact Eng., vol. 37 (6), pp. 694-702, 2010.

[26] A. Bardelcik, M. J. Worswick, S. Winkler, M. A. Wells, "A strain rate sensitive constitutive model for quenched boron steel with tailored properties," Int. J. Impact Eng., vol 50 (0), pp. 49-62, 2012.

[27] F. J. Ebner, "The HotPHASE Multi-Level Chamber Furnace - Concept, Advantages and Experiences from Production," 4th International Conference of Hot Sheet Metal Forming of High-Performance Steel, Lulea, Sweden, pp. 199-204, 2013.

[28] R. Kolleck, R. Veit, M. Merklein, J. Lechler, M. Geiger, "Investigation on induction heating for hot stamping of boron alloyed steels," CIRP Ann. Manuf. Technol., vol. 58 (1), pp. 275-278, 2009.

[29] K. Mori, T. Maeno, K. Mongkolkaji, "Tailored die quenching of steel parts having strength distribution using bypass resistance heating in hot stamping," J .Mater.Process. Technol., vol. 213 (3), pp. 508-514, 2013.

[30] M. A. Ahmetoglu, D. Brouwers, L. Shulkin, L. Taupin, G. L. Kinzel, T. Altan, "Deep drawing of round cups from tailor-welded blanks," J. Mater. Process. Technol., vol. 53 (3-4), pp. 684-694, 1995.

[31] D. D. Munera, A. Pic, D. Abou-Khalil, F. Shmit, "Innovative Press Hardened Steel Based Laser Welded Blanks Solutions for Weight Savings and Crash Safety Improvements," SAE International Journal of Materials and Manufacturing 1, pp. 472-479, 2008.

[32] R. Padmanabhan, M. C. Oliveira, L. F. Menezes, "Deep drawing of aluminium–steel tailor-welded blanks," Mater. Des., vol. 29 (1), pp. 154-160, 2008.

[33] T. Stoehr, J. Lechler, M. Merklein, "Investigations on different stamping strategies for influencing the microstructural properties with respect to partial hot stamping," 2nd International Conference of Hot Sheet Metal Forming of High-Performance Steel, Lulea, Sweden, pp. 273-281, 2009.

[34] J. Wilsius, B. Tavernier, D. Abou-Khalil, "Experimental and Numerical Investigation of Various Hot Stamped B-Pillar Concepts Based on Usibor® 1500P," 3rd International Conference of Hot Sheet Metal Forming of High-Performance Steel, Kassel, Germany, pp. 427-435, 2011.

[35] T. Labudde and W. Bleck, "Formability characterisation of press hardened steels," 2nd International Conference of Hot Sheet Metal Forming of High-Performance Steel, Lulea, Sweden, pp. 127-135, 2009.

[36] R. George, A. Bardelcik, M. Worswick, "Hot Forming of a Lab-Scale B-Pillar with Tailored Properties - Experiment and Modeling," 3rd International Conference of Hot Sheet Metal Forming of High-Performance Steel, Kassel, Germany, pp. 31-37, 2011.

[37] S. Erturk, M. Sester, M. Selig, P. Feuser, K. Roll, "A Thermo-Mechanical-Metallurgical FE Approach for Simulation of Tailored Tempering," 3rd International Conference of Hot Sheet Metal Forming of High Performance Steel, Kassel, Germany, pp. 447-454, 2011.

[38] J. Banik, F. Lenze, S. Sikora, R. Laurenz, "Tailored Properties - A Pivotal Question for Hot Forming," 3rd International Conference on Hot Sheet Metal Forming of High Performance Steel, Kassel, Germany, pp. 13-20, 2011.

[39] R. Erhardt and J. Boke, "Industrial application of hot forming press simulation," 1st International Conference of Hot Sheet Metal Forming of High Performance Steel, Kassel, Germany, pp. 83-88, 2008.

[40] D. Berglund, "Hot Stamped components with tailored properties - Simulation and validation of Product Performance, 2nd International Conference of Hot Sheet Metal Forming of High Performance Steel, Lulea, Sweden, pp. 293-301, 2009.

[41] K. Sato, T. Inazumi, A. Yoshitake, S. Liu, "Effect of material properties of advanced high strength steels on bending crash performance of hat-shaped structure," Int. J. Impact Eng., vol. 54 (0), pp. 1-10, 2013.

[42] H. Bok, M. Lee, E. J. Pavlina, F. Barlat, H. Kim, "Comparative study of the prediction of microstructure and mechanical properties for a hot-stamped B-pillar reinforcing part," Int. J. Mech. Sci., vol. 53 (9), pp. 744-752, 2011.

[43] H. Karbasian, C. Klimmek, A. Brosius, A. E. Tekkaya, "Numerical process design of hot stamping processes based on optimized thermo-mechanical chracteristics," 1st International Conference of Hot Sheet Metal Forming of High-Performance Steel, Kassel, Germany, pp. 97-103, 2008.

[44] A. B. Shapiro, "Using LS-DYNA to model hot sheet metal stamping," 1st International Conference of Hot Sheet Metal Forming of High-Performance Steel, Kassel, Germany, pp. 89-95, 2008.

[45] P. Åkerström and M. Oldenburg, "Austenite decomposition during press hardening of a boron steel—Computer simulation and test," J. Mater. Process. Technol., vol. 174 (1-3), pp. 399-406, 2006.

[46] P. Akerstrom, "Modelling and Simulation of Hot Stamping," Doctoral Thesis, Lulea University of Technology, 2006.

[47] J. S. Kirkaldy and D. Venugopalan, "Prediction of mocrostructure and hardenability in low alloy steels, in: A.R. Marder, J.I. Goldstein (Eds.)," International Conference on Phase Transformations in Ferrous Alloys, Philadelphia, PA, pp. 125-148, 1983.

[48] M. V. Li, D. Niebuhr, L. Meekisho, D. Atteridge, "A computational model for the prediction of steel hardenability," Metallurgical and Materials Transactions B, vol. 29 (3), pp. 661-672, 1998.

[49] Livermore Software Technology Corporation (LSTC), LS-DYNA® KEYWORD USER'S MANUAL VOLUME II - Material Models - Version R7.0, 2013.

[50] P. Maynier, B. Jungmann, J. Dollet, "Creusot-loire system for the prediction of the mechanical properties of low alloy steel products, in: D.V. Doane, J.S. Kirkaldy (Eds.)," Hardenability Concepts with Applications to Steel, Warrendale, PA, pp. 518, 1978.

[51] B. K. D. H. Bhadeshia, "Bainite in Steels," The Institute of Materials, London, U.K. 0-901462-95-0, 1992.

[52] R. W. K. Honeycombe, "Steels - Microstructure and Properties," Edvard Arnold 0-7131-27937, 1981.

[53] M. Schill, B. Hochholdinger, D. Lorenz, T. Erhart, "An Advanced Material Model for the Predictions of Phase Fractions and Part Properties in the Press Hardening Process," in 4th International Conference on Hot Sheet Metal Forming of High-Performance Steel, Lulea, Sweden, pp. 31-38, 2013.

[54] Livermore Software Technology Corporation (LSTC), LS-DYNA® KEYWORD USER'S MANUAL VOLUME I - Version R7.0, 2013.

[55] J. Leblond, G. Mottet, A. Devaux, "A Theoretical and Numerical Approach to the Plastic Behavior of Steels during Phase-Transformations 1. Derivation of General Relations," J. Mech. Phys. Solids, vol. 34 (4), pp. 395-409, 1986.

[56] J. Leblond, G. Mottet, A. Devaux, "A Theoretical and Numerical Approach to the Plastic Behavior of Steels during Phase-Transformations 2. Study of Classical Plasticity for Ideal-Plastic Phases," J. Mech. Phys. Solids, vo;. 34 (4), pp. 411-432, 1986.

[57] J. Leblond, J. Devaux, J. C. Devaux, "Mathematical-Modeling of Transformation Plasticity in Steels .1. Case of Ideal-Plastic Phases," Int. J. Plast., vol. 5 (6), pp. 551-572, 1989.

[58] J. Leblond, "Mathematical-Modeling of Transformation Plasticity in Steels .2. Coupling with Strain-Hardening Phenomena," Int. J. Plast., vol. 5 (6) No. 6, pp. 573-591, 1989.

[59] E. J. F. R. Caron, K. J. Daun, M. A. Wells, "Heat Transfer Coefficient Characterization during Hot Forming Die Quenching of Boron Steel Blanks," 4th International Conference of Hot Sheet Metal Forming of High-Performance Steel, Lulea, Sweden, pp. 407-414, 2013.

[60] M. Oldenburg and G. Lindkvist, "Tool thermal cycle design for manufacturing of components with tailored material properties," 3rd International Conference on Hot Sheet Metal Forming of High-Performance Steel, Kassel, Germany, pp. 203-210, 2011.

[61] M. Merklein and J. Lechler, "Determination of Material and Process Characteristics for Hot stamping Processes of Quenchenable Ultra High Strength Steels with Respect to a FE-based Process Design," Society of Automotive Engineers technical paper series, 2008.

[62] M. Merklein, J. Lechler, T. Stoehr, "Characterization of Tribological and Thermal Properties of Metallic Coatings for Hot Stamping Boron-Manganese Steels," 7th International Conference The Coatings in Manufacturing Engineering, Chalkidiki, Greece, pp. 219-228, 2008.

[63] E. Caron, K. Daun, M. Wells, "Experimental Characterization of Heat Transfer Coefficients During Hot Forming Die Quenching of Boron Steel," Metallurgical and Materials Transactions B, vol. 44 (2), pp. 332-343, 2013.

[64] A. Yanagida, A. Azushima, "Evaluation of coefficients of friction in hot stamping by hot flat drawing test," Cirp Annals-Manufacturing Technology, vol. 58 (1), pp. 247-250, 2009.

[65] J. Hardell, E. Kassfeldt, B. Prakash, "Friction and wear behaviour of high strength boron steel at elevated temperatures of up to 800 °C," Wear, vol. 264 (9-10), pp. 788-799, 2008.

[66] A. Ghiotti, S. Bruschi, F. Borsetto, "Tribological characteristics of high strength steel sheets under hot stamping conditions," J. Mater. Process. Technol., vol. 211 (11), pp. 1694-1700, 2011.

[67] P. Hora, "Benchmark Problem BM03," The Numisheet 2008 Benchmark Study, Interlaken, Switzerland, 2008.

[68] E. Voce, "The Relationship between Stress and Strain for Homogeneous Deformation," Journal of the Institute of Metals, vol. 74 (11), pp. 537-562, 1948.

[69] A. Bardelcik, K. Ghavam, R. George, M. J. Worswick, "An impact model of a hot stamped lab-scale B-pillar with tailored properties," 3rd International Conference of Hot Sheet Metal Forming of High-Performance Steel, Kassel, Germany, pp. 221-228, 2011.

[70] R. Ostlund, D. Berglund, M. Oldenburg, "Failure Analysis of a Hat Profile with Tailored Properties Subjected to Axial Compression, 4th International Conference of Hot Sheet Metal Forming of High-Performance Steel, Lulea, Sweden, pp. 23-30, 2013.

[71] ArcelorMittal, Usibor® 1500P material composition, 2009.

[72] T. Nishibata and N. Kojima, "Effect of quenching rate on hardness and microstructure of hot-stamped steel," Journal of Alloys and Compounds, vol. 577, pp. S549-S554, 2013.

[73] I ZIRCAR Refractory Composites, REFRACTORY BOARD TYPES ZIRCAL-18, ZIRCAL-45 AND ZIRCAL 95.

[74] R. George, A. Bardelcik, M. Worswick, "Improving the Prediction of the Bainite and Ferrite Phase Transformation During Hot Stamping Simulations Using LS-DYNA," 4th International Conference of Hot Sheet Metal Forming of High-Performance Steel, Lulea, Sweden, pp. 67-74, 2013.

[75] J. O. Hallquist, LS-DYNA Theory Manual, 2006.

[76] Incropera, DeWitt, Bergmann, Lavine, "Fundamentals of Heat and Mass Transfer," 6th ed., John Wiley & Sons, 2006.

[77] A. Bardelcik, Y. Prajogo, M. Worswick, D. Detwiler, S. Malcolm, "Mechanical and Microstructural Properties of a Tailored Hot Stamping with In-Die Heating," 5th International Conference on Hot Sheet Metal Forming of High-Performance Steel, Toronto, Canada, pp. 775-782, 2015.

[78] A. Barcellona and D. Palmeri, "Effect of Plastic Hot Deformation on the Hardness and Continuous Cooling Transformations of 22MnB5 Microalloyed Boron Steel," Metall. Mater. Trans. A-Phys. Metall. Mater. Sci., vol. 40A (5), pp. 1160-1174, 2009.

[79] J. Min, J. Lin, Y. Min, F. Li, "On the ferrite and bainite transformation in isothermally deformed 22MnB5 steels," Materials Science and Engineering: A, vol. 550 (0), pp. 375-387, 2012.

[80] M. Naderi, A. Saeed-Akbari, W. Bleck, "The effects of non-isothermal deformation on martensitic transformation in 22MnB5 steel," Mater. Sci. Eng. A - Struct. Mater. Prop. Microstruct. Process., vol. 487 (1-2), pp. 445-455, 2008.

[81] A Bardelcik, Private Communication, 2015.